Copyright

by

Shuang Liu

2012

The Dissertation Committee for Shuang Liu Certifies that this is the approved version of the following dissertation:

THICKNESS, PHASE RETARDATION, BIREFRINGENCE, AND REFLECTANCE OF THE RETINAL NERVE FIBER LAYER: IMPLICATIONS FOR GLAUCOMA DIAGNOSIS

Committee:

H. Grady Rylander III, Supervisor

Mia K. Markey, Co-Supervisor

Thomas E. Milner

Joydeep Ghosh

Alan C. Bovik

Thickness, phase retardation, birefringence, and reflectance of the retinal nerve fiber layer: Implications for glaucoma diagnosis

by

Shuang Liu, B.S.E.E.; M.S.E.E.

Dissertation

Presented to the Faculty of the Graduate School of

The University of Texas at Austin

in Partial Fulfillment

of the Requirements

for the Degree of

Doctor of Philosophy

The University of Texas at Austin

May 2012

Dedication

To my son, Leonardo S. Wang, my husband, Daifeng Wang, my parents, Jianxin Liu and Xiaoping Chen, and my parents-in-law, Fang Wang and Zhan Feng.

Acknowledgements

I owe my deepest gratitude to my husband, Daifeng Wang and my son, Leonardo S. Wang. Without their continuous love and support, my Ph.D. study would not have been completed in four and a half years. I am also very grateful to thank my parents, Jianxin Liu and Xiaoping Chen, and my parents-in-law, Fang Wang and Zhan Feng. They have been constantly encouraging me even at my very tough times.

I also would like to express my highest gratitude to my supervisors, Prof. H. Grady Rylander III and Prof. Mia K. Markey, not only for their excellent academic advice, but also for all kinds of support in my life. I really want to thank Prof. Rylander and Prof. Markey for advising me from strengthening the research results, writing manuscripts, revising papers to finishing the Ph.D. dissertation. This dissertation would not have been possible without their guidance, commitment, understanding, and patience.

My thanks also go out to my committee members, Prof. Thomas E. Milner, Prof. Joydeep Ghosh and Prof. Alan C. Bovik for their helpful suggestions on my research. I would like to show my special thanks to Prof. Milner for his critical edits and comments on my research and our co-authored papers.

Last but not least, I would also like to thank all members of UT Biomedical Engineering Laser Laboratory and Biomedical Informatics Lab, especially to Bingqing Wang, Jordan Dwelle, Biwei Yin, Amit Paranjape, Wendy Kan, Juhun Lee, and Gautam Muralidhar for their help. I would like to show my special thanks to my undergraduate assistants Anjali Datta and Derek Ho in Biomedical Informatics Lab.

Thickness, phase retardation, birefringence, and reflectance of the retinal nerve fiber layer: Implications for glaucoma diagnosis

Shuang Liu, Ph.D.

The University of Texas at Austin, 2012

Supervisors: H. Grady Rylander III and Mia K. Markey

Glaucoma is the second leading cause of blindness worldwide after cataract. Retinal nerve fiber layer thickness (RNFLT), phase retardation, and birefringence measured by Polarization Sensitive Optical Coherence Tomography (PS-OCT) have been used for glaucoma diagnosis. We first investigated two different image registration algorithms, a mutual information (MI) based algorithm and a log-polar transform cross-correlation (LPCC) based algorithm, on both human and non-human primate models. We evaluated the effects of image registration on longitudinal analysis of RNFLT in non-human primates using PS-OCT. Then, we investigated thickness, phase retardation, birefringence, and reflectance of the retinal nerve fiber layer as measured by PS-OCT in normal and glaucomatous non-human primates in a longitudinal study. We defined a new Reflectance Index (RI) and demonstrated that it might be an earlier indicator of glaucoma onset than RNFLT, phase retardation, or birefringence. Finally, we validated this finding on cross-sectional clinical study on human eyes measured by PS-OCT and RTVue OCT. For the data measured by PS-OCT, we showed that for distinguishing between glaucomatous and healthy eyes, as well as for distinguishing between glaucoma suspect and healthy eyes, our new normalized RNFL reflectance index (NRRI) performs significantly better than phase retardation and birefringence. The performances of NRRI and RNFL thickness in both conditions were statistically indistinguishable in this study,

which is likely due to the limited sample size. For the data measured by RTVue OCT, the performances of NRRI and RNFL thickness were statistically indistinguishable for distinguishing between glaucomatous and healthy eyes. NRRI performs significantly better than RNFL thickness for distinguishing between glaucoma suspect and healthy eyes. NRRI also performs significantly better than temporal, superior, nasal, inferior and temporal (TSNIT) average and nerve fiber indicator (NFI) from GDx VCC for distinguishing between glaucoma suspect and healthy eyes. NRRI is a promising parameter for distinguishing glaucoma suspect and healthy eyes and may indicate disease in the pre-perimetric stage.

Table of Contents

List of Tables

List of Figures

Chapter 1: Introduction

1.1 Background

Glaucoma is the second leading cause of blindness worldwide after cataract [1,2]. It is a progressive disease characterized by loss of retinal ganglion cells (RGCs) and their axons in the retinal nerve fiber layer (RNFL) with or without associated visual field loss. There are multiple approaches to glaucoma diagnosis, including measurement of intraocular pressure (IOP) and visual field testing. Optic nerve imaging devices such as GDx VCC (Carl Zeiss Meditec, Inc), Heidelberg Retinal Tomography (HRT, Heidelberg Engineering, GmbH, Dossenheim, Germany), and Optical Coherence Tomography (OCT) (Cirrus HD-OCT, Carl Zeiss Meditec, Inc, etc.) are also widely used to assist in glaucoma diagnosis. However, an estimated 50% of glaucoma cases in the USA are undiagnosed [3]. Furthermore, it is estimated that up to 50% of axons can be lost before any visual field defect is apparent [4]. Since visual field loss cannot be restored, earlier diagnosis and therapy may preserve visual function and reduce blindness caused by glaucoma.

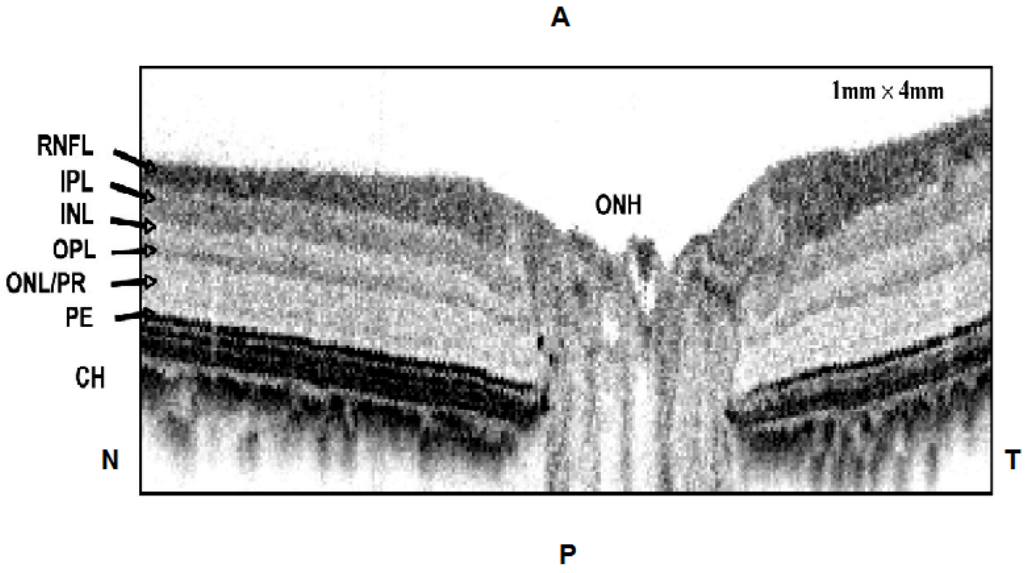

Figure 1. OCT B-scan image of in vivo primate retina demonstrating morphological features provided by OCT. (A: anterior; P: posterior; N: nasal; T: temporal; ONH: optic nerve head; RNFL: retinal nerve fiber layer; IPL: inner plexiform layer; INL: inner nuclear layer; OP: outer plexiform layer; ONL/PR: outer nuclear layer and photoreceptors; PE: pigment epithelium; CH: choroid). Image is 1mm deep by 4mm wide.

1.2 SIGNIFICANCE

The definition of glaucoma by American Optometric Association is "a group of ocular diseases with various causes that ultimately are associated with a progressive optic neuropathy leading to loss of vision function" [5]. Glaucoma can lead to partial or total blindness if it is diagnosed too late. Visual field loss in glaucoma usually starts from the periphery and gradually progresses to the central visual field. However, most glaucoma patients are unaware of the visual field loss since the process is gradual and painless. Therefore, in order to detect and manage patients at risk for developing glaucoma, prevent damage to the optic nerve, and preserve patients' quality of life, the American Academy of Ophthalmology gave the definition of primary open-angle glaucoma suspect

as “an individual with clinical findings and/or a constellation of risk factors that indicate an increased likelihood of developing POAG”[6].

Several techniques including tonometry, visual field testing, optic nerve evaluation, and optic nerve imaging have been developed in order to diagnose glaucoma before vision loss is noticed subjectively by the patient [5].

1.2.1 Current traditional approaches for glaucoma diagnosis

(a) Tonometry

Tonometry is a procedure to determine the intraocular pressure (IOP). High eye pressure used to be considered a hallmark of glaucoma. However, it is now recognized that IOP varies based on several factors including age, gender, blood pressure, diabetes mellitus, and exercise. Moreover, 30% of patients diagnosed with glaucoma have statistically normal IOP. Thus, tonometry alone is not sufficiently reliable for glaucoma diagnosis [7].

(b) Visual field testing

Visual field testing has been used for glaucoma diagnosis for several decades. Visual field loss is the gold standard for defining the presence of glaucoma. Visual field testing results are plotted as a visual field map. A visual field map can be used to evaluate the function of the optic nerve and can provide clinical assessment of visual function. In order to provide a reliable visual field map, the patient has to be able to understand the testing instructions, be fully cooperative, and complete the entire test. However, since visual field testing takes a long time to finish, about 30 minutes for both eyes, some patients have difficulty completing it [5].

(c) Optic nerve evaluation

Visual inspection of the optic nerve head is another method of detecting glaucoma. The optic nerve head can be viewed using a slitlamp biomicroscope and a handheld lens. Fundus photography is also used to document the morphology of the optic nerve head. The cup to disc ratio is usually used to describe the topographic appearance of the optic nerve. Larger cup to disc ratios indicate greater risk for glaucoma. However, there is a large range of normal cup to disc ratio values. Moreover, there is large inter- and intra-observer variability in cup to disc ratio assessment. Thus, optic nerve evaluation alone is not sufficiently reliable for glaucoma diagnosis [5,7].

1.2.2 Optic nerve imaging devices for glaucoma diagnosis

None of the traditional methods reviewed in 1.2.1 can provide quantitative measures of the morphological or structural changes in the retina caused by glaucoma. Therefore, these methods are of limited value for early detection of glaucoma and monitoring of glaucoma progression. In contrast, new instruments for optic nerve imaging provide more detailed information for glaucoma diagnosis. Two of the most widely used, commercially available instruments are the GDx nerve fiber analyzer (GDx VCC, Carl-Zeiss Meditec, Dublin, CA) and Optical Coherence Tomography (OCT such as Cirrus HD-OCT, Carl Zeiss Meditec, Inc, etc.).

(a) GDx Nerve fiber analyzer (GDx)

The GDx Nerve fiber analyzer is based on the concept of Scanning Laser Polarimetry (SLP). Since neurotubules within the retinal ganglion cell axons exhibit birefringent properties, GDx measures the change in polarization of the scanning beam of a polarized diode laser light with wavelength 780nm. GDx provides a quantitative analysis of the

peripapillary RNFL phase retardation (δ). Recent studies using GDx report sensitivity ranging in 92.3% - 96% and specificity values from 93% - 96% for diagnosing glaucoma [8,9,10].

(b) Optical Coherence Tomography (OCT)

Optical Coherence Tomography is a noninvasive imaging method that provides high-resolution morphological imaging data of the eye. An example of a high resolution OCT B-scan of primate retina is shown in Figure 1. The depth resolution of OCT makes it a very useful tool to quantify changes in RNFL thickness (Δz) associated with glaucoma. A recent study reports sensitivity of 85% and specificity of 94% for the Cirrus OCT instrument (Cirrus HD-OCT, Carl Zeiss Meditec, Inc, etc.) [11]. However, such standard OCT instruments do not give information on the phase retardation and birefringence of the RNFL.

Recently, Polarization Sensitive Optical Coherence Tomography (PS-OCT) has emerged as a promising new technique for glaucoma diagnosis. PS-OCT provides depth resolved morphological information along with sub-cellular information namely the birefringence [12]. In this dissertation, the RNFL thickness, phase retardation, birefringence and reflectance will be measured by Polarization-Sensitive Optical Coherence Tomography (PS-OCT). We would like to compare the performance of RNFL thickness, phase retardation, birefringence and reflectance on early diagnosis of glaucoma.

1.3 ORGANIZATION OF DISSERTATION

In Chapter 2, we introduce the instrumentation and describe the experimental procedures used for data collection. In Chapter 3, we investigate two registration

algorithms, a mutual information (MI) based algorithm and a log-polar transform cross-correlation (LPCC) based algorithm, for registration of OCT images. We also show effect of registration on longitudinal analysis of Retinal Nerve Fiber Layer Thickness in non-human primates using Optical Coherence Tomography. In Chapter 4, we show comparison of thickness, phase retardation, birefringence, and reflectance of the retinal nerve fiber layer in normal and glaucomatous non-human primates. In Chapter 5, we validate the findings of using Reflectance Index as the earliest indicator of glaucoma on clinical study on healthy human subjects, glaucoma patients and glaucoma suspect. We conclude our work and discuss the future research directions in Chapter 6.

Chapter 2: Instrumentation and Experimental Design

This dissertation describes the computational analysis of data from two experimental studies. The first study is a longitudinal glaucoma study on non-human primates. The second study is a clinical cross-sectional glaucoma study on human subjects.

2.1 LONGITUDINAL GLAUCOMA STUDY ON NON-HUMAN PRIMATES

2.1.1 Experimental procedures

Polarization sensitive OCT (PS-OCT) measurements were acquired in three macaque primates: two cynomolgus (macaca fascicularis), and one rhesus macaque (macaca mulatta). Using an established protocol [13,14,15], one eye of each primate was treated with an argon laser (488 nm and 514 nm) targeting the trabecular meshwork to induce an intraocular pressure (IOP) increase; the fellow eye was left untreated and served as a control. The three primates were followed for a period of 30 weeks during which weekly or biweekly PS-OCT imaging of the retina was performed to assess RNFL changes associated with elevated IOP. All studies reported were done under the direction of The University of Texas Institutional Animal Care and Use Committee and followed an approved protocol (#08013001), ensuring conformance with the ARVO Statement for the Use of Animals in Ophthalmic and Vision Research.

2.1.2 Glaucoma induction

To induce a sustained intraocular pressure (IOP) increase and induce glaucoma, we followed an animal model first described in 1974 [13] and used in many subsequent animal model glaucoma studies[14],[16],[17]. Photocoagulation is an accepted treatment option for open-angle glaucoma to lower the IOP. A similar procedure is followed for

glaucoma induction, except that a higher laser power is delivered and a more complete circumference of the eye is photocoagulated with the laser radiation causing trabecular meshwork scarring and reduced fluid outflow capacity resulting in a sustained IOP increase.

For trabeculoplasty, the primates were anesthetized using aqueous Telezol (4mg/kg) IM and a Ketamine (10mg/kg) booster as needed. Topical anesthetic (proparacaine hydrochloride) was applied prior to trabeculoplasty. A pediatric goniolens was inserted between the lids with a canthotomy being necessary in two of the eyes. The primates were placed in a prone position with the head facing forward and strapped against the headrest of a slit lamp (Coherent 930 argon laser with Zeiss slit lamp). A series of 200, argon laser pulses (50μm, 1W, 0.5s) were delivered to the complete trabecular meshwork. Post-op, 0.2 mg celestone was administered sub-conjunctivally to control inflammation. For this study, trabeculoplasty was done in one eye (OD) in each of the three primates and the other eye (OS) was left untreated as a control. A sustained IOP increase was induced in all of the treated eyes. Primate 1 required two treatments and primate 3 required four repeated treatments (Figure 18) to induce a sustained IOP increase.

2.1.3 PS-OCT System Description

The PS-OCT system was similar to that described earlier [18], except that free-space optical components were utilized rather than optical fiber (see system diagram in Figure 2).

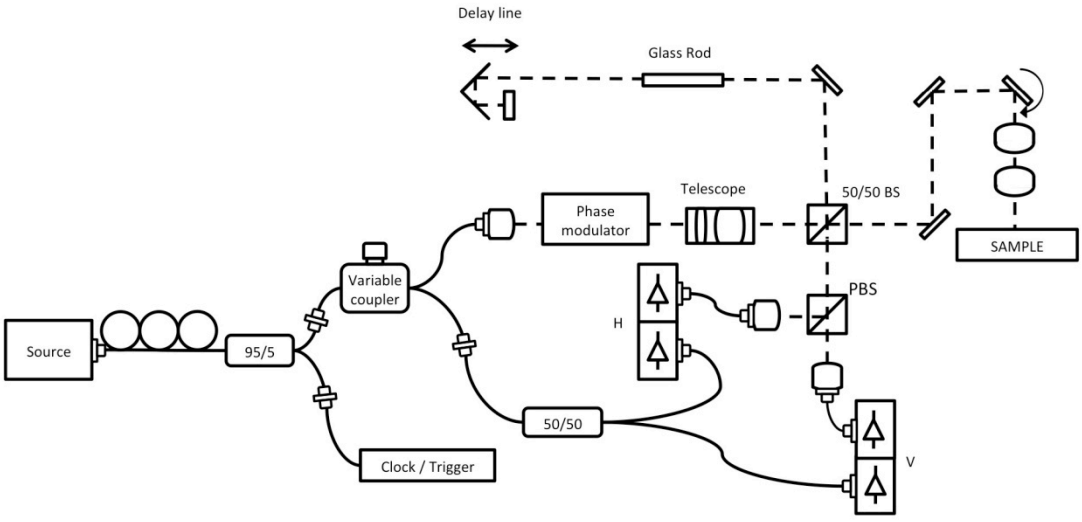

Figure 2. PS-OCT system diagram. BS is beamsplitter, PBS is polarizing beamsplitter.

Briefly, the PS-OCT system uses a 1 μm center wavelength swept laser source (Santec, HSL 1000) with an axial resolution of 12 μm and lateral resolution of 25 μm. Average incident power on the primate cornea was 1.13 mW. The PS-OCT system was a custom-built tabletop research instrument constructed for the purpose of this study. Polarization sensitivity was provided by positioning an electro-optic phase modulator (New Focus, Santa Clara, CA) in the interferometer source path to control the polarization state of light input into the interferometer. Polarization diverse detection was achieved with a polarizing beam splitter and separate detectors for the two orthogonal polarization channels. The phase modulator provided three sequential input polarization states incident on the primate's eye separated by 120 degrees on the Poincare sphere [19].

2.1.4 Imaging Procedures

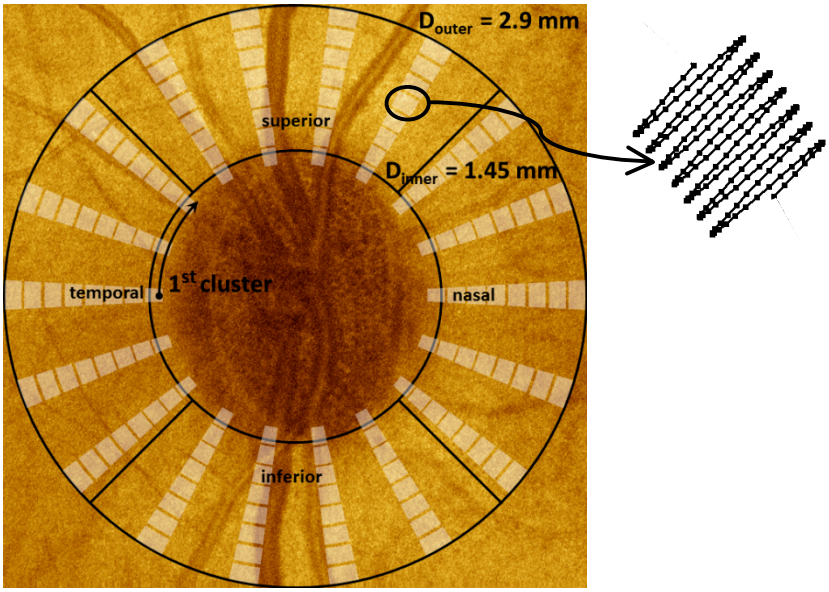

Figure 3. Schematic showing clustered imaging regions overlaid on a fundus image with marked quadrants. Sampling within a cluster is shown at the upper right. The clustered pattern collects 200 A-Scans over a small region; these A-scans are averaged to reduce noise in estimates of the polarization parameters.

Two scan patterns were utilized to record images of the primate RNFL. RI and RNFL thickness parameters determined from continuous ring scan measurements are continuously sampled throughout the measured region while the clustered scan measurements are sampled in small regions around a central location. Continuous ring scan images were recorded to provide a fundus image and blood vessel map in order to register images acquired on different dates. Continuous ring scan images consisted of 100 B-scans each comprised of 360 A-scans at a fixed radial distance from the ONH. Successive A-scans were separated by 1 degree and successive B-Scans were spaced radially by 15 μm. Clustered ring scan images were recorded to provide the polarimetric

data required to deduce RNFL birefringence and phase retardation. Clustered ring scans consisted of 8 circumferential retinal B-scans at a fixed radial distance from the ONH (see Figure 3 above). Each of these B-scans contained 18 evenly spaced clusters each consisting of 200 A-scans recorded over a sine wave pattern with 10 μm A-scan spacing. Prior to each imaging session, an IOP measurement was performed with a Tono-Pen VET^{TM} (Reichert, Depew, NY).

2.1.5 ONH Placement

The imaging procedure required mechanically stabilizing the primate's head and eyes. Just before recording images, each primate was positioned supine for alignment with the PS-OCT scanning optics. The primate's head was mounted in a cushioned cradle and maintained in a stable position using a custom rubber mask that was fitted around the nose and mouth to allow interface with anesthesia apparatus. The mask was attached to the cradle to securely hold the head. The entire fixture, including the primate's head, could be translated laterally over a distance of approximately 25 mm to allow positioning of the pupil in line with the PS-OCT scanning optics. Orthogonal goniometers permitted rotation of the primate's head and allowed for the ONH head to be centered in the scan range of the PS-OCT imaging beam. Temporary sutures were inserted at the limbus on the nasal and temporal sides of the eye to prevent eye motion. These sutures were gently placed under tension and affixed to the stationary facemask. The pupils were dilated prior to imaging using 1% tropicamide to maximize light throughput to the retina. A drop of 10% methylcellulose was placed on the cornea and a custom spherical PMMA 8.4 mm diameter contact lens was placed on the eye to neutralize refractive error in each primate eye. The lens curvature was 6.2 mm with powers ranging from +3 to -5 diopters.

During the initial alignment process, the PS-OCT imaging system was continually cycling a rectangular raster scan pattern and updating a fundus image for visualization,

alignment, and centering of the optic nerve head. This fundus image, similar to that provided by a standard ophthalmoscope, was displayed in real time by summing pixels along the axial direction.

These data from the non-human primate model are used in Chapter 3 for investigating the LPCC and MI registration algorithms and evaluating the effects of registration on longitudinal estimation of RNFLT. These data are also used in Chapter 4 for investigating candidate markers for early glaucoma diagnosis in longitudinal glaucoma study on non-human primates model.

2.2 CLINICAL GLAUCOMA STUDY ON HUMAN

2.2.1 Subjects and Study protocol

Two study groups are presented. The first group consists of 34 eyes including 13 healthy, 9 glaucomatous, and 12 glaucoma suspect eyes from 33 human subjects enrolled at the Eye Institute of Austin (EIA). The second group consisted of 41 eyes including 20 healthy, 15 glaucomatous, and 6 glaucoma suspect eyes from 38 human subjects enrolled in the study at the Duke Eye Center (DEC). Both eyes of each participant were assessed in this study. For each subject with the same diagnosis for both of his/her eyes (e.g., both glaucomatous), we selected one of his/her eyes for each analysis; the selected eye was the one for which the best quality images were obtained for the particular instrument under consideration in the analysis. For glaucoma patients with one glaucomatous eye and one glaucoma suspect eye, we include both eyes in the data analysis since our study is not concerned with direct comparison of glaucomatous and glaucoma suspect eyes. The age and gender distributions for each subject category are shown in Figure 4 and Figure 5.

Eligibility for a human participant is based on medical and ocular history and a comprehensive eye examination (including standard disc photography and Humphrey-

Zeiss 24-2 visual field test) by a glaucoma specialist. The inclusion criteria are age between 40 and 80; visual acuity score of 20/40 or better; spherical refraction within ± 5 diopters; and cylinder refraction within ± 3 diopters. The exclusion criteria are discernable anomaly of the anterior chamber; uveitis; significant opacification of the cornea or crystalline lens; concurrent active eye disease in the study eye that may affect intraocular pressure or its measurement; eyes with secondary glaucoma or acute narrow angle glaucoma; eyes with pigmentary or pseudoexfoliation glaucoma; eyes with proliferative or severe nonproliferative diabetic retinopathy, retinal detachment, retinitis pigmentosa, or other significant retinopathy; eyes with field loss attributed to a non-glaucoma condition, dilated pupil diameter less than 4mm, and visual fields < 20 degrees; patients on kidney dialysis and any physical or mental impairment affecting the patient's ability to perform any study tests.

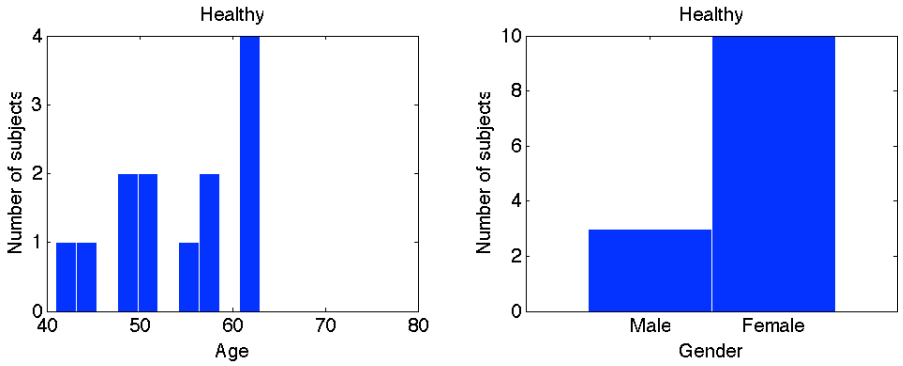

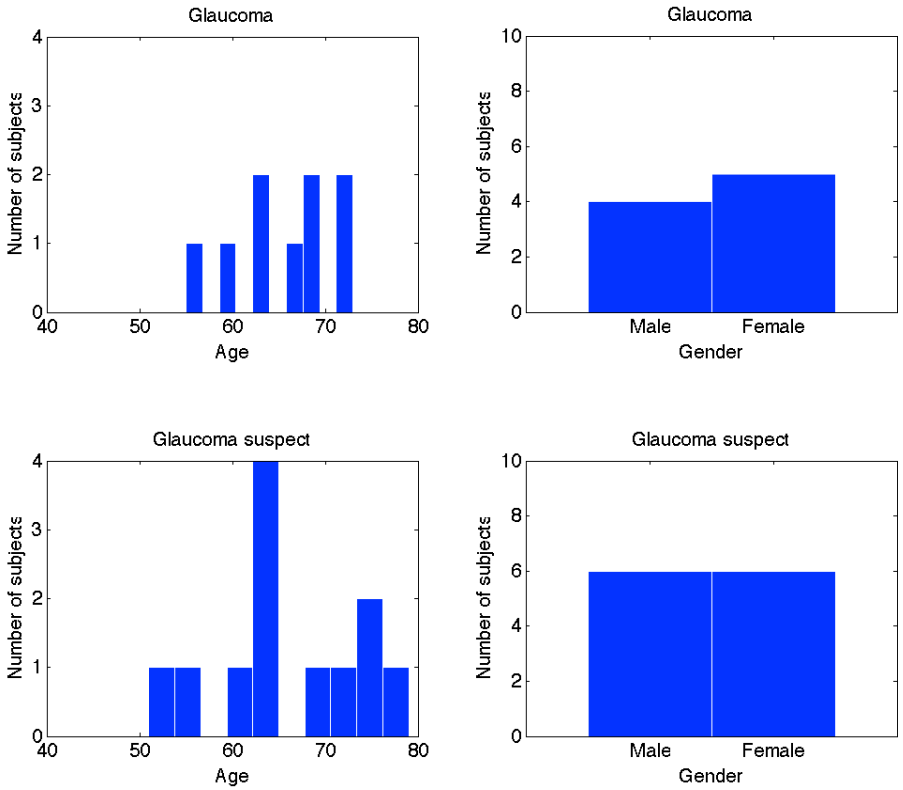

Figure 4. Age (years) and Gender distribution of healthy subjects, glaucoma patients, and glaucoma suspects from the study at the Eye institute of Austin (EIA).

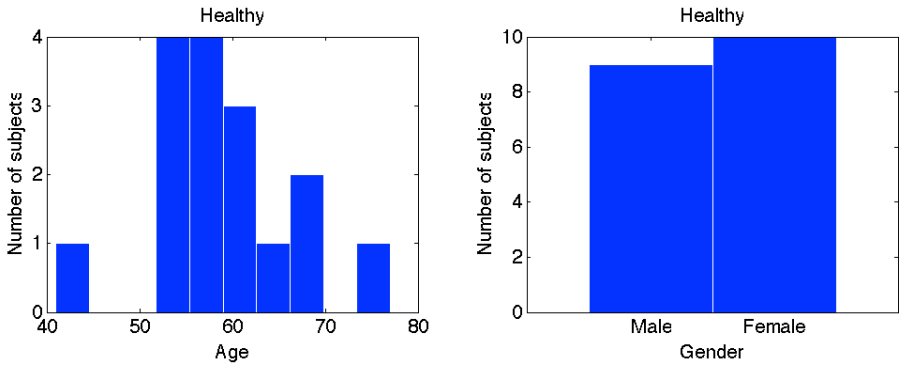

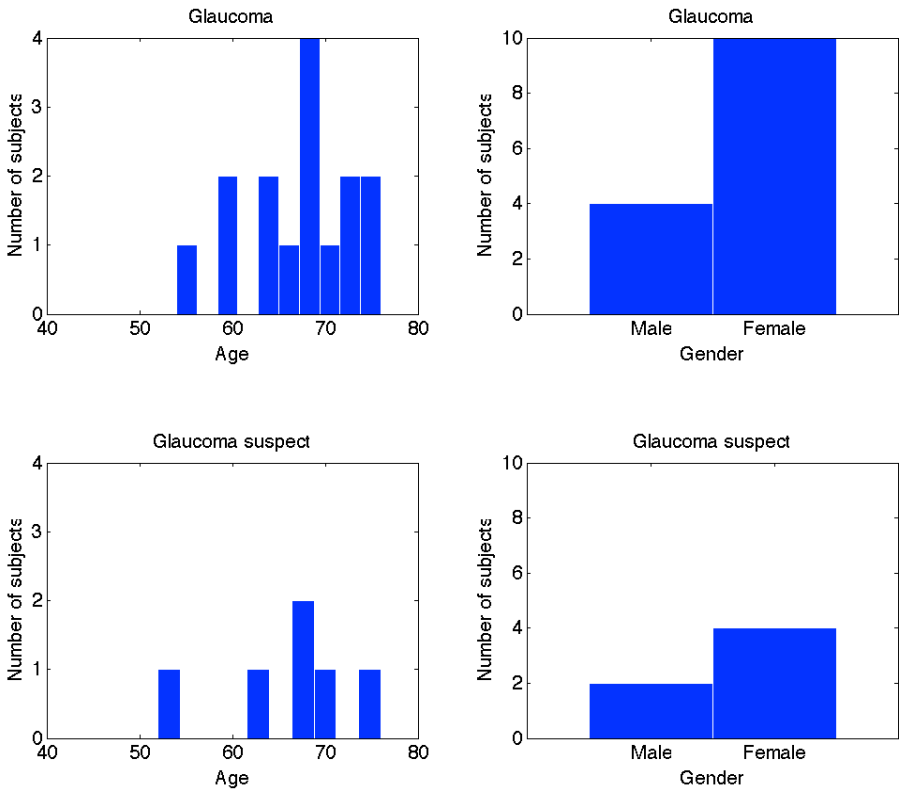

Figure 5. Age (years) and Gender distribution of healthy subjects, glaucoma patients, and glaucoma suspects from the study at the Duke Eye Center (DEC).

Healthy control eyes are defined as IOP<21 mmHg with no history of elevated IOP, normal visual fields [mean deviation and pattern standard deviation (PSD) within 95% confidence limits and Glaucoma Hemifield Test (GHT) normal limits], and no optic disc abnormalities. Glaucomatous eyes are defined as history of elevated IOP, two consecutive abnormal visual fields (PSD outside the 95% confidence limits, abnormal GHT, or any abnormalities listed under visual fields, and abnormal optic disc. An effort was made to recruit early and moderate glaucoma defects on the Hodapp-Parrish-Anderson grading scale. Glaucoma suspect eyes are those that meet the definition of Primary Open Angle Glaucoma Suspect by the American Academy of Ophthalmology's Preferred Practice Pattern[6]. There are two types of glaucoma suspect included in this

study. The first type is ocular hypertension. The subjects with ocular hypertension should have intraocular pressure higher than 21 mmHg but not more than 30 mmHg measured in at least 3 separate visits and have normal optic nerve head appearance. The second type is preperimetric glaucoma. Subjects with preperimetric glaucoma were defined as patients with an asymmetric cup-to-disc ratio and showed early glaucomatous optic disc abnormality, including thinning of neuroretinal rim and notching. All subjects belonging to the glaucoma suspect group had normal visual field results as defined in the healthy group.

This study was approved by the Institutional Review Board at The University of Texas at Austin and at Duke University Medical Center (NCT #01222065). All methods adhered to the tenets of the Declaration of Helsinki for research involving human subjects. All participants of this study gave informed consent and could withdraw from the study without jeopardizing eye care.

2.2.2 Instrumentation

We used two different spectral domain OCT systems and the GDx VCC system for retina imaging in this study. The first instrument is a Polarization-Sensitive Swept-Source Spectral Domain Optical Coherence Tomography (OCT) system developed by our lab and described in one of our previous publications[12]. A clustered ring scan consists of 36 clusters of 100 A-lines per ring, corresponding to an angular separation of 10 degrees (p/18 radians) and 10 concentric rings about the optic nerve head with equidistant between rings. The innermost diameter is 2 mm and outermost diameter is 5 mm for the study conducted at the Eye Institute of Austin. The innermost diameter is 1.5 mm and outermost diameter is 5 mm for the study conducted at the Duke Eye Center. Because of the innermost diameter difference in the scanning pattern, we didn't combine

the dataset aquired by PS-OCT from EIA and Duke for analysis. 100 A-lines per cluster were found to offer a good compromise between polarimetric signal-to-noise ratio (PSNR) and acquisition time[20]. To ensure speckle fields are uncorrelated, A-line separation was set at 10 mm - 14 mm, equivalent to system speckle size. Averaging $N_A = 100$ uncorrelated A-lines increases PSNR by approximately $\sqrt{N_A} = 10$ [20].

Spectral domain OCT examination was also performed with the RTVue FD-OCT (software version 4.0.5.39, Optovue, Inc., Fremont, CA). RTVue uses a scanning laser diode with a wavelength of 840 nm. The protocols used for imaging with RTVue in this study were ONH (optic nerve head). The scanning pattern was different from what we used in PS-OCT system. 13 ring scans around the ONH were taken by RTVue OCT. The innermost diameter is 1.3mm and outermost diameter is 4.9mm. RNFL phase retardation maps were also measured with a corneal-compensated scanning laser polarimeter (GDx-VCC, Carl Zeiss Meditec, Inc., Dublin, CA). The GDx converts phase retardation into RNFL thickness assuming a constant RNFL birefringence. All patients were examined using these three instruments during the same visit.

The data from the experimental study introduced in 2.1 are analyzed in Chapter 3 and Chapter 4. The data from the study described in 2.2 are analyzed in Chapter 3 and Chapter 5.

Chapter 3: Image registration of retinal blood vessel images from OCT

In this chapter, we investigate two image registration algorithms, a mutual information (MI) based algorithm and a log-polar transform cross-correlation (LPCC) based algorithm on blood vessel images from non-human primates eyes and human eyes. The data analyzed in this Chapter are from the experimental studies described in Chapter 2. We submitted one journal paper about the study described in section 3.1 to Investigated Ophthalmology & Visual Science[21]. This paper is under revision now. We submitted one conference paper about the study described in section 3.2 to 34th Annual International Conference of the Engineering in Medicine and Biology Society [22].

3.1 Effect of registration on longitudinal analysis of retinal nerve fiber layer thickness of non-human primates using Optical Coherence Tomography (OCT)

3.1.1 Motivation

Estimation of retinal nerve fiber layer thickness (RNFLT) is an important step in both glaucoma diagnosis and detection of glaucoma progression. Optical Coherence Tomography (OCT) can objectively and quantitatively measure RNFL thickness. Because RNFLT maps measured by OCT are highly correlated with visual field loss [23,24,25], OCT can be used to assist in glaucoma diagnosis and longitudinal detection of glaucoma progression.

Studies suggest higher repeatability and reproducibility in measuring RNFLT of healthy and glaucomatous eyes with commercially available spectral-domain OCT compared to time-domain OCT instrumentation [26,27,28]. However, causes of measurement variability, for example, manual placement of the scan circle by the instrument operator and patient eye rotation during successive measurements, remain problematic. In monitoring glaucoma progression, small changes of RNFLT might be

missed and false changes of RNFLT might be detected because of misalignment of successive RNFLT maps. Therefore, accurate registration of maps recorded at different OCT imaging sessions is desired for assessment of glaucoma progression. Recently, methods including tracking systems and scan alignments based on the optic nerve head have been developed to improve image registration and RNFLT measurement reproducibility. Some of the latest versions of commercially available spectral domain OCT software also incorporate methods to enable serial analysis of RNFLT changes. For example, the Spectralis OCT (Heidelberg Engineering, Heidelberg, Germany) uses a system to track eye movements and enable "real-time" registration. The OCT software package RTVue FD-OCT (Optovue, Inc., Fremont, CA) uses post-processing methods based on baseline images to enable registration. Previous studies have shown that evaluation of RNFLT might be affected by variations in the position of the scan circle of measurements around the optic nerve that can compromise measurement reproducibility in eyes of healthy human subjects [29,30]. However, no study has reported on whether image registration can improve longitudinal RNFLT evaluation in healthy eyes and which RNFLT features may be more sensitive to misalignment of RNFLT maps recorded on different dates.

In this longitudinal study, we investigated algorithms based on mutual information (MI) and log-polar transform cross-correlation (LPCC) for registration of retinal maps recorded using a spectral domain OCT instrument of healthy non-human primates based on retinal blood vessel locations. We chose to investigate MI and LPCC algorithms because they were demonstrated as two robust approaches for retinal image registration [31,32,33,34]. We evaluated change of 17 different RNFLT features calculated from the retinal maps (all rings average, TSNI quadrants average and 12 clock hour sectors average) with and without registration over a 30-week time period.

3.1.2 Methods

(a) Datasets

The left eye of each primate as described in chapter 2 was used in this study. Poor quality scans were rejected by the instrument operator. Two scanning patterns were used to generate retinal maps. For each primate eye, one raster scan was performed on a 3 × 3 mm^2 square area centered on the optic nerve head (ONH) and used to create a raster scan fundus image that was used as the baseline image for the respective primate eye. Each raster scan was comprised of 100 B-scans and each B-scan consisted of 256 A-scans. A second scanning pattern was a continuous ring scan pattern that contained 100 equally spaced ring B-scans centered on the ONH with ring diameters ranging from 1.5 mm to 3.0 mm. Each B-scan contained 100 A-scans. Data recorded from continuous ring scans were used to create an RNFL thickness map of each eye. Fundus images of continuous ring scans were also created for registration purposes as target images (Figure 6).

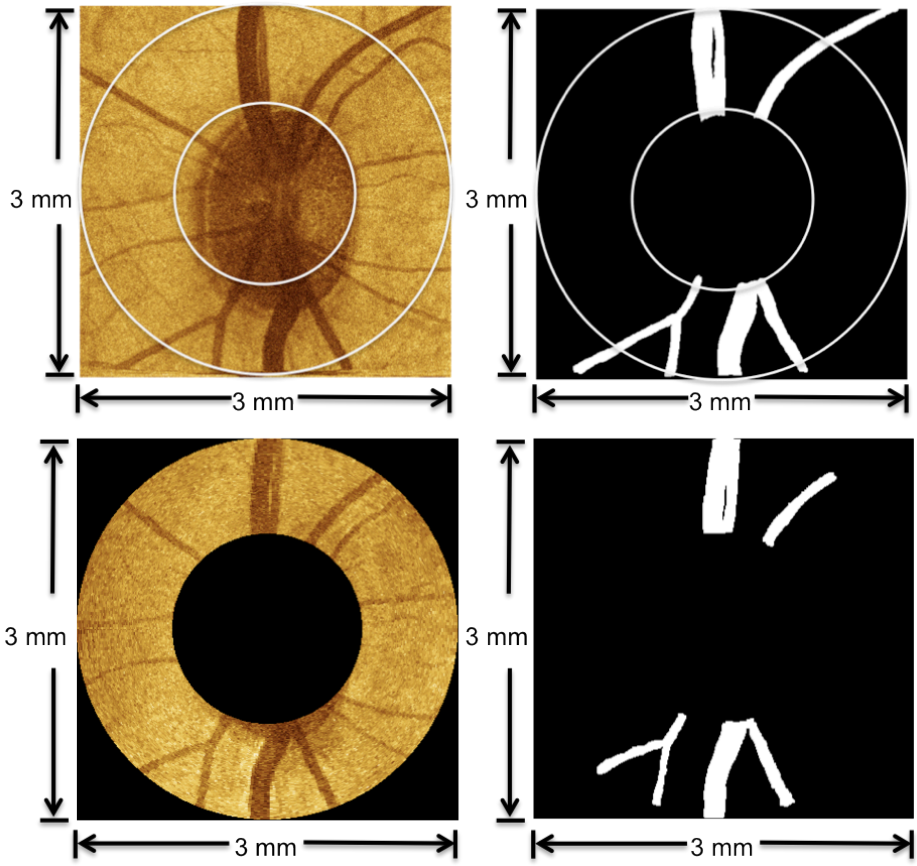

Figure 6. Images in the top row are derived from a raster scan fundus image (top, left) and manually segmented blood vessels (top, right). One raster scan fundus image is selected for each primate eye and the central area is used as the reference image for registration of RNFLT maps. Images in the bottom row are derived from a continuous ring scan fundus image (bottom, left) and manually segmented blood vessels (bottom, right). The continuous ring scan fundus image for each session is used as a reference image to register RNFL thickness maps.

(b) Retinal nerve fiber layer thickness (RNFLT) map and feature calculation

A LABVIEW software program (National Instruments, Austin, Texas) was implemented for the OCT system to automatically detect RNFL boundaries in each B-scan of continuous ring scans [12,35]. After RNFL boundary detection, an expert on OCT

retinal image evaluation visually inspected the boundaries overlayed on each B-scan to correct any misidentified boundaries. RNFLT values were then imported into MATLAB (The Mathworks, Natick, MA) for RNFL feature calculation. The most widely used feature parameters were computed including the all-rings average thickness, temporal, superior, nasal, and inferior (TSNI) quadrants average thicknesses, and each of the 12-clock hour RNFLT averages according to the OD clock-wise hours (Figure 7). Feature values are calculated on RNFLT maps before and after registration.

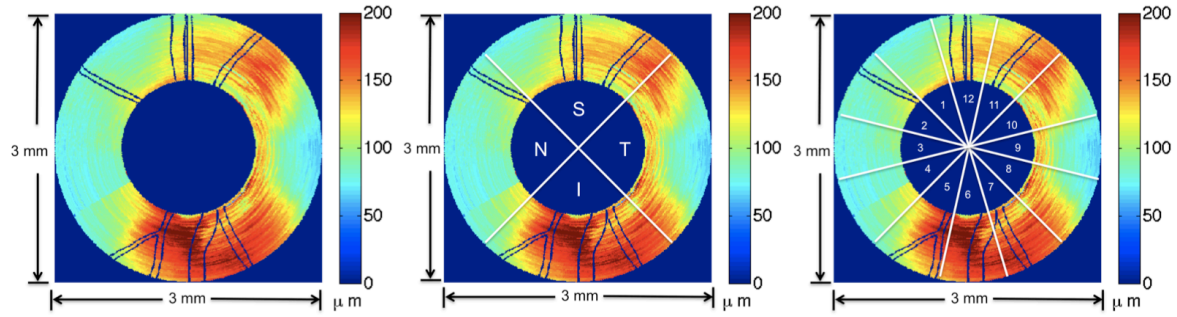

Figure 7. Feature parameter calculation of RNFLT map of a primate left eye (OS). Left is all-rings average of all 100 rings in RNFLT map. Middle shows the temporal (T), superior (S), inferior (I) and nasal (N) quadrants in RNFLT map. Right shows the 12 clock-hour sectors in the RNFLT map.

(c) Registration and evaluation method

One fundus image created from the raster scan is used as a reference image for each primate eye. All fundus images of continuous ring scans are target images and registered against this baseline image to ensure alignment of all RNFL thickness maps obtained with the continuous ring scan method. We applied two registration algorithms, a method based on mutual information (MI) and a log-polar transform based cross-correlation (LPCC) algorithm. The process of applying MI and LPCC algorithms and evaluation of precision and recall are shown in a flowchart (Figure 8). The original reference and target intensity images are used for the MI algorithm to determine the best

transformation factors to align the reference and target image pair. The manually segmented blood vessel images from reference and target images (Figure 6) are used for the LPCC algorithm to find the best transformation factors to align the reference and target image pair. Precision and recall between manually segmented blood vessels of reference and target image pairs are used to evaluate the alignment between image pairs before and after registration. Details of the algorithms and evaluation process are described in the following sections.

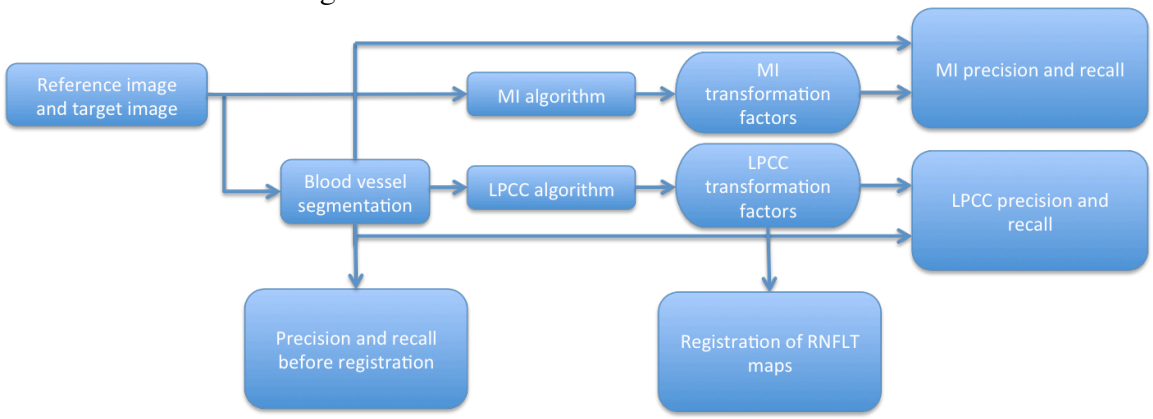

Figure 8. Flowchart diagramming application of MI and LPCC algorithms. Reference and target intensity images are used for the MI algorithm to find the transformation factors (translation, rotation, scaling) to register the image pair. The manually segmented blood vessel images of the reference and target images are used for the LPCC algorithm to find the transformation factors (translation, rotation, scaling) to register the image pair. The precisions and recalls between manually segmented blood vessels in reference and target image pairs before registration (bottom left), after MI registration (upper right), and after LPCC registration (lower right) are calculated. The LPCC transformation factors are used to register RNFLT maps.

Mutual information (MI) algorithm

We first use a mutual information (MI) algorithm to register RNFLT maps recorded on different days to the reference image [31,32,33]. The MI algorithm is performed on reference-target image pairs and does not require segmentation of the blood vessels. The MI registration algorithm holds the reference image fixed while the target image undergoes transformations until images are registered. Linear transformation factors included x- and y-translation, rotation and scaling. The mutual information between a reference (A) target (B) image pair is defined as:

$$\mathrm{MI}(A,B)=H(A)+H(B)-H(A,B) \quad (\mathbf{1})$$

Where $H(A)$ and $H(B)$ are the Shannon entropies of the reference (A) and target (B) images, respectively, defined as

$$\mathrm{H}(X)=-\sum_{i=1}^{N} p(x_i)\log p(x_i) \quad (\mathbf{2})$$

Where $p(x_i)$ is the probability of occurrence of the intensity value x_i in the image. Similarly, $H(A,B)$ is the joint Shannon entropy of images A and B, defined as

$$\mathrm{H}(A,B)=-\sum_{i,j} p(i,j)\log p(i,j) \quad (\mathbf{3})$$

Where $p(i,j)$ is the joint probability of the image intensity pairs in the joint histogram of images A and B. Two images are considered registered when $MI(A,B)$ has a maximum value with respect to the linear transformation factors.

We perform the MI registration in two major steps: a coarse registration step followed by a fine registration step. For coarse registration, we translate the target image from -25 to 25 pixels (approximately 0.15 mm) in both x and y directions with an interval of 5 pixels (approximately 0.03 mm), and rotate the image -10 to 10 degrees in 2 degree intervals until maximum mutual information between the reference and target images is

obtained. To reduce time for coarse registration, larger search intervals are used compared to those used subsequently in fine registration. Performing three transformations simultaneously helps to prevent the algorithm from stalling in a local maximum, which is more common if each type of transformation were to be performed separately. The coarse transformation parameters that provide the maximum mutual information (MI) are found and performed on the target image before fine registration.

In fine registration, all transformation parameters, translation, rotation and scaling are performed separately with smaller search intervals to maximize mutual information. We first do a scaling search for a scale factor between 0.85 to 1.15 with an interval of 0.01, then vary x-translation factor from -20 pixels to 20 pixels (approximately 0.12 mm) with an interval of 1 pixel (approximately 0.006 mm), then y-translation factor from -20 pixels to 20 pixels with an interval of 1 pixel, then rotation factor from -20 to 20 degrees with an interval of 0.1 degrees, and finally scaling again with search radius between 0.85 to 1.15 with an interval of 0.01.

Log-polar transform based cross-correlation (LPCC) algorithm

RNFLT maps recorded on different days are also registered to the reference image using a log-polar transform based cross-correlation (LPCC) algorithm [34]. We first manually segment the blood vessels in the original intensity reference and target images. Blood vessel images are mapped into log-polar coordinates so that rotation and scaling in the original image correspond to translation in log-polar images. Log-polar transformed images are then cross-correlated to determine the scaling and rotation factors. Because spatial-domain calculations, unlike frequency-domain computations, are not translation invariant, the log-polar transform and subsequent cross-correlation is completed for all possible choices of origin within a limited search area in the reference image. When the

maximum cross-correlation is found, the choice of origin corresponds to translation and shifts in log-polar space correspond to scaling and rotation. To speed-up the LPCC algorithm, search for the maximum is completed at two resolution levels, using the parameters from the courser level as an estimate of the parameters for the finer level.

Because the OCT instrument operator approximately centered the scan ring over the optic nerve head before recording data, images are roughly aligned, and registration is achieved within a limited range of translation factors. Translation factors between image pairs are limited to 40 pixels (approximately 0.23 mm) to improve registration speed. For coarse registration, the images are subsampled to $1/4^{th}$ the size, yielding 128 x 128 pixel images with 20 x 20 pixel (approximately 0.23 x 0.23 mm) search areas corresponding to x- and y-translation factors between -10 and 10 pixels (approximately 0.12 mm). Log-polar transforms of the target images with all possible choices of origin in the search areas are then cross-correlated with the transform of the reference image.

To reduce computation time, all cross-correlations are calculated using the fast Fourier transform (FFT). The cross-correlation is linear in the scaling direction but circular in the rotation direction. Therefore, the log-polar transforms of the images are zero-padded along the scaling axis but not the rotation axis.

The optimal scaling, rotation, and translation parameters determined from these cross-correlations are then applied to the target image before fine registration. For fine registration, the 512 x 512 pixel blood vessel images were used, and the translation factors were limited to -4 and 4 pixels (approximately 0.02 mm). The linear transformation was computed as in coarse registration using log-polar transforms and cross-correlations.

Manual segmentation of blood vessels

Manual segmentation of blood vessel images was needed for two aspects of this study. First, blood vessel segmentation is a necessary pre-processing step for registration using the LPCC algorithm. Second, we used the manual segmented blood vessels for calculation of precision and recall of reference-target image pairs to evaluate performance of MI and LPCC algorithms.

Segmentation of the blood vessels in both raster and continuous ring scan fundus images were completed manually. Using a tablet PC, the five widest blood vessels with branches in each fundus image were manually annotated.

Evaluation of the registration results

The MI and LPCC algorithms were evaluated in terms of precision and recall between manually segmented reference and target image pairs before and after registration. The overlapped scanning region of reference and target images is used for calculation of precision and recall. Precision and recall are defined as:

$$precision = \frac{N_{TP}}{N_{TP} + N_{FP}} \quad \textbf{(4)}$$

$$recall = \frac{N_{TP}}{N_{TP} + N_{FN}} \quad \textbf{(5)}$$

Where N_{TP} is the number of overlapping blood vessel pixels in reference and target images (true positives). N_{FP} is the number of blood vessel pixels in the target image but not in the reference image (false positives). N_{FN} is number of blood vessel pixels in the reference image but not target image (false negatives) (Figure 9). The algorithm with better performance is used for registration of RNFLT maps.

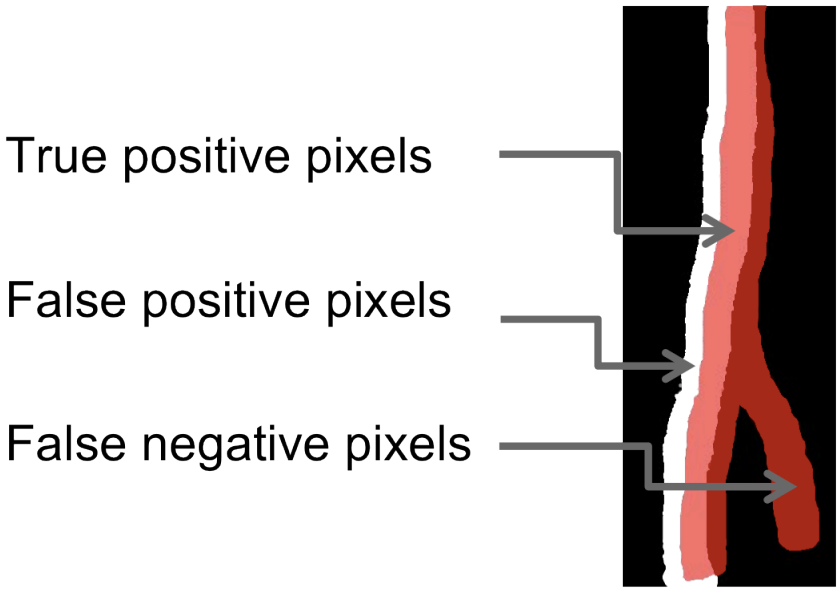

Figure 9. Definition of true positive (TP), false positive (FP), and false negative (FN) pixels for calculation of precision and recall. Red regions are the location of blood vessels in reference image while white regions are the location of blood vessels in target image. Blood vessel pixels that overlap in both reference and target images are marked as TP (light red). Blood vessel pixels in the target image but not in the reference image are marked as FP (white). Blood vessel pixels in the reference image but not the target image are marked as FN (dark red).

(c) Statistical analysis

Linear mixed-effects models were used for longitudinal evaluation of estimated RNFL parameters to capture both the similarity (fixed effect) and variations (random effects) among the three primates. Linear mixed-effects models also provide unbiased analysis of balanced and unbalanced repeated-measurement data, which is consistent with our experiment design. We used the R statistical programming language (v2.13.10 07/08/2011; http://www.R-project.org/, R Development Core Team, 2011, R Foundation

for Statistical Computing, Vienna, Austria) and R studio (v0.94, 06/15/2011, RStudio, Inc.) for implementing the linear mixed-effects models.

We first evaluated whether the precision and recall calculated for registered image pairs by MI and LPCC algorithms are improved significantly compared with no registration. We also use the precision and recall of image pairs registered by mutual information (MI) and log-polar based cross-correlation (LPCC) algorithms to compare the performance of these two algorithms. We used the following linear mixed effects model to evaluate the significance for the pairwise comparisons:

$$T_{i,t} = T_{avg} + b_i + \gamma \times reg_{i,t} + \varepsilon_{i,t} \qquad (6)$$

Where $T_{i,t}$ is precision or recall of the i[th] primate control eye on day *t* since the beginning of the study, T_{avg} is the mean precision or recall across all the eyes. b_i is a random effect representing the deviation from T_{avg} for the i[th] primate eye, normally distributed with zero-mean and standard deviation δ_b. $reg_{i,t}$ is a binary variable representing with($reg_{i,t} = 1$) or without registration($reg_{i,t} = 0$) for the i[th] primate control eye on day t when the model is used for comparison of precision and recall with and without registration. When the model is used for comparison of precision and recall of image pairs registered by MI and LPCC algorithm, $reg_{i,t}$ is a binary variable representing which algorithm is used for the i[th] primate control eye on day t ($reg_{i,t} = 0$ for MI algorithm; $reg_{i,t} = 1$ for LPCC algorithm). γ is the slope for $reg_{i,t}$. ε_{it} is a random effect representing the deviations in precision or recall on day *t* of the i[th] primate eye

from the mean precision or recall of the i^{th} primate eye and normally distributed with zero-mean and standard deviation $\delta\varepsilon$.

We investigated whether registration will affect the evaluation of RNFL thickness over time in this longitudinal study for healthy eyes. The following linear mixed effects model was applied,

$$RNFLT_{i,t}=(\alpha_1+\beta_i)+\alpha_2 \times t+\xi_{i,t} \qquad (7)$$

In the mixed effects model, $RNFLT_{i,t}$ is a feature value in RNFLT maps of the eye of the i^{th} primate on day t since the beginning of the study. The intercept α_1 and the mean slope α_2 for number of days *t* are fixed effects. The random effect is the change from the baseline intercept for i^{th} primate, β_i, which is normally distributed with zero-mean and standard deviation δ. $\xi_{i,t}$ is the random error component for the i^{th} eye on day t and assumed to be normally distributed with a mean of zero and standard deviation δ_e.

3.1.3 Results

(a) Comparison of MI and LPCC algorithms

Precision and recall were used to evaluate quality of registration results after application of MI and LPCC algorithms. Precision and recall between reference-target blood vessel image pairs of each primate eye were calculated before registration. Precision and recall between reference and target images of each primate eye were calculated after registration using the mutual information (MI) based and log-polar based cross-correlation (LPCC) algorithms (Figure 10). Precision and recall following registration by either the MI or LPCC algorithm were significantly better than that before

registration (p<<0.001). Thus, either the MI or LPCC registration algorithm could significantly improve alignment of reference and target images. Precision of the LPCC algorithm was significantly higher than that of the MI algorithm (p<<0.001). Recall of the MI based algorithm and recall of the LPCC based algorithm were not significantly different (p>0.05). Inasmuch as the results suggest the LPCC algorithm performs slightly better than the MI algorithm on the recorded primate images, we used the LPCC algorithm to register maps for analysis of RNFLT versus time.

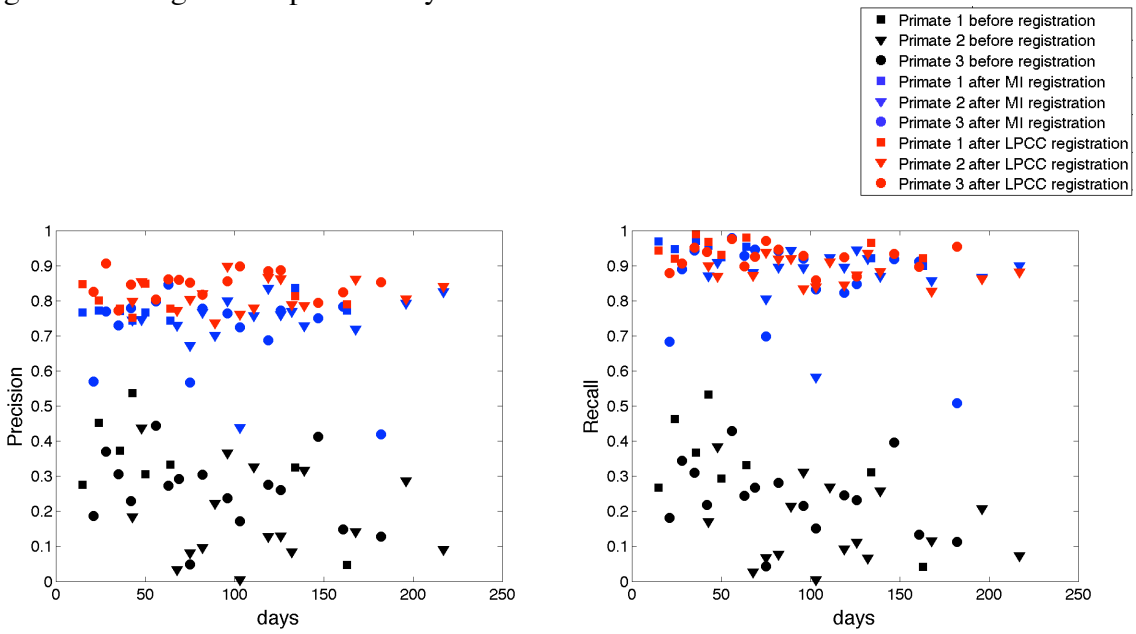

Figure 10. Precision (left) and recall (right) before (black) and after registration by MI (blue) and LPCC (red) algorithms. Precision and recall following registration by both MI (blue) and LPCC (red) algorithms are significantly better than values before (black) registration (p<<0.001). Precision of the LPCC (red) algorithm is significantly higher than that of the MI (blue) algorithm (p<<0.001). Recalls of LPCC and MI algorithms are not significantly different (p>0.05).

(b) Analysis of RNFL thickness over time with and without registration

We used a linear mixed effects model (Equation 8) to evaluate whether changes in retinal nerve fiber layer thickness (RNFLT) features occurred during the study duration. Before registration, RNFLT features are calculated in each map at each date. After registering all target images to a corresponding reference image using the LPCC algorithm, we co-aligned all RNFLT maps and use the overlapped region of all RNFLT maps from different dates to calculate the RNFLT feature parameter values. We found that prior to registration, three RNFLT features (1, 2, and 10 clock hour sectors averages) showed significant change during the study (Figure 11). Before registration, one and two o'clock hour sectors average RNFLT showed a significant decrease ($p<0.01$). Before registration, ten o'clock hour sector average increased significantly during the study duration ($p<0.05$). Other RNFLT features showed no change over the study duration. However, after registration, all RNFLT features, all model slopes of RNFLT feature vs. time are not significantly different from zero, suggesting all thickness feature parameter values are constant over the time course of the study. Since for healthy eyes, we would not expect the RNFL thickness to change significantly during the six months study duration [36], we conclude that consistency of RNFLT feature parameters improves after registration.

The results suggest that registration can remove artifacts introduced by misalignment of RNFLT maps especially in more detailed features like 12 o'clock hour sector average. Overall, the clock hour features of RNFLT are more sensitive to misregistration artifacts compared to the all-rings average and TSNI quadrants average.

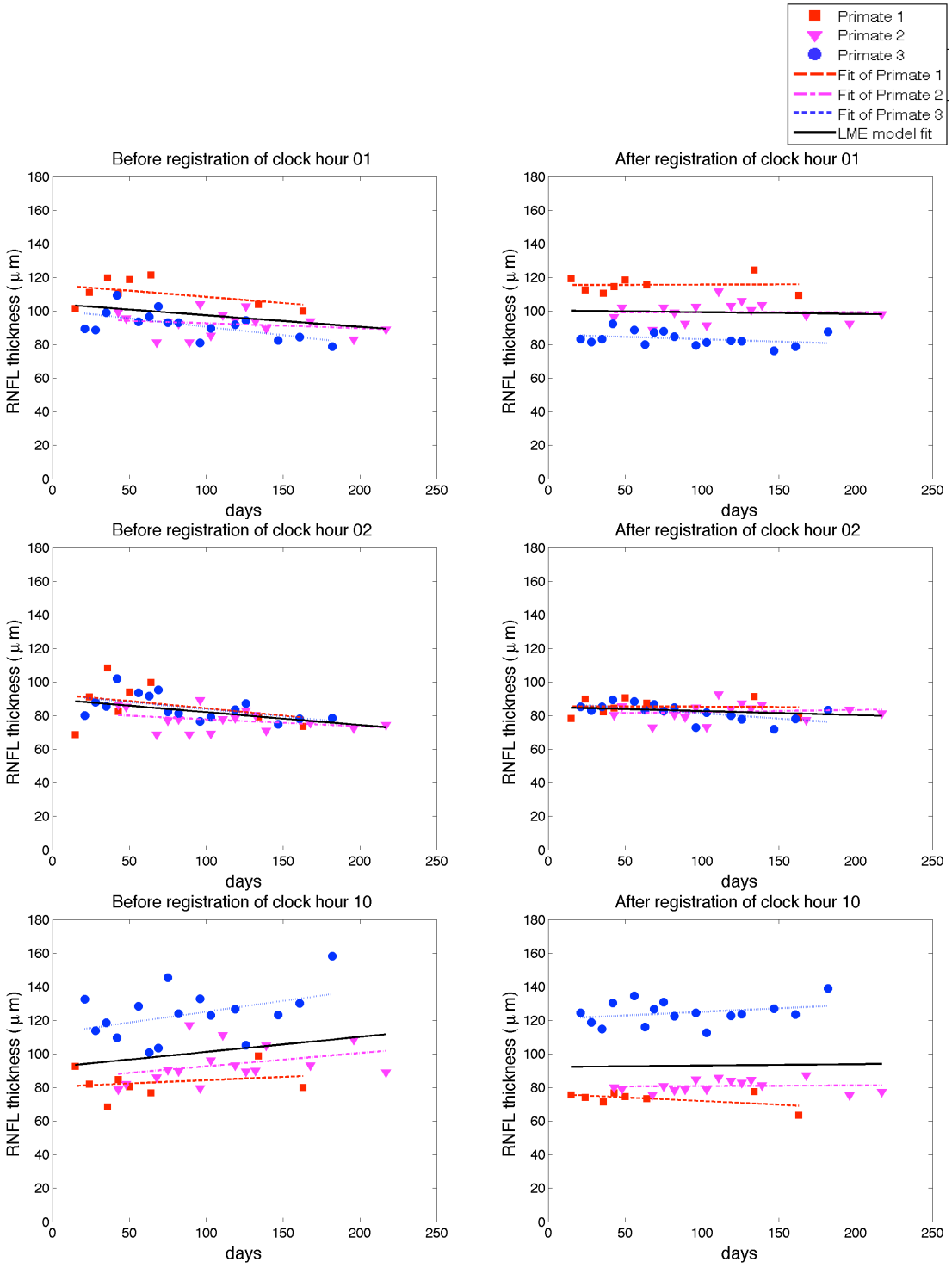
Primate 1
Primate 2
Primate 3
Fit of Primate 1
Fit of Primate 2
Fit of Primate 3
LME model fit
Before registration of clock hour 01
After registration of clock hour 01
Before registration of clock hour 02
After registration of clock hour 02
Before registration of clock hour 10
After registration of clock hour 10
RNFL thickness (μ m)
days

Figure 11. Estimation of change of RNFLT of clock hour 1, 2 and 10 average over time. The left column is before registration, right column is after registration. The dashed lines are the fits of individual primates. The individual fits display very similar trends as compared to the linear mixed effects model fits. The clock hour 1 and 2 averages decreased significantly before registration ($p<0.01$) but stay constant after registration. The clock hour 10 average RNFLT increased significantly before registration ($p<0.05$) but is constant after registration.

3.2 COMPARISON OF REGISTRATION ALGORITHMS ON HUMAN RETINAL BLOOD VESSEL IMAGES FROM OCT

3.2.1 Motivation

In order to compare RNFLT maps measured by OCT of a glaucoma patient across different imaging sessions, we need to co-register the maps to exclude the misalignments due to manual placement of the scan circle by the instrument operator and patient eye rotation in different imaging sessions. Moreover, registration is needed to find the same region of interest in RNFLT maps acquired by different scanning patterns since there are several patterns used in commercial instruments. Blood vessel images such as Line-Scanning Laser Ophthalmoscope (LSLO) images and fundus images created from OCT B-scans are usually used for registration of RNFLT maps. In section 3.1, we demonstrated the importance of registration of retinal blood vessel images from non-human primates' eyes [21]. In this section, we compared the performance of a mutual information (MI) based algorithm and a log-polar transform cross-correlation (LPCC) based algorithm on blood vessel images from human eyes.

3.2.2 Methods

(a) Dataset

The study included 9 healthy subjects, selected from the human clinical study described in Chapter 2. Two types of blood vessel image sets are acquired from each subject in this study.

The first image sets are LSLO images from two different imaging sessions during the same visit of the same subject (Figure 12). The LSLO image covers approximately a 1.5 by 1.5 cm square region on the retina. The two LSLO images from one subject formed a temporal image pair, which was then registered using the registration algorithms.

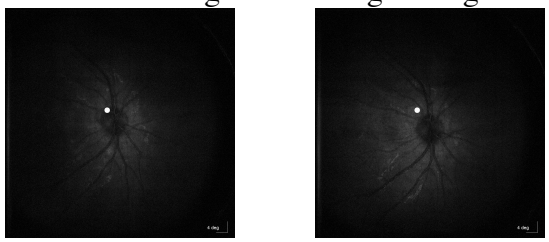

Figure 12. LSLO images of the same eye from two different imaging sessions during the same visit. The LSLO image covers a 1.5 by 1.5 cm square region on the retina.

Figure 13. Raster scan fundus image and continuous ring scan fundus image.

The second image sets are fundus images created from the B-scan images in two imaging sessions for the same subject by two different scanning patterns, the raster scan pattern and the continuous ring scan pattern (Figure 13). The raster scan is performed on a 6 by 6 mm square area and used to create a raster scan fundus image. There are 100 B-

scans in each raster scan session, and there are 256 A-scans in each B-scan. The continuous ring scan pattern contains 100 equally spaced ring B-scans centered on ONH with the innermost ring diameter of 1.5 mm and outermost ring diameter of 5 mm. The fundus images from the two scanning patterns are registered using MI and LPCC algorithms.

(b) Blood vessel and ONH detection

The registration and evaluation methods are similar to the ones described in 3.1.2. One extra step is to do automatic blood vessel detection and ONH detection. In order to improve the performance of the LPCC based algorithm, we first detected the ONH and blood vessels in reference and target image pairs. In LSLO images, blood vessels are detected in a ring around the optic nerve head (ONH). In the raster scan fundus images, blood vessels are detected in the entire image excluding a circle around the ONH. In continuous ring scan fundus images, blood vessels are detected throughout the scanning ring. Therefore, in both the LSLO and raster scan images, the center of the ONH must first be automatically detected. Since the size and shape of the ONH is relatively constant across subjects and since the ONH appears darker than the background region in the images, a matched filter that utilizes these characteristics is used. The images are cross-correlated with a circle approximately 1.4 mm in diameter (120 pixels in the 500 by 500 pixel raster scan images and 70 pixels in the 500 by 500 pixel LSLO images). Because the ONH is typically located near the center of the image, the ONH is assumed to be within a circular region centered at the middle of the image and empirically optimized to have a radius of 125 pixels (1.45 mm) for raster scan images and 55 pixels (1.1 mm) for LSLO images. The location of the maximum of the cross-correlation within this search region is used to determine the ONH location. However, since the LSLO images are

darker near the edges, the cross-correlation peak may correspond to a location closer to the edges instead of the actual ONH position. Therefore, if, for an LSLO image, the detected ONH location is on the circumference of the search circle, it is assumed that the ONH localization failed, and the center of the image is returned.

The blood vessels are then detected. The images are first preprocessed to enhance contrast and reduce noise. Since, in images from OCT, blood vessels appear to be of lower intensity, an increase in contrast enables more blood vessel edges to be detected. The Wiener filter is applied to smooth images (in order to decrease false detections by the edge detector) while preserving edge information. Edges are detected in the processed images using a standard Canny edge detection algorithm. Edge-strength and object-size thresholding are subsequently used to remove extraneous edges from the binary images (Figure 14).

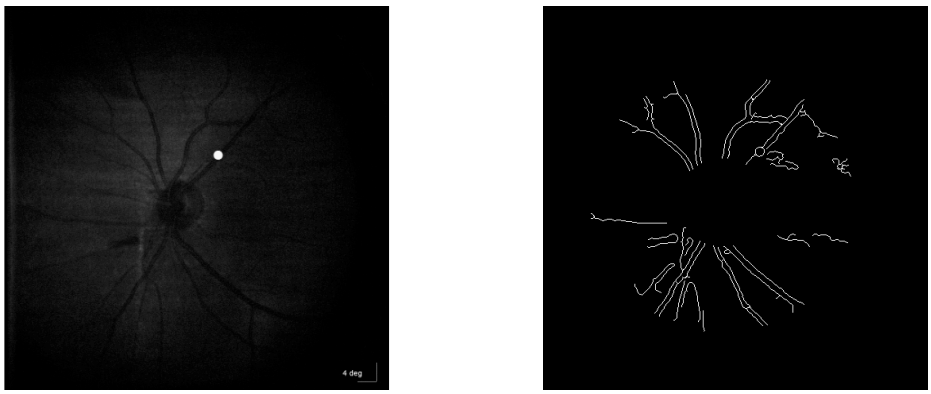

Figure 14. LSLO image and binary edge image that is the result of preprocessing and Canny edge detection.

Using the edge information, blood vessels are identified and filled in based on assumptions about the nature of most vessels. Since typical blood vessels are characterized by their length and narrow, unvarying width, the small and essentially unvarying distance between sets of adjacent, continuous edges is used to identify

candidate blood vessels. It is then ensured that candidate vessels are radially oriented with respect to the ONH and are of lower intensity than the locally surrounding background area. Regions with all these characteristics are considered blood vessels, and all pixels between the edges are filled.

Some less common vessel patterns do not fit the assumption of two straight, continuous, parallel lines (Figure 15). Vessel bifurcations and vessels whose boundaries are connected by an extraneous edge are identified and filled after more typical vessels are handled. The resulting binary blood vessel segmentations are then registered (Figure 16).

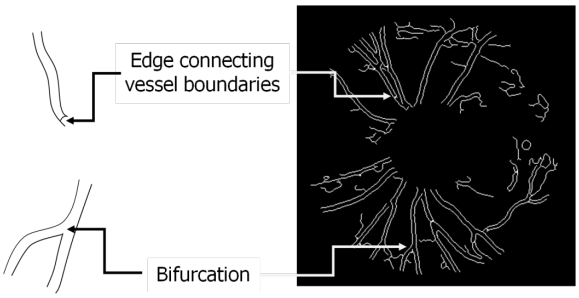

Figure 15. Special cases of vessels: Edge connecting vessel boundaries and Bifurcation.

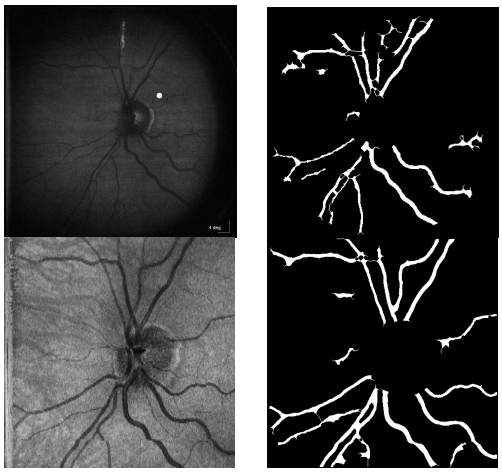

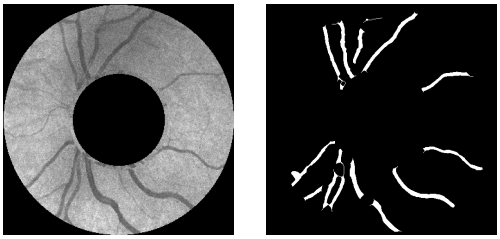

Figure 16. Blood vessel detection on an LSLO image (top), a raster scan image (middle), and a continuous ring scan image (bottom).

3.2.3 Results

(a) Registration results of LSLO images

For LSLO images, the average precision and recall of the segmented image pairs before registration were both 0.32±0.07. The average precision and recall of the segmented image pairs after registration using MI algorithm were 0.59±0.02 and 0.78 ± 0.04, respectively. The average precision and recall of the segmented image pairs after registration using LPCC algorithm were 0.60 ± 0.02 and 0.87 ±0.02, respectively. The precision and recall were significantly better following MI and LPCC registration ($p<0.001$ for both precision and recall). The gain in recall after registration using LPCC algorithm was significantly larger than the one obtained by registration with the MI algorithm ($p<0.05$). The gains in precision after registration using both algorithms were not significantly different ($p>0.05$). The LPCC algorithm performed better than MI algorithm on registration of LSLO image pairs.

(b) Registration results of raster scan and continuous ring scan fundus images

For registrations between raster scan and continuous ring scan fundus images, the average precision and recall of the segmented image pairs before registration were 0.16±0.05 and 0.19±0.06. The average precision and recall of the segmented image pairs

after registration using MI algorithm were 0.41±0.04 and 0.63 ± 0.06, respectively. The average precision and recall of the segmented image pairs after registration using LPCC algorithm were 0.51 ± 0.04 and 0.79 ±0.07, respectively. MI and LPCC registration algorithms both significantly improved precision and recall calculated between the segmented image pairs ($p<0.001$). The gains in precision as well as recall of both algorithms were not significantly different ($p>0.05$). This was probably due to the small sample size; the power to find a significant difference between the precision gains was only 5% and similarly the power to find a significant difference between the recall gains was only 6%. Thus, a larger dataset would be needed to determine if there was more benefit to using one registration rather than another for this application.

3.3 DISCUSSION

In this Chapter, we first investigated benefits of image registration on estimation of longitudinal RNFL thickness (RNFLT) changes in non-human primate eyes using mutual information (MI) and Log-polar transform based cross-correlation (LPCC) algorithms. Precision and recall calculated between manually segmented blood vessel image pairs were used for comparison with that determined after applying LPCC and MI algorithms. Results indicate application of either MI or LPCC algorithms improves the alignment between target and reference images compared to no registration. The precision after registration by the LPCC algorithm is significantly higher than that after registration by the MI algorithm. Similar recall is obtained following registration by either MI or LPCC algorithms. The computation time of the LPCC algorithm was five-times faster than that of the MI algorithm. However, this computation time does not include the pre-processing time required to segment the blood vessels before application of the LPCC algorithm. Both MI and LPCC algorithms showed good performance for

registration of fundus images of primate eyes and thus have potential for application to OCT image data recorded from human eyes.

This study is the first to evaluate how registration can affect the analysis of RNFLT measurement in a longitudinal study on healthy eyes using a non-human primate model. We evaluated the registration effect on all reported RNFLT feature parameters, which includes all-rings average, TSNI quadrants average, and 12 clock hours average. The results suggest that RNFLT feature parameters evaluated in the 12-clock hours are affected by registration in a longitudinal study in healthy primate eyes. Registration can correct the artifacts introduced by misalignment of RNFLT maps recorded on different dates. Registration allows detection of changes of detailed features and prevents false detection of changes due to misalignment. Moreover, any analyses associated with the all-rings average and TSNI quadrants average are not affected by the registration. Misalignment of a series of RNFLT maps is a candidate reason that previous studies showed that the all-rings average is the most robust feature in *reproducibility* studies [26,37]. Results suggest the 1, 2, and 10 clock hour sectors are the most sensitive to registration errors in this study, possibly because these clock hour sectors are located in regions with a large RNFLT gradient. Intuitively, sectors that are in RNFLT gradient transition zones should be more sensitive to misregistration than sectors in smooth areas of RNFLT maps. Therefore, without registration, the variations of RNFLT features across different dates are due to misalignments among RNFLT maps plus the reproducibility error introduced by the instrument. With registration, the variations of RNFLT features across different dates are primarily due to the reproducibility error introduced by the instrument.

The first study in this Chapter is performed on non-human primates. Due to the difference of eye fixation method during imaging acquisition, primate experiments

magnify rotation artifacts because of the suture positioning process that was done to bring the primate's ONH into the center of the field of view. In a clinical setting where a patient can fixate on a target, human eyes may have smaller rotation variation from one imaging session to another. However, human eyes can still exhibit comparable translation factors to primate eyes because this effect is primarily due to the variability in the operator's placement of the scanning ring around the ONH. We conclude from this study that registration has the potential to improve glaucoma detection in human eyes. Consequently, in the second study described in this Chapter, we compared the performance of LPCC and MI algorithms on human retina blood vessel images. Consistent with our prior research with non-human primates, this study demonstrates that both MI and LPCC based algorithms can successfully register LSLO image pairs for human eyes. The LPCC based algorithm performed significantly better than the MI based algorithm on registering LSLO images. These results on registering the same type of image pairs from human eyes are also consistent with those of our previous work on primates' eyes, which validates our findings on primates' eyes on human eyes. Both MI and LPCC algorithms also can successfully register the raster scan and continuous ring scan fundus image pairs. For registering raster scans and continuous ring scan fundus image pairs, the performance of MI and LPCC algorithms were not significantly different based on the small sample size we have. In order to achieve 80% power to find significant differences between precision gains of MI and LPCC algorithms, we would need to include at least 1500 samples. In order to achieve 80% power to find significant differences between recall gains of MI and LPCC algorithms, we would need to include at least 614 samples. Thus, whether one registration algorithm or another is more beneficial for this application cannot be determined until larger scale studies are performed.

Chapter 4: Thickness, phase retardation, birefringence, and reflectance of the retinal nerve fiber layer in normal and glaucomatous non-human primates

In Chapter 4, we identify candidate markers for early glaucoma diagnosis. We measure time variation of retinal nerve fiber layer (RNFL) thickness, phase retardation, birefringence, and reflectance using polarization sensitive optical coherence tomography (PS-OCT) in three non-human primates with induced glaucoma in one eye. We investigated the time variation of RNFL thickness, phase retardation, birefringence, and reflectance with elevated intraocular pressure (IOP). This chapter presents computational analysis of data from the non-human primate study that is described in Chapter 2. We submitted one journal paper and its revision to Investigated Ophthalmology & Visual Science[38].

4.1 MOTIVATION

Optical coherence tomography (OCT) is an imaging modality that provides high-resolution (2-15 μm) cross-sectional images of the retina at video rate and can quantify macroscopic changes in the optic nerve head (ONH) and RNFL. Inasmuch as previous studies have demonstrated a link between decreased RNFL thickness measured with OCT and glaucoma[17], OCT measurements of RNFL thickness have become a routine component of glaucoma screening, diagnosis, and monitoring protocols. Polarization sensitive OCT (PS-OCT) adds an additional contrast mechanism to standard OCT imaging and allows recording depth-resolved polarimetric measurements from the RNFL including phase retardation and birefringence. Previous studies have demonstrated a link between retinal birefringence and RNFL microtubule density [39],[40] providing a

motivation to investigate the predictive value of RNFL birefringence and phase retardation as candidate markers for early glaucoma diagnosis.

Increasing evidence has shown that mitochondrial dysfunction plays a key role in a number of neurodegenerative diseases including glaucoma [41,42,43]. In addition, Huang et al. observed cytoskeletal changes in response to elevated IOP that may precede RNFL thinning [44]. Because both mitochondria and the cytoskeleton contribute to light scattering, RNFL reflectance was measured in an attempt to monitor these features and related structural changes during glaucoma progression [45].

4.2 METHODS

4.2.1 RNFL Thickness Measurements

During post-processing of recorded PS-OCT data, the RNFL was automatically segmented in both continuous and clustered ring scan images as described previously [46]. A-scans in each cluster are averaged to reduce speckle noise, with the assumption that RNFL boundaries are changing slowly in each small cluster. A thresholding procedure was applied on these averaged A-scans to provide an initial guess of the vitreous-RNFL boundary location. The automatically detected RNFL boundaries were then manually inspected to ensure that the initial guess was correct. The region between the detected boundaries was segmented, taken as the RNFL, and used to calculate phase retardation (see Polarimetric Data Analaysis section below). For clustered ring scan data, RNFL boundaries were iteratively varied and the phase retardation re-calculated until uncertainty of the phase retardation was minimized. For clustered ring scan data, selected RNFL boundaries corresponded to minimum uncertainty of RNFL phase retardation.

4.2.2 Polarimetric Data Analysis

Inasmuch as interferometric imaging techniques suffer from speckle noise, A-scan averaging is necessary to obtain reliable estimates of RNFL phase retardation and birefringence. To determine estimates of RNFL phase retardation and birefringence, 200 A-scans in a clustered region are averaged to obtain an accurate estimate of phase retardation using a numerical algorithm described previously[19],[47] .The Stokes vectors for each of the three input polarization states are calculated from the two collected polarization channels. Computed Stokes vectors are segmented at the RNFL boundaries. In birefringent materials such as the RNFL the Stokes vectors of increasing depths trace arcs on the Poincare sphere where the subtended angle of the arcs is the double-pass phase retardation. A non-linear Levenberg-Marquardt algorithm estimates nine parameters by simultaneously fitting the three arcs on the Poincare sphere representing the polarization state of light reflected from the RNFL. The nine parameters returned by the Levenberg-Marquardt algorithm include the birefringence (1), optical axis orientation (2), and the three initial polarization states ($6 = 3 \times 2$). This calculation, performed for each cluster (see Figure 3) allows construction of birefringence and phase retardation maps around the ONH.

Each clustered map for each eye was registered rotationally and laterally using blood vessel maps acquired in continuous ring scan images immediately prior to recording clustered scans. Because the imaging areas on subsequent days did not precisely overlap, some clusters were excluded during the registration process. In addition, exclusion criteria were applied to screen clustered data for further processing. Exclusion criteria included: 1) RNFL thickness less than 15 μm; 2) relative uncertainty in RNFL birefringence ($\Delta n/n$) greater than 0.2; 3) absolute uncertainty of RNFL

birefringence greater than 30 deg/100 μm; or 4) RNFL not identifiable. Data sets with high birefringence uncertainty were typically clusters that contained large blood vessels.

4.2.3 RNFL Reflectance

To quantify RNFL reflectance, we define an RNFL reflectance index (*RI*) as the ratio of OCT intensities of the RNFL (I_{RNFL}) to that of a thin layer about the retinal pigment epithelium (*RPE*) and containing small volumes of the photoreceptor outer segment and superficial choroid (I_{RPE}). By referencing light reflected from the RNFL to a common structural layer in the retina (RPE), this *RI* definition normalizes variation due to system performance and corneal transmission. For example, because elevated IOP may be correlated with increased corneal cloudiness reducing light intensity incident on the retina our definition of *RI* mitigates the effect of corneal transmission variation. Variations in refractive power over the time course of the study (30 weeks) were minimized by optimizing the OCT image at the start of each imaging session by selecting a contact lens from a customized set to optimize focus of OCT light on the RNFL.

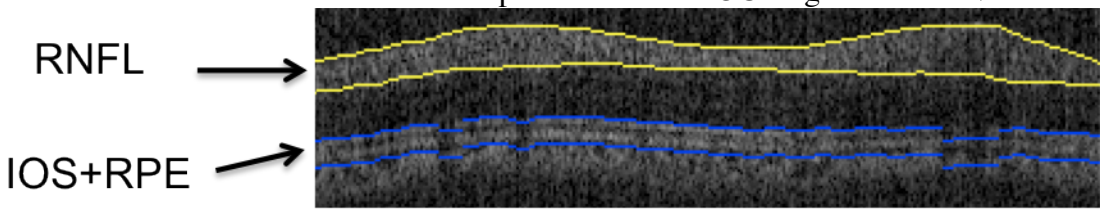

Figure 17. Segmented layers to determine RI , RNFL (yellow) and RPE (blue, including small volumes of inner and outer segment and superficial choroid) in a retinal B-scan image.

For each B-scan in continuous ring scan images, the RNFL was identified with an automatic boundary detection technique (similar to that applied to clustered ring scan data but lacking optimization using phase retardation) and the average RNFL brightness over the thickness (N_{RNFL}) was determined (I_{RNFL}). For I_{RPE}, an anterior boundary at the

IOS was identified automatically in the B-scan images. Similarly, a posterior boundary was taken to be 10 pixels (~75 μm) below the anterior boundary. This segmented RPE region is larger than necessary to fully capture the brightest reflecting region that is not in the RNFL in the retina. Although segmenting the anterior boundary at the Bruch's membrane is preferred, the limited axial resolution in this PS-OCT system and reliance on automated edge detection did not allow Bruch's membrane to be consistently segmented. Instead, a fixed thickness for the RPE region was taken. Average brightness value between these two boundaries (Figure 17, blue) gave I_{RPE}. We define RI for one A-scan in one B-scan image (either continuous or clustered ring scan data) corresponding to one image collection session as:

$$RI = \frac{\bar{I}_{RNFL}}{\bar{I}_{RPE}} \quad (8)$$

where for a continuous ring scan,

$$\bar{I}_{RNFL} = \frac{\sum_a I_{RNFL_a}}{N_{RNFL_a}} \quad (9)$$

which is the average OCT signal intensity in the RNFL for the ath A-scan.

For a clustered ring scan,

$$\bar{I}_{RNFL_c} = \frac{\sum_c \left(\sum_a I_{RNFL_a} \Big/ N_{RNFLa} \right)_c}{N_c} \quad (10)$$

which is the average OCT signal intensity in the RNFL for all A-scans of the cth cluster with N A-scans per cluster. For both continuous and clustered ring scan data,

$$\overline{I}_{RPE} = \frac{\sum_{b=1}^{N_b} \left(\sum_a I_{RPE_a} / N_{RPE} \right)_b}{N_b} \quad (11)$$

which is the average OCT signal intensity in a layer about the RPE and including small volumes of the inner and outer segment (IOS) and superficial choroid averaged over all B-scans in one image collection, where N_b is number of B-scans in each image collection, and N_{RPE} is number of pixels (10) in the layer about the RPE. For both continuous and clustered ring scans, we calculated RI for A-scans in one retinal scan and then constructed an *RI* map for that scan.

4.2.4 IOP Damage Integral

Because the procedure for inducing glaucoma provides a variable IOP increase, the number of days after glaucoma induction is not a representative measure of RNFL damage in response to elevated IOP and may result in artifacts between primates. For this reason, the integral over time of the IOP pressure difference between treated and control eyes (treated less control) was used to calculate the IOP damage integral at day *d*,

$$\text{IOP damage integral} = \int_0^d \left(IOP_{TR} - IOP_{CT} \right) dt \quad (12)$$

where *TR* is treated eye (OD) and *CT* is control eye (OS) and IOP is measured in mmHg and time (*t*) is in days. Variation of RNFL thickness, phase retardation, birefringence, and *RI* were analyzed versus both IOP damage integral and days (*d*) after glaucoma induction. Mean IOP was calculated by dividing the IOP damage integral by the number of days.

Damage to the optic nerve is a function of both the IOP damage integral and the mean absolute elevation of IOP[48].

4.2.5 Statistical Analysis

Linear and nonlinear mixed-effects models were applied to analyze RNFL thickness, phase retardation, birefringence, and RI data recorded in this study. Mixed-effect models allow for the variation between different subjects enrolled in the study. Application of linear and nonlinear mixed-effects models provides a number of advantages: 1) capture the similarities between as well as the variance among different primates enrolled in the study; and 2) effective for analysis of longitudinal, repeated-data measurements as recorded here. The R statistical programming language (v2.13.10 07/08/2011; http://www.R-project.org/, R Development Core Team, 2011, R Foundation for Statistical Computing, Vienna, Austria) and R studio (v0.94, 06/15/2011, RStudio, Inc.) was used to implement linear mixed-effects models. The non-linear mixed-effects model was implemented using MATLAB™ (The Mathworks, Natick, MA).

Continuous and clustered ring scan images of each primate retina recorded at different dates were registered against a baseline blood vessel raster scan image to ensure co-registration and alignment. We calculated averages for RNFL thickness, phase retardation, birefringence, and reflectance index (*RI*) for each primate eye corresponding to all rings, four inner rings, four outer rings, superior, inferior, nasal, and temporal quadrants. Each RNFL parameter for control and treated eyes was plotted against time (number of days, *d*) after administration of the first laser treatment for each primate. Linear mixed effects models were used to evaluate whether optical parameters changed over time:

$$P_{i,d} = (a_1 + b_i) + a_2 \cdot d + E_{i,d} \quad (13)$$

where $P_{i,d}$ is the value of parameter P (e.g., RNFL thickness, phase retardation, birefringence, or *RI*) of either the control or treated eye of the i^{th} primate on day d. The baseline intercept a_1 and the mean slope (a_2) for number of days (d) after laser treatment are fixed effects. The random effect is the variability from the baseline intercept for the i^{th} primate, b_i, which is normally distributed with zero-mean and standard deviation δ. $E_{i,d}$ is the random error component for the control eye or treated eye of the i^{th} primate on day d and is assumed to be normally distributed with a zero-mean and standard deviation δ_E. For both equation 6 and equation 7 below, a fixed slope is assumed. In a sample set with few subjects such as this a linear mixed effects model cannot converge to a solution with multiple random parameters. The random slope model is preferred because it assumes a similar effect for all the subjects with a random starting point for each subject. In order to show the variability of slopes among different primates individual fits for each primate are also included.

The difference in each RNFL parameter ($Pdif_{i,d}$) between the control and treated eyes on each day was plotted against the IOP damage integral. The data were fit with a linear mixed effects model(Equation below) to identify statistically significant trends:

$$Pdif_{i,d} = (\gamma_0 + \beta_i) + \gamma_1 \times IOP\,\mathrm{int}\,dif_{i,d} + \xi_{i,d} \quad (14)$$

Where $Pdif_{i,d}$ is the difference of the *P'th* RNFL parameter (RNFL thickness, phase retardation, birefringence, and *RI*) between the control and treated eye for the i^{th} primate on day d. $IOPintdiff_{i,d}$ is the IOP damage integral for the i^{th} primate on day d. The fixed

effects are the intercept γ_0 and the mean slope γ_1 for the IOP damage integral. The random effect is the variability from the baseline intercept for the i^{th} primate, β_i, which is normally distributed with mean zero and standard deviation δ_i. $\xi_{i,d}$ is the random error component for the i^{th} primate on day d and is assumed to be normally distributed with a mean of zero and standard deviation δ.

Based on qualitative observation of the data distribution and the fact that most damage processes can be fit with an exponential model [49], we also fit our data to a nonlinear mixed effects model such that

$$Pdif_{i,d} = (\alpha_0 + \eta_i) - \alpha_1 \times e^{-\frac{IOP\,\mathrm{int}\,dif_{i,d}}{\tau}} + \varepsilon_{i,d} \quad (15)$$

where $Pdif_{i,d}$ is the difference of the *P'th* RNFL parameter between control and treated eyes for the ith primate on day d. $IOPintdif_{i,d}$ is the IOP damage integral for the i^{th} primate on day d. Fixed effects include the intercept α_0, the coefficient α_1 for the exponential of IOP damage integral, and lifetime τ. The random effect is the variability from the baseline intercept for the i^{th} primate, η_i, which is normally distributed with zero-mean and standard deviation δ_i. $\varepsilon_{i,d}$ is the random error component for the i^{th} primate on day d and is assumed to be normally distributed with a mean of zero and standard deviation δ_e. We use the Akaike information criterion (AIC) and the Bayesian information criterion (BIC) to compare the goodness-of-fit of the non-linear and linear models.

4.3 RESULTS

4.3.1 Elevated IOP

IOP and PS-OCT data were recorded from six eyes in three primates in this experiment, three control and three treated eyes. A moderate IOP increase was observed

in each of the treated eyes (Figure 18) during the course of this study with an average IOP elevation of 13 mmHg. The protocol employed here gave a more moderate IOP elevation compared to a similar study [17] directed to detect a decreased RNFL thickness. The IOP damage integral for primate 3 was initially negative because of iritis resulting from the initial trabeculoplasty.

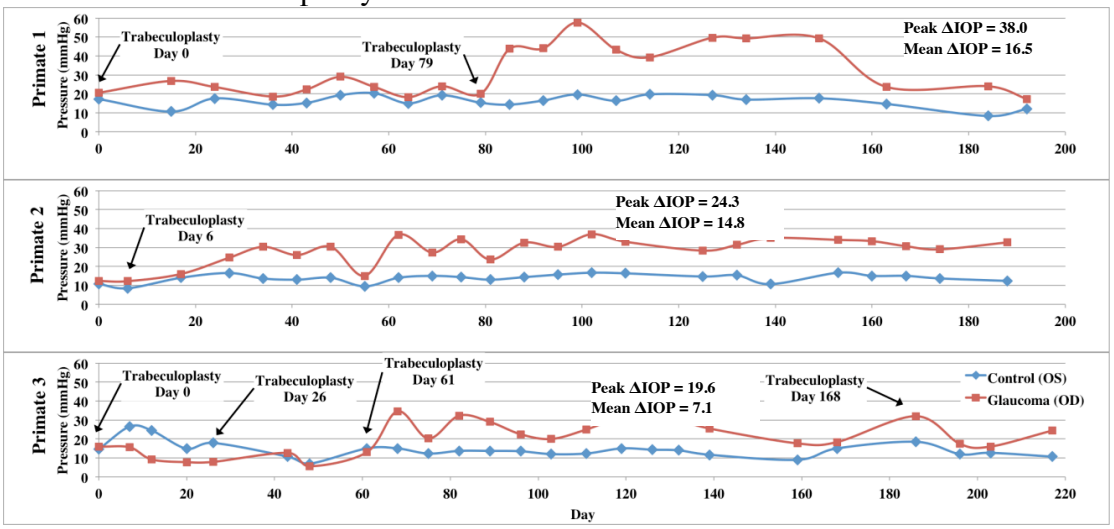

Figure 18. IOP vs. time in control (blue) and treated (red) eyes of each primate over course of the study. Peak ΔIOP values and mean ΔIOP values are included on the graphs for each primate.

4.3.2 Temporal Variation of RNFL Parameters

We measured four parameters from the clustered retinal scans: RNFL thickness, phase retardation, birefringence, and reflectance index (RI). Similar to the analysis performed on the clustered data, we measured two parameters, RNFL thickness and RI, from continuous ring scans. RNFL thickness and RI determined from clustered and continuous ring scans give similar but slightly different results. Retinal maps showing parameter values in both control and treated eyes are generated for beginning (day 27), middle (day 81), and end (day 174) time points (Figure 19 to Figure 24). In birefringence

maps, values are reported in units of phase retardation per unit depth (°/μm) and unitless birefringence.

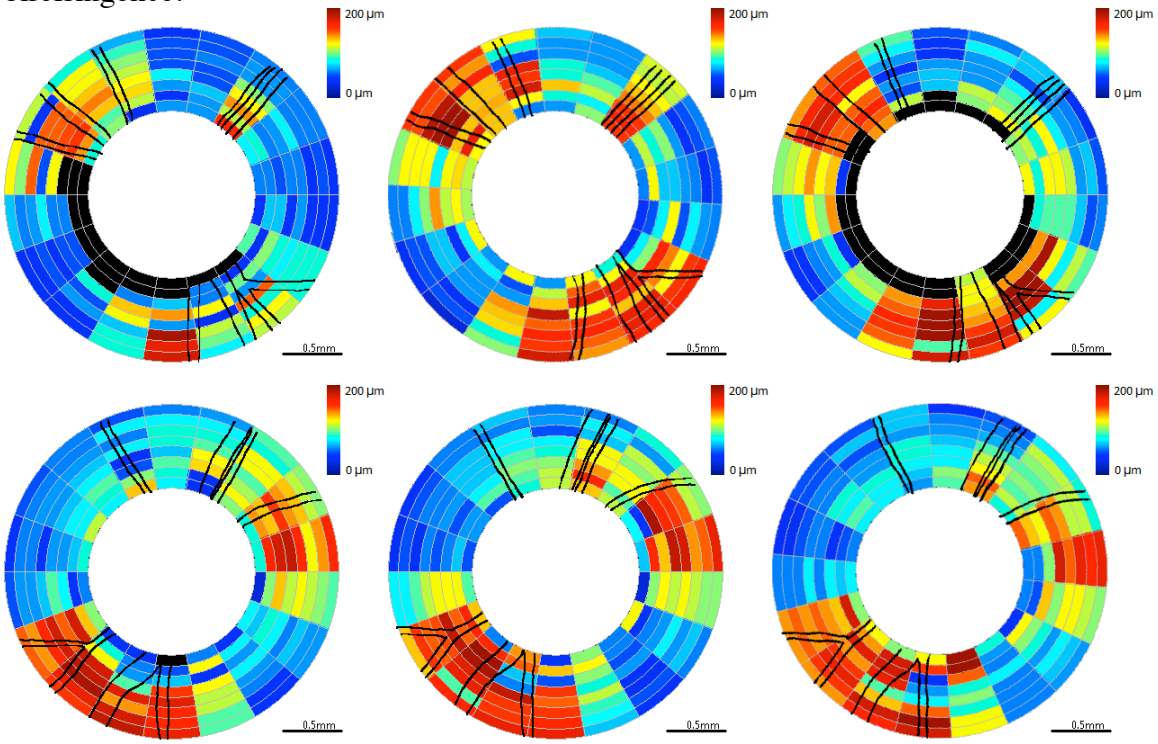

Figure 19. RNFL thickness maps for clustered retinal scans for primate 2. Top row is OD (treated eye) and bottom row is OS (control eye). Time points correspond to beginning (left column, day 27), middle (center column, day 81), and end (right column, day 174) of the study. Blood vessels indicated by black lines. Excluded clusters are marked black.

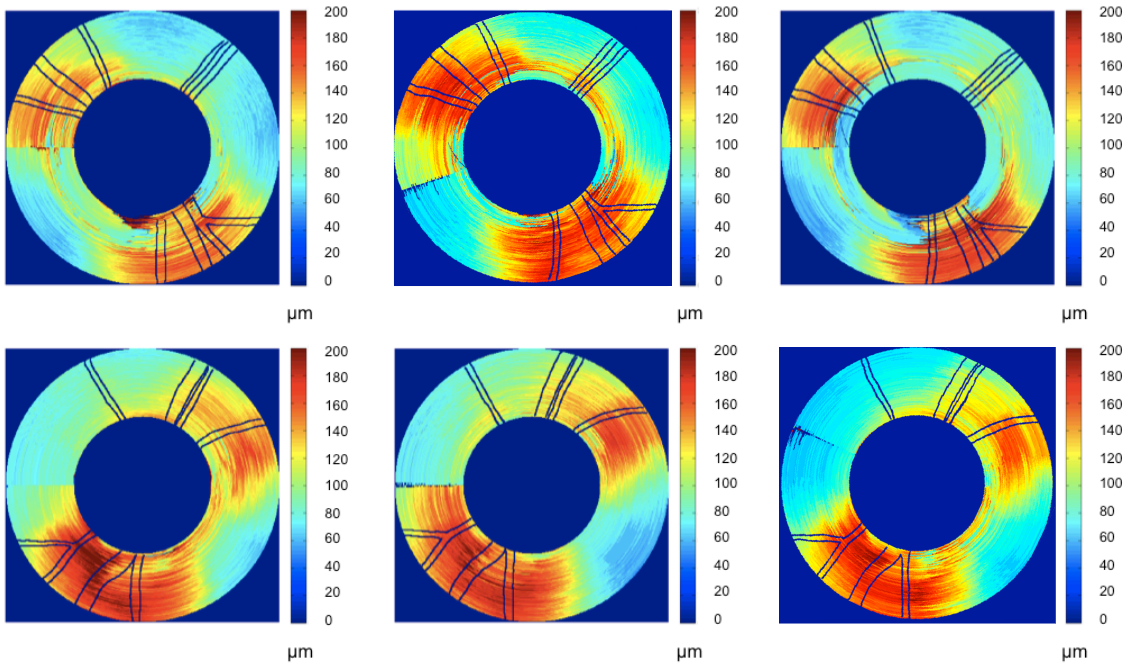

Figure 20. RNFL thickness maps for continuous ring scans for primate 2. Top row is OD (treated eye) and bottom row is OS (control eye). Time points correspond to beginning (left column, day 27), middle (center column, day 81), and end (right column, day 174) of the study. Blood vessels indicated by black lines.

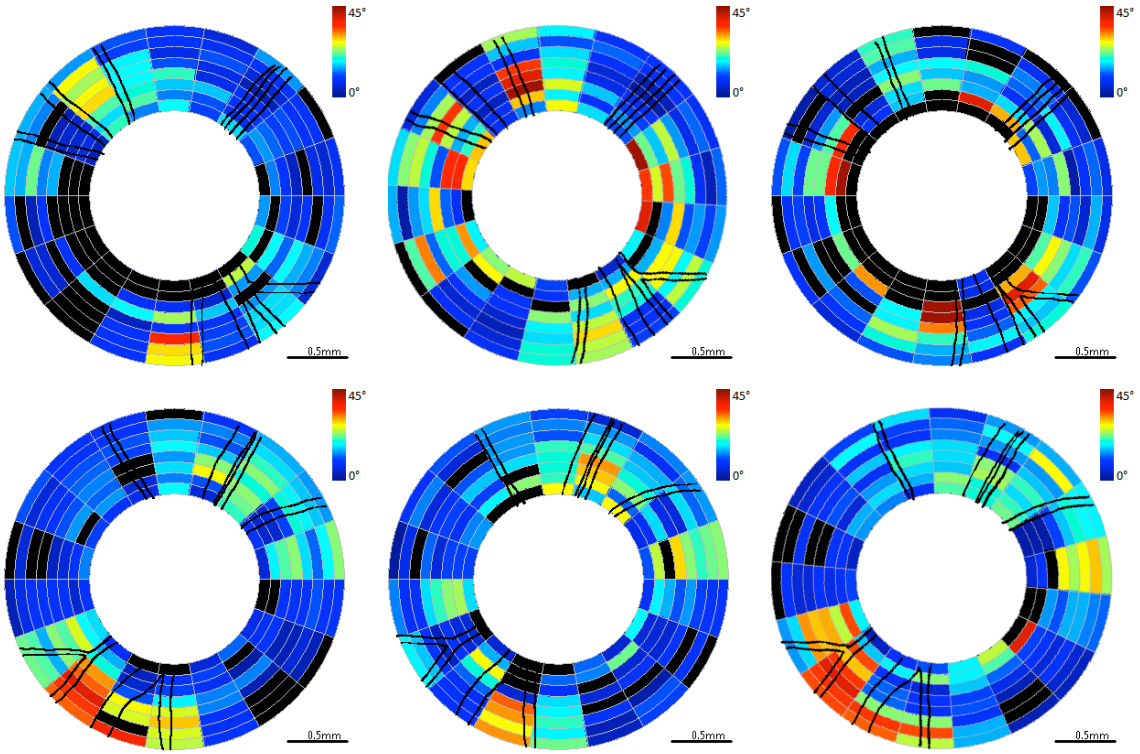

Figure 21. RNFL phase retardation maps for clustered retinal scans for primate 2. Top row is OD (treated eye) and bottom row is OS (control eye). Time points correspond to beginning (left column, day 27), middle (center column, day 81), and end (right column, day 174) of the study. Blood vessels indicated by black lines. Excluded clusters are marked black.

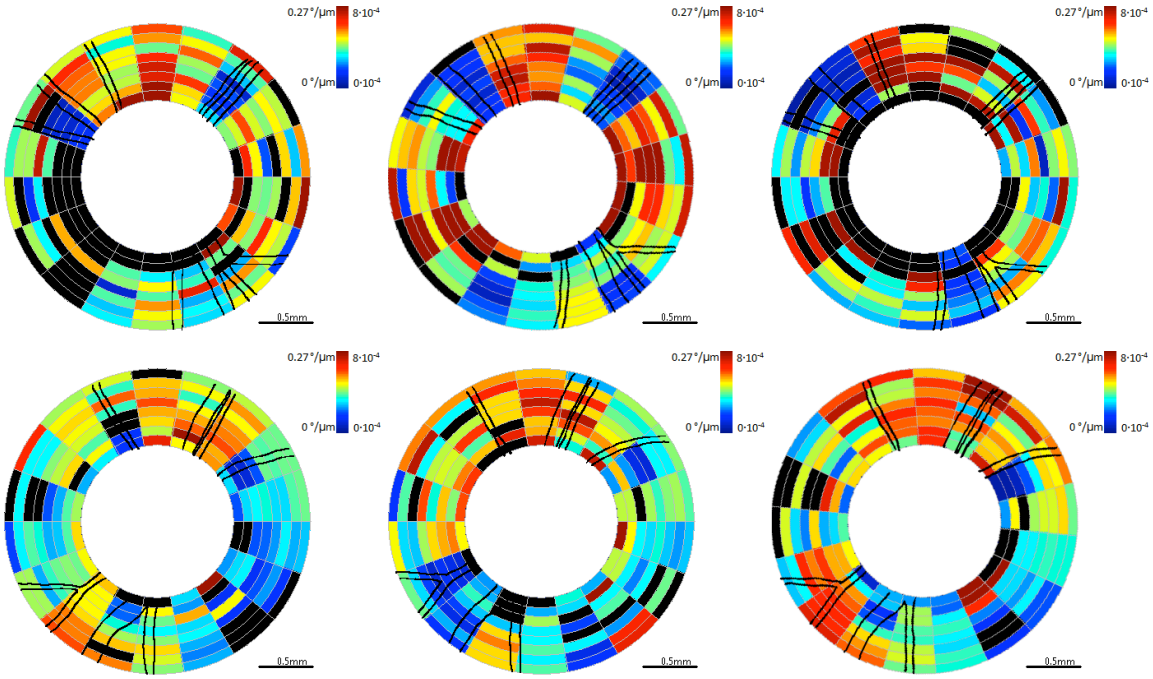

Figure 22. RNFL birefringence maps for clustered retinal scans for primate 2. Top row is OD (treated eye) and bottom row is OS (control eye). Time points correspond to beginning (left column, day 27), middle (center column, day 81), and end (right column, day 174) of the study. The color scale is notated with units of both unitless birefringence and phase retardation unit depth (°/µm). Blood vessels are indicated by black lines. Excluded clusters are marked black.

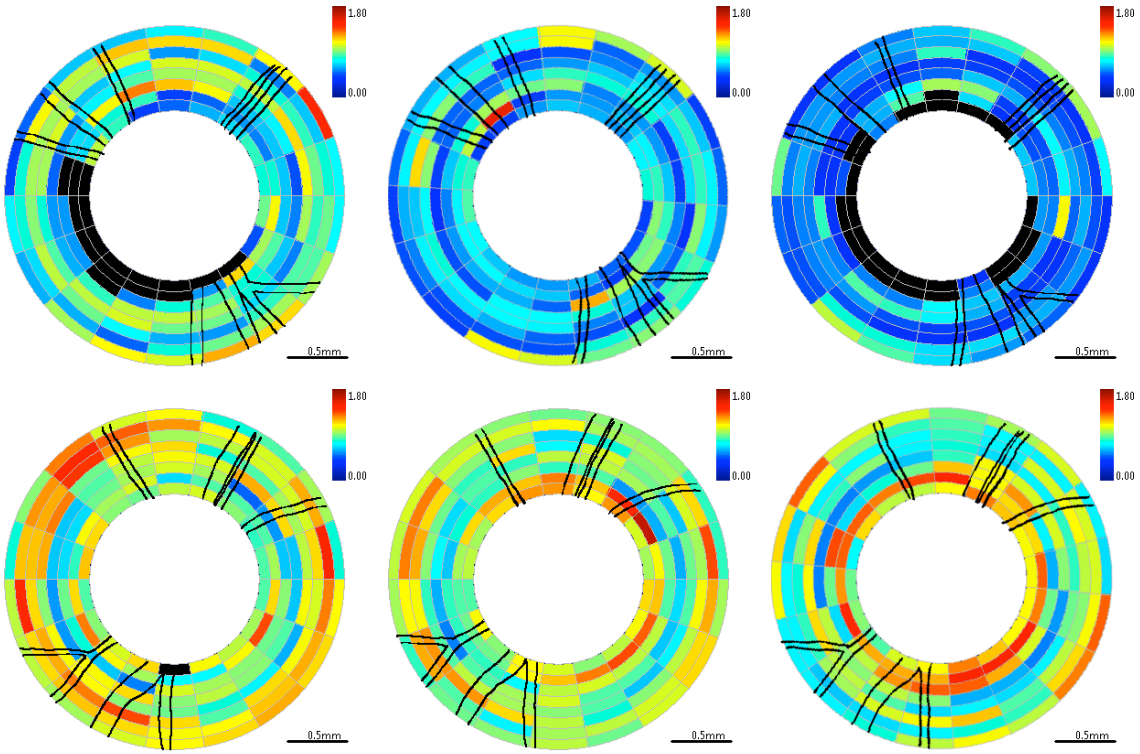

Figure 23. RNFL reflectance index (*RI*) maps for clustered retinal scans for primate 2. Top row is OD (treated eye) and bottom row is OS (control eye). Time points correspond to beginning (left column, day 27), middle (center column, day 81), and end (right column, day 174) of the study. Blood vessels indicated by black lines. Excluded clusters are marked black.

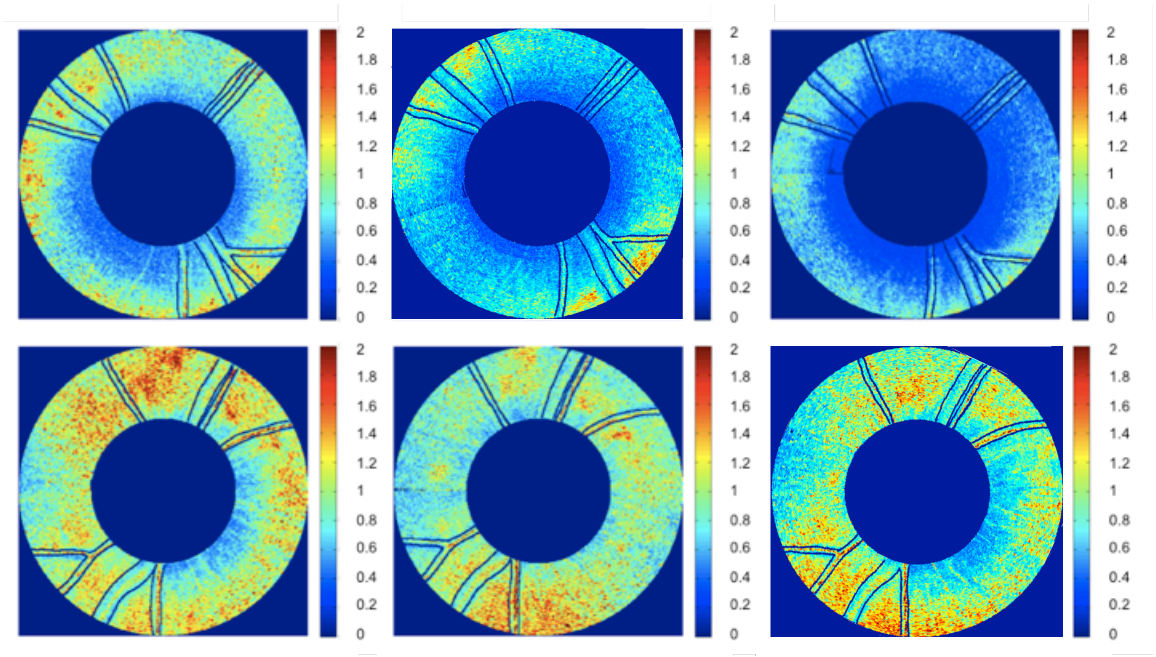

Figure 24. RNFL reflectance index (*RI*) maps for continuous ring scans for primate 2. Top is OD (treated eye) and bottom is OS (control eye). Time points correspond to beginning (left, day 27), middle (center, day 81), and end (right, day 174) of the study. Blood vessels indicated by black lines.

Each parameter (RNFL thickness, phase retardation, birefringence, and reflectance index (RI)) averaged over the entire ring scan is plotted against number of days from the first laser trabeculoplasty (Figure 25 to Figure 28). A linear mixed effects model (Eq. 13) is applied to fit each RNFL parameter as a function of time. In both clustered and continuous ring scan data, both the control and treated eyes showed a significant decrease in *RI*. When averaged over all rings, no significant changes in RNFL thickness, birefringence, or phase retardation was observed (Figure 25 to Figure 28).

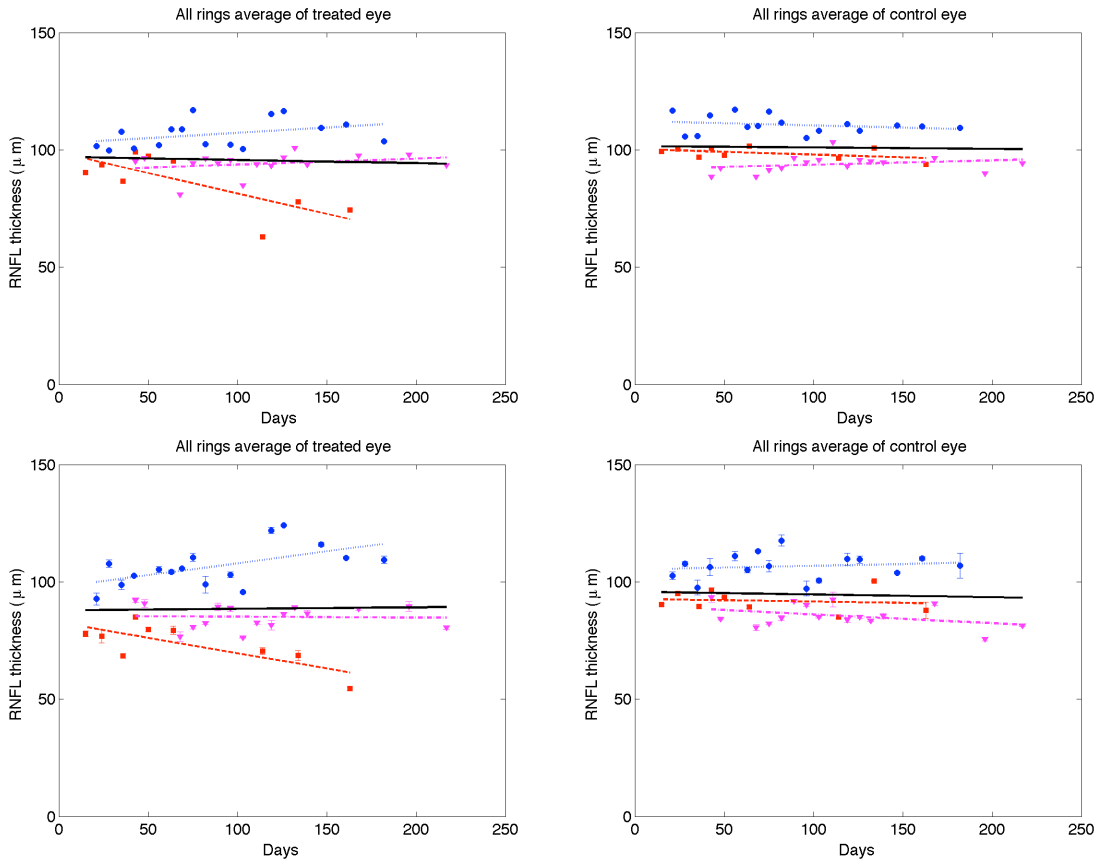

Figure 25. Time variation of averaged (all rings) RNFL thickness of treated (left column) and control (right column) eyes for continuous (top row) and clustered (bottom row) ring scans (squares primate 1; circles primate 2, and triangles primate 3). Linear mixed effects model fits for individual primates (colored lines) and combined (all primates, black). Statistics for the combined data are shown in the supplemental material in Table 2 and the individual fits are included in Table 3 to Table 5.

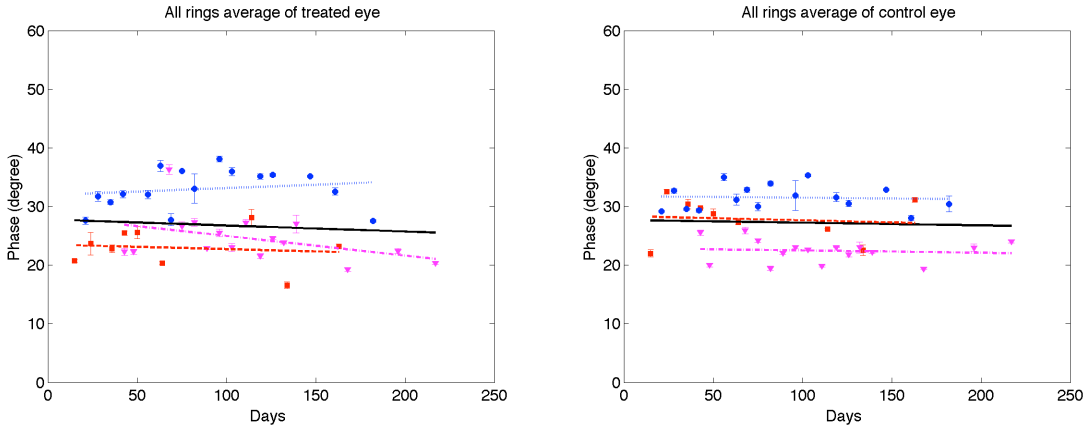

Figure 26. Time variation of averaged (all rings) RNFL phase retardation of treated (left) and control (right) eyes for clustered retinal scans (squares primate 1; circles primate 2, and triangles primate 3). Linear mixed effects model fits for individual primates (colored lines) and combined (all primates, black). Statistics for the combined data are shown in the supplemental material in Table 2 and the individual fits are included in Table 3 to Table 5.

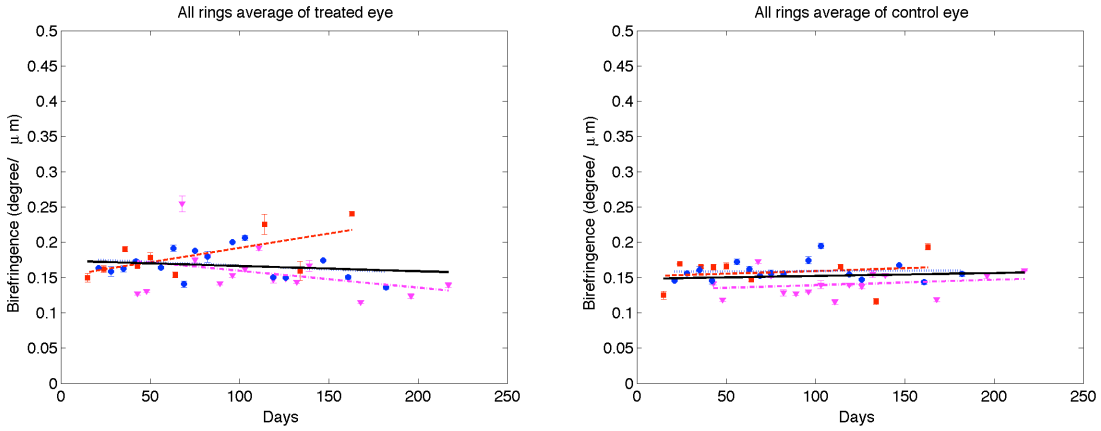

Figure 27. Time variation of averaged (all rings) RNFL birefringence of treated (left) and control (right) eyes for clustered retinal scans (squares primate 1; circles primate 2, and triangles primate 3). Linear mixed effects model fits for individual primates (colored lines) and combined (all primates, black). Statistics for the combined data are shown in the supplemental material in Table 2 and the individual fits are included in Table 3 to Table 5.

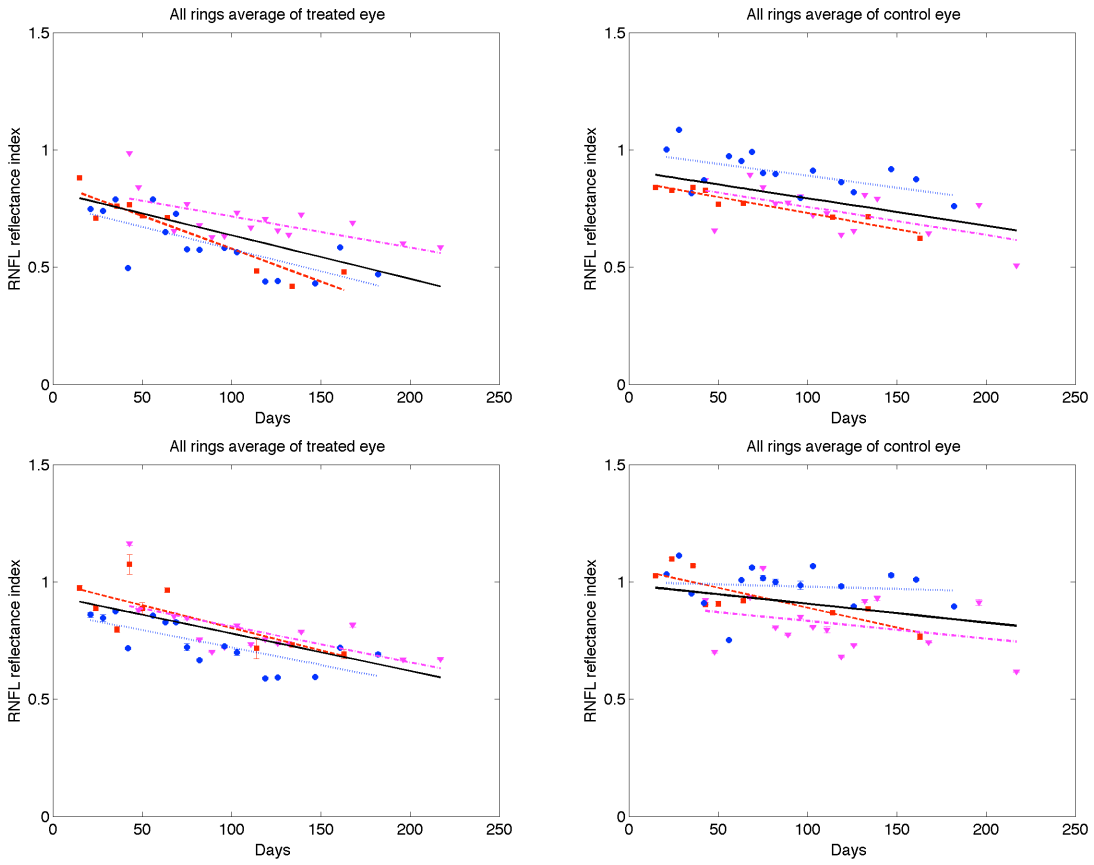

Figure 28. Time variation of averaged (all rings) RNFL reflectance index (*RI*) of treated (left column) and control (right column) eyes for continuous (top row) and clustered (bottom row) ring scans (squares primate 1; circles primate 2, and triangles primate 3). Linear mixed effects model fits for individual primates (colored lines) and combined (all primates, black). The linear mixed model suggests *RI* decreased significantly over time for both treated ($p<0.0001$) and control eyes ($p<0.05$). Statistics for the combined data are shown in the supplemental material in Table 2 and the individual fits are included in Table 3 to Table 5.

A linear mixed effects model was also used to analyze RNFL parameters in each segmented region (results available in supplemental material, Table 2 to Table 6). The linear mixed-effects model analysis of all three primates combined versus number of days shows a significant *RI* decrease in control and treated eyes for all averaged regions but no significant changes in RNFL thickness, birefringence or phase retardation. The linear

mixed-effects model analysis of individual primates versus number of days shows significant decrease in *RI* for the majority of averaged regions in the treated eye, RNFL thickness decreases in some regions, and isolated regions show decreases in phase retardation and birefringence. In the individual results for primate 1, there was also several groupings that showed a small but significant increase in the birefringence for the treated eye over the course of the study. In these regions of increased birefringence for this isolated primate there is also a significant increase in the birefringence uncertainty through the course of the study.

4.3.3 RNFL parameters versus IOP damage integral

To evaluate change of RNFL parameters with respect to IOP exposure, we fit the difference between control and the treated eyes of RNFL parameters as a function of IOP damage integral using a linear mixed effects model. Inasmuch as significant trends might emerge in isolated regions of the eyes, retinal maps were segmented and RNFL parameters in each segment was analyzed separately in addition to parameter averages over the entire retina. RNFL parameters were computed and averaged in segmented regions including the four inner rings, four outer rings, superior, inferior, nasal, and temporal quadrants and plotted both over time and IOP damage integral. Fits were performed in each segmented region for all three primates combined (Table 1) as well as individuals (see supplemental material, Table 6).

Differences in RNFL thickness, phase retardation, birefringence, and reflectance index (RI) are plotted (Figure 29 to Figure 33) for all usable clusters with all primates combined. No significant trend is observed ($p>0.05$) in the difference of RNFL thickness, phase retardation and birefringence between control and treated eyes vs. IOP damage integral. For both clustered and continuous ring scan data, difference between RNFL

reflectance index (RI) of control and treated eyes increases significantly when IOP damage integral increases ($p<0.05$ for both).

Using a linear mixed effects model, RNFL parameters (thickness, phase retardation, birefringence, and reflectance index) averaged in various segmented regions (all rings, inner rings, outer rings, superior, inferior, nasal, and temporal quadrants) were evaluated versus the IOP damage integral (Figure 29 to Figure 33). For all RNFL thickness measurements in each segmented region, only the nasal quadrant showed a significant change. The inferior quadrant showed a significant change for both RNFL phase retardation and birefringence. In addition, RNFL phase retardation had a significant change in the superior quadrant and the birefringence had a significant change in the nasal region.

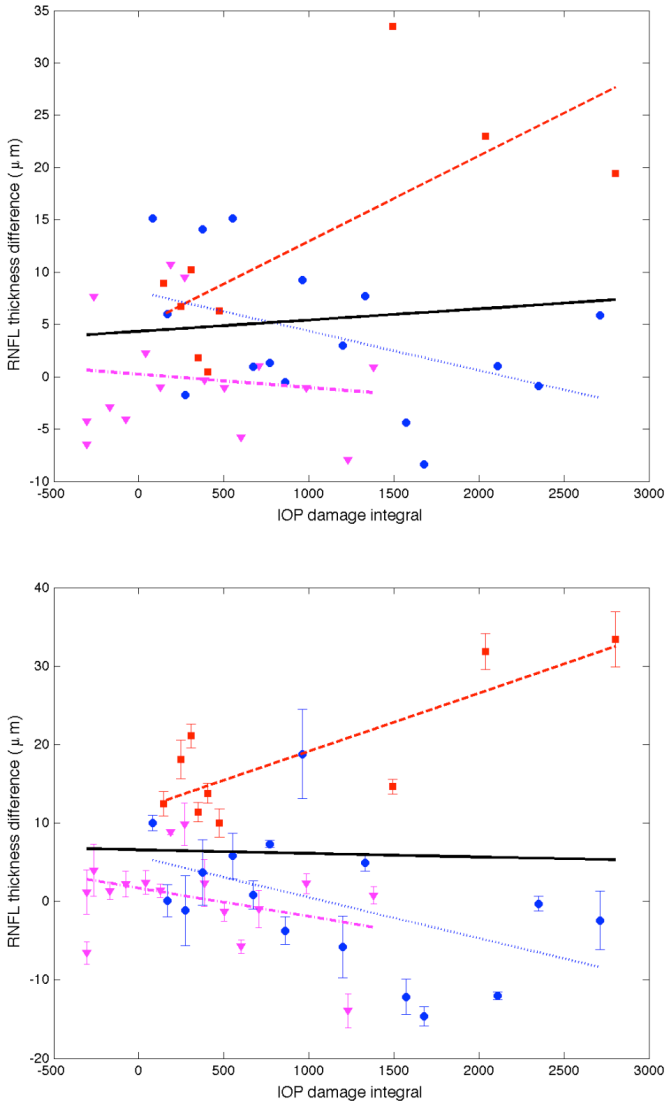

Figure 29. Average (all rings) of RNFL thickness difference (control less treated) for continuous (top) and clustered (bottom) retinal scans vs. IOP damage integral (squares primate 1; circles primate 2; and triangles are primate 3). Linear mixed model fits for individual primates (colored lines) and combined (all primates, black). Statistics for the combined data are shown in Table 1 and the individual fits are included in the supplemental material in Table 6.

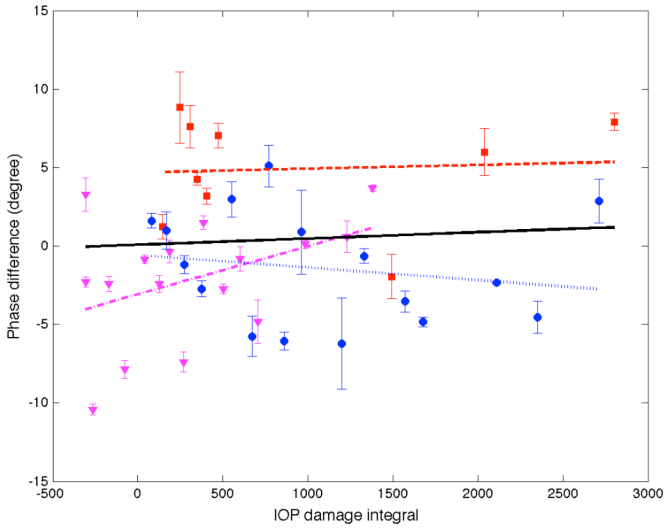

Figure 30. Average (all rings) of phase retardation difference (control less treated) for clustered retinal scans vs. IOP damage integral (squares primate 1; circles primate 2; and triangles are primate 3). Linear mixed model fits for individual primates (colored lines) and combined (all primates, black). Statistics for the combined data are shown in Table 1 and the individual fits are included in the supplemental material in Table 6.

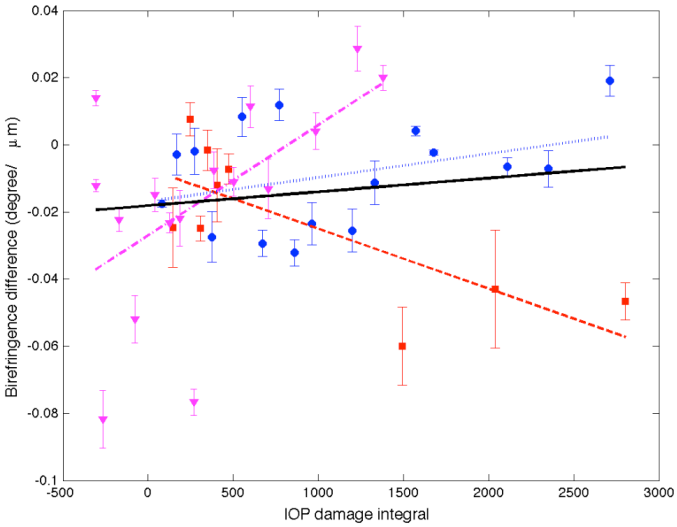

Figure 31. Average (all rings) of birefringence difference (control less treated) for clustered retinal scans vs. IOP damage integral (squares primate 1; circles primate 2; and triangles are primate 3). Linear mixed model fits for individual primates (colored lines) and combined (all primates, black). Statistics for the combined data are shown in Table 1 and the individual fits are included in the supplemental material in Table 6.

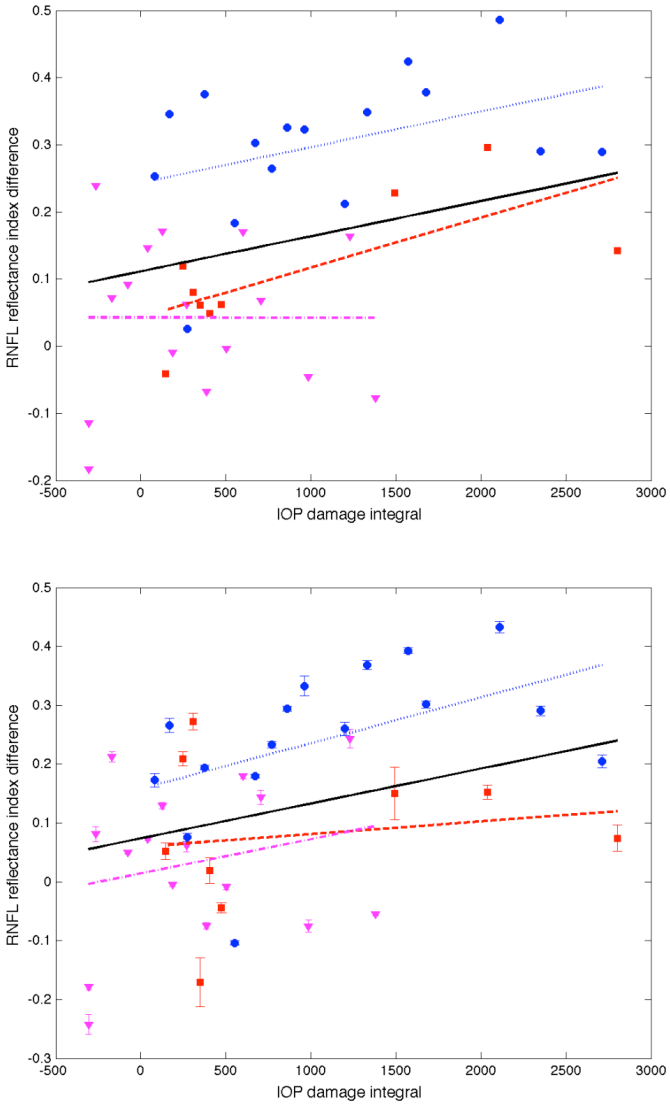

Figure 32. Average (all rings) of RNFL reflectance index (RI) difference (control less treated) for continuous (top) and clustered (bottom) retinal scans vs. IOP damage integral (squares primate 1; circles primate 2; and triangles are primate 3). Linear mixed model fits for individual primates (colored lines) and combined (all primates, black). Statistics for the combined data are shown in Table 1 and the individual fits are included in the supplemental material in Table S5.

Table 1. RNFL parameter differences (control less treated) in segmented regions versus IOP damage integral for all primates analyzed with a linear mixed effects model. P-values with values <0.05 have been marked in red to easily identify the regions of statistical significance.

RNFL Parameter	Region	Slope	p(slope)
Clustered Thickness (µm)	All rings	-4.52×10^{-4}	0.789
	Inner ring	-2.47×10^{-3}	0.274
	Outer ring	2.16×10^{-4}	0.891
	Superior	4.81×10^{-3}	0.129
	Inferior	2.75×10^{-3}	0.462
	Nasal	-6.83×10^{-3}	0.000
	Temporal	4.39×10^{-3}	0.186
Continuous Thickness (µm)	All rings	1.07×10^{-3}	0.511
	Inner ring	9.30×10^{-4}	0.647
	Outer ring	1.27×10^{-3}	0.409
	Superior	2.36×10^{-3}	0.140
	Inferior	3.22×10^{-3}	0.342
	Nasal	1.88×10^{-3}	0.278
	Temporal	-3.06×10^{-3}	0.058
Phase (°)	All rings	1.76×10^{-4}	0.698
	Inner ring	2.34×10^{-4}	0.729
	Outer ring	-1.21×10^{-4}	0.772
	Superior	1.38×10^{-3}	0.046
	Inferior	-1.70×10^{-3}	0.021
	Nasal	3.83×10^{-4}	0.502
	Temporal	3.29×10^{-4}	0.701
Birefringence (°/µm)	All rings	4.12×10^{-9}	0.820
	Inner ring	1.77×10^{-8}	0.440

	Outer ring	-1.23×10^{-8}	0.597
	Superior	2.02×10^{-8}	0.279
	Inferior	-7.28×10^{-8}	0.002
	Nasal	6.27×10^{-8}	0.029
	Temporal	-1.05×10^{-7}	0.195
Clustered Reflectance Index (RI)	All rings	5.93×10^{-5}	0.038
	Inner ring	6.30×10^{-5}	0.053
	Outer ring	5.98×10^{-5}	0.043
	Superior	4.99×10^{-5}	0.091
	Inferior	5.55×10^{-5}	0.058
	Nasal	7.22×10^{-5}	0.016
	Temporal	6.77×10^{-5}	0.023
Continuous Reflectance Index (RI)	All rings	5.23×10^{-5}	0.028
	Inner ring	4.89×10^{-5}	0.054
	Outer ring	5.58×10^{-5}	0.018
	Superior	5.39×10^{-5}	0.061
	Inferior	8.89×10^{-5}	0.014
	Nasal	6.36×10^{-5}	0.021
	Temporal	8.42×10^{-6}	0.783

We analyze RI versus IOP damage integral using a non-linear model (Eq. 15)[50]. We use the Akaike information criterion (AIC) and Bayesian information criterion (BIC) to compare the goodness-of-fit of the non-linear and linear models. Because AIC and BIC values derived from the nonlinear model (clustered: AIC=-39.4, BIC=-30.8; continuous:

AIC=-52.0,BIC=-43.4) are smaller than those of the linear model (clustered: AIC=-16.6, BIC=-9.9; continuous: AIC=-37.8, BIC=-31.2), we conclude that the nonlinear model provides a better fit to *RI* data compared to the linear model. In both linear and non-linear models, the continuous scan provides a better fit than the clustered scan.

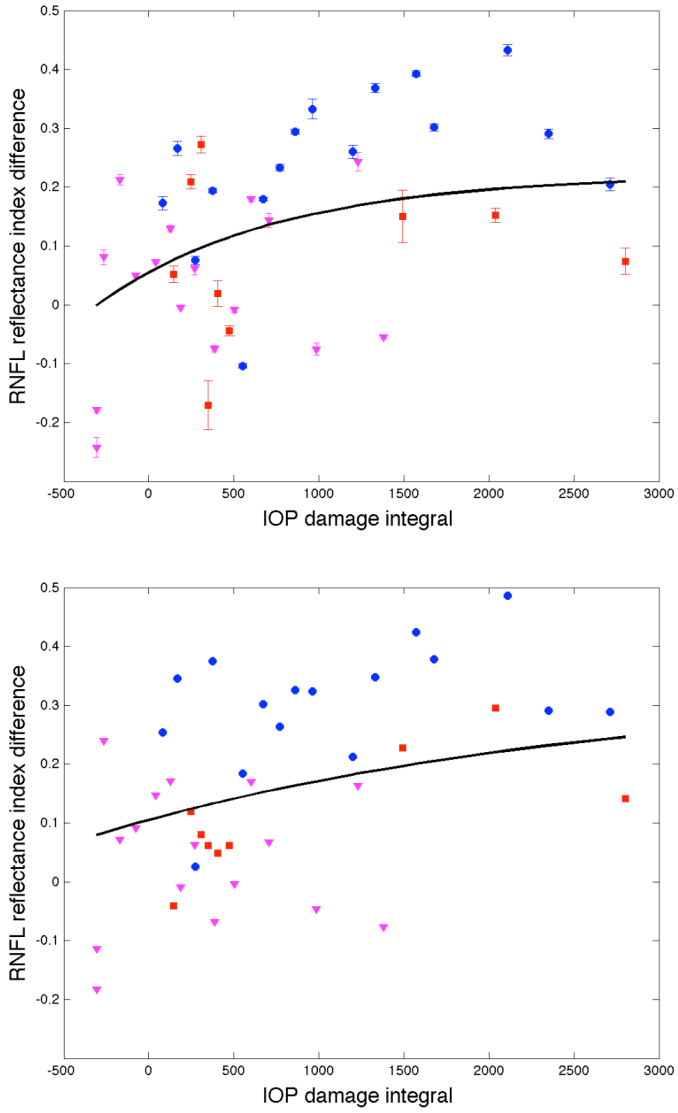

Figure 33. Average (all rings) of RNFL reflectance index (*RI*) difference (control less treated) for clustered (top) and continuous (bottom) retinal scans vs. IOP damage integral (squares primate 1; circles primate 2; and triangles are primate 3). Nonlinear mixed effects model fits (black curves) for clustered (τ =1060.4, AIC=-39.4, BIC=-30.8) and continuous (τ =2848.3, AIC=-52.0, BIC=-43.4) data for all primates.

4.4 DISCUSSION

At the outset, it should be noted that these results are derived from a small sample of only three primates. This is a pilot study and the results while showing statistical significance should be treated as preliminary. The parameter in treated eyes with elevated IOP showing the most significant change was RNFL reflectance index (*RI*). Statistically significant decreases in *RI* were observed in some quadrants in treated eyes. *RI* derived from clustered retinal scans showed statistically significant decreases with increased IOP damage integral in all-rings, outer-rings, nasal, and temporal quadrants. *RI* derived from continuous retinal scans showed statistically significant decreases with IOP damage integral in all-rings, outer-rings, inferior, and nasal quadrants. Using the linear mixed effects model, significant changes were observed in *RI* vs. number of days for both the control and treated eyes. The rate of decrease of *RI* for the treated eye (-1.60×10^{-3} days^{-1}) was five-times greater than that observed in control eyes (-0.080×10^{-3} days^{-1}). Prolonged and frequent anesthesia of the three primates enrolled in these studies may have contributed to decreased *RI* in the control eyes. Interestingly, neural mitochondrial changes have been observed in rodents subjected to prolonged anesthesia exposure [51]. As discussed below, mitochondrial changes can impact optical scattering properties of the host cell. Consequently, mitochondrial changes due to prolonged anesthesia exposure may have contributed to *RI* decrease observed in control and treated eyes. Phase retardation and birefringence changes were detected in the course of this study only in the inferior quadrant and may be considered as candidate markers for early glaucoma diagnosis in subsequent investigations.

4.4.1 RNFL Thickness Changes

Schuman et al. have observed RNFL thinning as a result of elevated IOP with a similar level of IOP integral. In the current study, statistically significant RNFL thinning was observed only in the nasal region (the thinnest RNFL region) using the clustered thickness data. Considering the lower values of average IOP utilized in this study (13 mm Hg) compared to those employed by Schuman et al. (~25 mmHg), absence of significant RNFL thinning may not be unexpected even considering a similar IOP integral value. The IOP integral is a linear damage model with poorly understood limitations. Both the IOP integral and the ΔIOP are important parameters in predicting glaucoma damage. Chauhan et al. investigated the effect of elevated IOP in rodents and found a strong correlation of functional and structural changes to peak IOP, suggesting a damage threshold [48]. Although Schuman doesn't report the peak IOP values for individual primates enrolled in his study, values are assumed to be much higher considering the study had a shorter duration to reach similar IOP integral values. In this sense, absence of significant RNFL thinning in all regions can be viewed as complementary, not contradictory to previous studies.

4.4.2 Candidate Cellular Mechanisms

This is not the first study to report reflectance changes in the retina; however, it is the first reported definition of reflectance change observed with OCT and the first report that RNFL reflectance decreases when glaucoma is induced in primates[45],[52]. Although additional investigation is necessary to test candidate mechanisms for RNFL reflectance decrease observed here, changes in the mitochondrial networks and axonal cytoskeleton changes are hypothetical mechanisms. Previous studies have demonstrated that changes in mitochondrial membrane permeability in response to elevated IOP precede retinal ganglion cell loss in glaucomatous eyes [43,53].

Mitochondrial dysfunction is recognized as an important component in the etiology of many neurodegenerative pathologies including amyotrophic lateral sclerosis, Alzheimer's, and Parkinson's disease. Mitochondria are recognized as dynamic organelles that constantly undergo fusion and fission processes that are required to maintain normal function of the host cell. Fusion of mitochondria to form interconnected intracellular networks is believed to be a necessary component to maintain a mitochondrial population with a full complement of gene products that can mitigate age-related degeneration. In fact, autosomal dominant optic atrophy, the leading cause of childhood blindness, is caused by a mutation in the mitochondrial fusion gene OPA1 [54]. Inasmuch as mitochondrial changes are an important component of neurodegenerative diseases, their potential contribution to RNFL reflectance changes is of interest.

Recently, Ju et al. demonstrated that mitochondria fission in differentiated retinal ganglion cell cultures is induced in response to elevated hydrostatic pressures [55]. A number of recent studies have observed optical scattering changes in cells undergoing apoptosis that originate at least in part to the mitochondria. Pasternack et al. used a Fourier microscopy approach to demonstrate that early cell apoptosis is accompanied by mitochondrial fission and fragmentation that results in more isotropic or large-angle light scattering [56]. Chalut et al. utilized angle-resolved optical coherence tomography (OCT) to document similar scattering changes that the authors suggested may involve mitochondrial fission [57]. A number of investigators have recently applied OCT to document light scattering changes in cells undergoing apoptosis or necrosis[58],[59]. Although the decrease in RI in glaucomatous primate eyes reported here is consistent with reduced collected backscatter due to intensified mitochondrial fission resulting in increased large angle scattering, other mechanisms such as changes in the axonal

membrane or microtubules may contribute to the observed decrease in RNFL reflectance. Additional studies are required to isolate and better characterize the various candidate cellular processes that may contribute to decreased RNFL reflectance observed in studies reported here. In chapter 5, we will validate some of our findings in human clinical glaucoma study.

4.5 SUPPLEMENTAL INFORMATION

Table 2. RNFL parameters in segmented regions versus number of days for all primates analyzed with a linear mixed model. P-values with values <0.05 have been marked in red to easily identify the regions of statistical significance.

		Mix of all 3 primates			
		Control		Treated	
RNFL Parameter	Feature	Slope	p (slope)	Slope	p (slope)
Clustered Thickness (µm)	All rings	-1.15×10^{-2}	0.495	6.45×10^{-3}	0.797
	Inner rings	-1.11×10^{-2}	0.637	4.03×10^{-2}	0.244
	Outer rings	-2.30×10^{-2}	0.228	-1.59×10^{-2}	0.49
	Superior	3.22×10^{-2}	0.418	2.93×10^{-3}	0.938
	Inferior	-2.40×10^{-2}	0.517	-5.21×10^{-2}	0.277
	Nasal	-5.47×10^{-2}	0.006	4.37×10^{-2}	0.065
	Temporal	3.13×10^{-2}	0.209	-2.19×10^{-3}	0.954
Continuous Thickness (µm)	All rings	-5.66×10^{-3}	0.627	-1.34×10^{-2}	0.583
	Inner rings	-6.50×10^{-3}	0.651	-1.05×10^{-2}	0.728
	Outer rings	-6.76×10^{-3}	0.554	-1.50×10^{-2}	0.51
	Superior	-9.73×10^{-4}	0.956	-1.65×10^{-2}	0.44
	Inferior	-1.73×10^{-2}	0.476	-4.54×10^{-2}	0.313
	Nasal	1.25×10^{-2}	0.359	-1.02×10^{-2}	0.693
	Temporal	-1.60×10^{-2}	0.348	2.96×10^{-2}	0.155
Phase Retardation (°)	All rings	-4.52×10^{-3}	0.473	-1.03×10^{-2}	0.372
	Inner rings	-4.75×10^{-3}	0.538	-1.27×10^{-2}	0.557
	Outer rings	-6.72×10^{-3}	0.376	-4.80×10^{-3}	0.517
	Superior	9.85×10^{-3}	0.385	-2.60×10^{-2}	0.173
	Inferior	-3.69×10^{-2}	0.034	1.58×10^{-2}	0.366
	Nasal	-2.24×10^{-3}	0.875	-1.26×10^{-2}	0.248
	Temporal	2.35×10^{-2}	0.414	-4.92×10^{-3}	0.949
Birefringence (°/µm)	All rings	4.15×10^{-5}	0.833	-7.43×10^{-5}	0.648
	Inner rings	3.98×10^{-5}	0.54	-1.39×10^{-4}	0.366
	Outer rings	5.29×10^{-5}	0.971	1.93×10^{-5}	0.614
	Superior	4.04×10^{-6}	0.871	-1.13×10^{-4}	0.337
	Inferior	-7.72×10^{-5}	0.203	2.29×10^{-4}	0.054
	Nasal	1.62×10^{-4}	0.13	-1.97×10^{-4}	0.245
	Temporal	1.13×10^{-4}	0.898	2.67×10^{-4}	0.265
Clustered Reflectance Index (RI)	All rings	-8.03×10^{-4}	0.015	-1.60×10^{-3}	0.000
	Inner rings	-4.40×10^{-4}	0.247	-1.28×10^{-3}	0.000
	Outer rings	-1.14×10^{-3}	0.002	-1.88×10^{-3}	0.000
	Superior	-8.66×10^{-4}	0.013	-1.51×10^{-3}	0.000
	Inferior	-6.74×10^{-4}	0.053	-1.42×10^{-3}	0.000
	Nasal	-8.08×10^{-4}	0.019	-1.76×10^{-3}	0.000
	Temporal	-8.64×10^{-4}	0.009	-1.76×10^{-3}	0.000
Continuous Reflectance Index (RI)	All rings	-1.17×10^{-3}	0.000	-1.86×10^{-3}	0.000
	Inner rings	-1.21×10^{-3}	0.000	-1.88×10^{-3}	0.000
	Outer rings	-1.15×10^{-3}	0.000	-1.86×10^{-3}	0.000
	Superior	-1.47×10^{-3}	0.000	-2.21×10^{-3}	0.000
	Inferior	-8.43×10^{-4}	0.045	-1.93×10^{-3}	0.000
	Nasal	-1.09×10^{-3}	0.001	-1.93×10^{-3}	0.000
	Temporal	-1.30×10^{-3}	0.000	-1.35×10^{-3}	0.000

Table 3. RNFL parameters in segmented regions versus number of days for primate 1 analyzed with a linear mixed model. P-values with values <0.05 have been marked in red to easily identify the regions of statistical significance.

RNFL Parameter	Feature	Primate 1			
		Control		Treated	
		Slope	p (slope)	Slope	p (slope)
Clustered Thickness (µm)	All rings	-1.04×10^{-2}	0.768	-1.31×10^{-1}	0.768
	Inner rings	-9.97×10^{-3}	0.854	-1.08×10^{-1}	0.854
	Outer rings	-2.12×10^{-2}	0.436	-1.46×10^{-1}	0.436
	Superior	3.08×10^{-2}	0.700	-1.02×10^{-1}	0.700
	Inferior	-6.18×10^{-3}	0.946	-3.91×10^{-1}	0.946
	Nasal	-1.36×10^{-1}	0.016	3.42×10^{-1}	0.016
	Temporal	1.61×10^{-1}	0.002	-2.22×10^{-1}	0.002
Continuous Thickness (µm)	All rings	-2.34×10^{-2}	0.192	-1.75×10^{-1}	0.019
	Inner rings	-1.99×10^{-2}	0.466	-1.89×10^{-1}	0.014
	Outer rings	-2.73×10^{-2}	0.119	-1.64×10^{-1}	0.025
	Superior	-3.47×10^{-2}	0.506	-7.62×10^{-2}	0.172
	Inferior	-1.19×10^{-2}	0.774	-4.05×10^{-1}	0.004
	Nasal	2.23×10^{-2}	0.134	-1.42×10^{-1}	0.005
	Temporal	-5.33×10^{-2}	0.353	9.26×10^{-3}	0.858
Phase Retardation (°)	All rings	-5.39×10^{-3}	0.716	-7.36×10^{-5}	0.996
	Inner rings	-3.16×10^{-4}	0.981	4.44×10^{-4}	0.980
	Outer rings	-1.25×10^{-2}	0.554	1.56×10^{-3}	0.911
	Superior	1.39×10^{-2}	0.303	-1.97×10^{-2}	0.309
	Inferior	-1.61×10^{-2}	0.422	5.72×10^{-3}	0.725
	Nasal	-1.44×10^{-2}	0.400	-4.81×10^{-3}	0.795
	Temporal	6.99×10^{-3}	0.851	5.76×10^{-2}	0.231
Birefringence (°/µm)	All rings	-1.08×10^{-8}	0.990	1.47×10^{-6}	0.039
	Inner rings	2.23×10^{-7}	0.585	1.37×10^{-6}	0.160
	Outer rings	-2.80×10^{-7}	0.864	1.72×10^{-6}	0.008
	Superior	5.13×10^{-7}	0.320	1.11×10^{-7}	0.880
	Inferior	-1.92×10^{-7}	0.610	3.27×10^{-6}	0.008
	Nasal	8.06×10^{-7}	0.432	-9.29×10^{-8}	0.940
	Temporal	-1.24×10^{-6}	0.700	8.17×10^{-6}	0.050
Birefringence Uncertainty (°/µm)	All rings	2.34×10^{-8}	0.761	4.49×10^{-7}	0.007
	Inner rings	-9.03×10^{-9}	0.904	4.37×10^{-7}	0.055
	Outer rings	7.35×10^{-8}	0.392	5.36×10^{-7}	0.004
	Superior	1.60×10^{-8}	0.813	2.85×10^{-7}	0.068
	Inferior	-1.20×10^{-8}	0.909	7.84×10^{-7}	0.002
	Nasal	2.44×10^{-7}	0.182	1.71×10^{-7}	0.545
	Temporal	1.99×10^{-7}	0.230	1.89×10^{-6}	0.001
Clustered Reflectance Index (RI)	All rings	-1.71×10^{-3}	0.000	-1.74×10^{-3}	0.010
	Inner rings	-1.45×10^{-3}	0.009	-1.19×10^{-3}	0.040
	Outer rings	-1.95×10^{-3}	0.001	-1.99×10^{-3}	0.019
	Superior	-1.54×10^{-3}	0.000	-1.33×10^{-3}	0.013
	Inferior	-1.69×10^{-3}	0.000	-8.65×10^{-4}	0.138
	Nasal	-1.96×10^{-3}	0.000	-2.04×10^{-3}	0.022
	Temporal	-1.64×10^{-3}	0.001	-2.00×10^{-3}	0.005
Continuous Reflectance Index (RI)	All rings	-1.37×10^{-3}	0.000	-2.80×10^{-3}	0.000
	Inner rings	-1.29×10^{-3}	0.001	-2.72×10^{-3}	0.001
	Outer rings	-1.43×10^{-3}	0.000	-2.86×10^{-3}	0.000
	Superior	-1.99×10^{-3}	0.002	-3.40×10^{-3}	0.001
	Inferior	-1.43×10^{-3}	0.029	-3.62×10^{-3}	0.000
	Nasal	-1.01×10^{-3}	0.000	-1.71×10^{-3}	0.004
	Temporal	-1.03×10^{-3}	0.066	-2.37×10^{-3}	0.003

Table 4. RNFL parameters in segmented regions versus number of days for primate 2 analyzed with a linear mixed model. P-values with values <0.05 have been marked in red to easily identify the regions of statistical significance.

RNFL Parameter	Feature	Primate 2			
		Control		Treated	
		Slope	p (slope)	Slope	p (slope)
Clustered Thickness (µm)	All rings	1.54 x 10^{-2}	0.611	1.01 x 10-1	0.611
	Inner rings	5.75 x 10^{-2}	0.127	1.73 x 10^{-1}	0.127
	Outer rings	-3.74 x 10^{-2}	0.379	5.76 x 10^{-2}	0.379
	Superior	1.59 x 10^{-1}	0.062	5.50 x 10^{-2}	0.062
	Inferior	-2.64 x 10^{-2}	0.701	1.67 x 10^{-1}	0.701
	Nasal	-1.68 x 10^{-2}	0.606	8.62 x 10^{-2}	0.606
	Temporal	-3.10 x 10^{-2}	0.490	1.11 x 10^{-2}	0.490
Continuous Thickness (µm)	All rings	-1.87 x 10^{-2}	0.377	4.50 x 10^{-2}	0.160
	Inner rings	-1.30 x 10^{-2}	0.601	5.26 x 10^{-2}	0.298
	Outer rings	-2.39 x 10^{-2}	0.278	4.02 x 10^{-2}	0.170
	Superior	2.13 x 10^{-2}	0.450	1.82 x 10^{-2}	0.657
	Inferior	-7.32 x 10^{-2}	0.135	8.36 x 10^{-2}	0.061
	Nasal	-3.44 x 10^{-2}	0.155	2.25 x 10^{-2}	0.584
	Temporal	6.70 x 10^{-3}	0.795	3.25 x 10^{-2}	0.419
Phase Retardation (°)	All rings	-2.30 x 10^{-3}	0.711	2.84 x 10^{-3}	0.774
	Inner rings	-2.93 x 10^{-3}	0.703	1.21 x 10^{-2}	0.437
	Outer rings	-4.13 x 10^{-3}	0.623	-5.82 x 10^{-4}	0.949
	Superior	1.50 x 10^{-2}	0.194	1.26 x 10^{-3}	0.934
	Inferior	-2.58 x 10^{-2}	0.147	2.57 x 10^{-2}	0.081
	Nasal	4.91 x 10^{-3}	0.470	-3.84 x 10^{-3}	0.773
	Temporal	-3.25 x 10^{-3}	0.757	-7.88 x 10^{-3}	0.652
Birefringence (°/µm)	All rings	8.03 x 10^{-9}	0.971	-3.62 x 10^{-7}	0.301
	Inner rings	-2.03 x 10^{-7}	0.486	-4.62 x 10^{-7}	0.440
	Outer rings	1.99 x 10^{-7}	0.305	-2.38 x 10^{-7}	0.316
	Superior	-1.88 x 10^{-7}	0.372	-1.87 x 10^{-7}	0.714
	Inferior	-2.75 x 10^{-7}	0.342	6.04 x 10^{-8}	0.829
	Nasal	3.36 x 10^{-7}	0.316	-4.71 x 10^{-7}	0.305
	Temporal	1.28 x 10^{-7}	0.800	-6.75 x 10^{-7}	0.264
Birefringence Uncertainty (°/µm)	All rings	-2.12 x 10^{-8}	0.657	-6.13 x 10^{-8}	0.314
	Inner rings	-2.94 x 10^{-8}	0.643	-1.33 x 10^{-7}	0.202
	Outer rings	-1.03 x 10^{-8}	0.784	-4.92 x 10^{-9}	0.914
	Superior	-5.72 x 10^{-8}	0.206	5.95 x 10^{-8}	0.583
	Inferior	-2.25 x 10^{-8}	0.480	-9.07 x 10^{-8}	0.047
	Nasal	-1.59 x 10^{-8}	0.849	-8.17 x 10^{-8}	0.190
	Temporal	9.67 x 10^{-9}	0.917	-1.49 x 10^{-7}	0.183
Clustered Reflectance Index (RI)	All rings	-4.95 x 10^{-4}	0.255	-1.63 x 10^{-3}	0.000
	Inner rings	1.49 x 10^{-4}	0.784	-1.36 x 10^{-3}	0.000
	Outer rings	-9.90 x 10^{-4}	0.032	-1.85 x 10^{-3}	0.000
	Superior	-7.25 x 10^{-4}	0.131	-1.45 x 10^{-3}	0.000
	Inferior	-2.22 x 10^{-4}	0.651	-1.65 x 10^{-3}	0.000
	Nasal	-3.66 x 10^{-4}	0.459	-1.56 x 10^{-3}	0.000
	Temporal	-6.84 x 10^{-4}	0.080	-1.79 x 10^{-3}	0.000
Continuous Reflectance Index (RI)	All rings	-1.02 x 10^{-3}	0.018	-1.90 x 10^{-3}	0.001
	Inner rings	-1.11 x 10^{-3}	0.018	-1.70 x 10^{-3}	0.002
	Outer rings	-9.47 x 10^{-4}	0.030	-2.07 x 10^{-3}	0.001
	Superior	-1.56 x 10^{-3}	0.007	-2.25 x 10^{-3}	0.001
	Inferior	-3.00 x 10^{-4}	0.714	-1.80 x 10^{-3}	0.003
	Nasal	-1.10 x 10^{-3}	0.083	-2.27 x 10^{-3}	0.002
	Temporal	-1.12 x 10^{-3}	0.049	-1.28 x 10^{-3}	0.013

Table 5. RNFL parameters in segmented regions versus number of days for primate 3 analyzed with a linear mixed model. P-values with values <0.05 have been marked in red to identify the regions of statistical significance.

RNFL Parameter	Feature	Primate 3			
		Control		Treated	
		Slope	p (slope)	Slope	p (slope)
Clustered Thickness (µm)	All rings	-3.74×10^{-2}	0.151	-3.57×10^{-3}	0.151
	Inner rings	-6.99×10^{-2}	0.061	-2.14×10^{-3}	0.061
	Outer rings	-9.70×10^{-3}	0.679	-8.07×10^{-3}	0.679
	Superior	-5.72×10^{-2}	0.179	1.02×10^{-2}	0.179
	Inferior	-2.64×10^{-2}	0.598	-6.36×10^{-2}	0.598
	Nasal	-4.10×10^{-2}	0.071	8.72×10^{-3}	0.071
	Temporal	1.37×10^{-2}	0.648	1.71×10^{-2}	0.648
Continuous Thickness (µm)	All rings	1.84×10^{-2}	0.345	2.57×10^{-2}	0.329
	Inner rings	1.18×10^{-2}	0.632	3.24×10^{-2}	0.340
	Outer rings	2.25×10^{-2}	0.189	2.05×10^{-2}	0.342
	Superior	2.01×10^{-3}	0.934	-3.23×10^{-3}	0.897
	Inferior	3.77×10^{-2}	0.241	3.79×10^{-2}	0.391
	Nasal	5.30×10^{-2}	0.020	3.56×10^{-2}	0.377
	Temporal	-1.56×10^{-2}	0.415	4.04×10^{-2}	0.115
Phase Retardation (°)	All rings	-2.00×10^{-3}	0.741	-1.79×10^{-2}	0.134
	Inner rings	-3.41×10^{-3}	0.581	-2.87×10^{-2}	0.149
	Outer rings	-7.21×10^{-4}	0.915	-8.76×10^{-3}	0.211
	Superior	-7.78×10^{-3}	0.364	-2.37×10^{-2}	0.160
	Inferior	-1.19×10^{-2}	0.269	-8.96×10^{-3}	0.497
	Nasal	3.19×10^{-3}	0.740	-1.73×10^{-2}	0.220
	Temporal	2.07×10^{-2}	0.007	-2.24×10^{-2}	0.199
Birefringence (°/µm)	All rings	2.36×10^{-7}	0.376	-6.75×10^{-7}	0.225
	Inner rings	3.75×10^{-7}	0.178	-9.57×10^{-7}	0.221
	Outer rings	1.06×10^{-7}	0.718	-4.22×10^{-7}	0.269
	Superior	-2.45×10^{-8}	0.926	-7.32×10^{-7}	0.203
	Inferior	-1.01×10^{-7}	0.738	-1.26×10^{-7}	0.753
	Nasal	5.69×10^{-7}	0.445	-8.69×10^{-7}	0.315
	Temporal	7.78×10^{-7}	0.015	-9.62×10^{-7}	0.237
Birefringence Uncertainty (°/µm)	All rings	4.90×10^{-8}	0.310	-9.67×10^{-8}	0.351
	Inner rings	8.50×10^{-8}	0.087	-1.28×10^{-7}	0.352
	Outer rings	1.65×10^{-8}	0.756	-7.14×10^{-8}	0.355
	Superior	3.88×10^{-8}	0.298	-3.45×10^{-8}	0.651
	Inferior	-3.03×10^{-9}	0.931	-6.92×10^{-8}	0.465
	Nasal	1.49×10^{-7}	0.371	-1.31×10^{-7}	0.496
	Temporal	2.65×10^{-8}	0.615	-1.50×10^{-7}	0.188
Clustered Reflectance Index (RI)	All rings	-1.01×10^{-3}	0.092	-1.65×10^{-3}	0.004
	Inner rings	-8.48×10^{-4}	0.157	-1.58×10^{-3}	0.007
	Outer rings	-1.13×10^{-3}	0.138	-1.69×10^{-3}	0.007
	Superior	-1.07×10^{-3}	0.102	-1.79×10^{-3}	0.001
	Inferior	-1.01×10^{-3}	0.119	-1.37×10^{-3}	0.033
	Nasal	-9.98×10^{-4}	0.096	-1.71×10^{-3}	0.006
	Temporal	-9.16×10^{-4}	0.131	-1.48×10^{-3}	0.007
Continuous Reflectance Index (RI)	All rings	-1.20×10^{-3}	0.017	-1.33×10^{-3}	0.006
	Inner rings	-1.23×10^{-3}	0.014	-1.60×10^{-3}	0.009
	Outer rings	-1.18×10^{-3}	0.021	-1.14×10^{-3}	0.005
	Superior	-1.02×10^{-3}	0.095	-1.47×10^{-3}	0.006
	Inferior	-9.63×10^{-4}	0.146	-1.17×10^{-3}	0.055
	Nasal	-1.08×10^{-3}	0.059	-1.86×10^{-3}	0.001
	Temporal	-1.74×10^{-3}	0.007	-8.76×10^{-4}	0.073

Table 6. RNFL parameter differences (control less treated) in segmented regions versus IOP damage integral for individual primates analyzed with a linear mixed model. P-values with values <0.05 have been marked in red to identify the regions of statistical significance.

RNFL Parameter	Feature	Primate 1		Primate 2		Primate 3	
		Slope	p (slope)	Slope	p (slope)	Slope	p (slope)
Clustered Thickness (µm)	Entire ring	7.41×10^{-3}	0.007	-5.18×10^{-3}	0.063	-3.62×10^{-3}	0.196
	Inner ring	6.15×10^{-3}	0.034	-6.94×10^{-3}	0.074	-7.49×10^{-3}	0.095
	Outer ring	7.72×10^{-3}	0.012	-5.78×10^{-3}	0.020	-4.98×10^{-5}	0.983
	Superior	9.69×10^{-3}	0.122	6.56×10^{-3}	0.244	-7.03×10^{-3}	0.182
	Inferior	2.17×10^{-2}	0.004	-1.21×10^{-2}	0.013	2.77×10^{-3}	0.658
	Nasal	-8.60×10^{-3}	0.069	-6.21×10^{-3}	0.032	-5.04×10^{-3}	0.055
	Temporal	2.09×10^{-2}	0.001	-8.27×10^{-3}	0.149	-6.90×10^{-4}	0.842
Continuous Thickness (µm)	Entire ring	8.16×10^{-3}	0.029	-3.73×10^{-3}	0.097	-1.27×10^{-3}	0.648
	Inner ring	9.08×10^{-3}	0.018	-3.85×10^{-3}	0.251	-2.67×10^{-3}	0.428
	Outer ring	7.41×10^{-3}	0.049	-3.76×10^{-3}	0.076	-2.71×10^{-4}	0.915
	Superior	3.43×10^{-3}	0.371	4.89×10^{-4}	0.866	5.49×10^{-5}	0.987
	Inferior	2.12×10^{-2}	0.008	-9.51×10^{-3}	0.016	-1.21×10^{-3}	0.815
	Nasal	9.42×10^{-3}	0.000	-3.43×10^{-3}	0.205	1.05×10^{-3}	0.758
	Temporal	-3.86×10^{-3}	0.386	-1.40×10^{-3}	0.568	-5.38×10^{-3}	0.025
Phase Retardation (°)	Entire ring	-1.75×10^{-4}	0.837	-2.80×10^{-4}	0.669	1.67×10^{-3}	0.115
	Inner ring	4.80×10^{-5}	0.963	-8.42×10^{-4}	0.369	2.66×10^{-3}	0.129
	Outer ring	-5.93×10^{-4}	0.592	-2.24×10^{-4}	0.718	8.51×10^{-4}	0.204
	Superior	1.85×10^{-3}	0.088	9.14×10^{-4}	0.446	1.49×10^{-3}	0.319
	Inferior	-1.02×10^{-3}	0.444	-3.16×10^{-3}	0.011	-9.96×10^{-5}	0.945
	Nasal	-5.51×10^{-4}	0.683	5.52×10^{-4}	0.504	2.03×10^{-3}	0.104
	Temporal	-2.19×10^{-3}	0.446	3.46×10^{-4}	0.661	4.48×10^{-3}	0.015
Birefringence (°/µm)	Entire ring	-8.20×10^{-8}	0.099	2.30×10^{-8}	0.170	9.67×10^{-8}	0.033
	Inner ring	-6.22×10^{-8}	0.134	1.70×10^{-8}	0.483	1.40×10^{-7}	0.038
	Outer ring	-1.12×10^{-7}	0.208	2.65×10^{-8}	0.114	5.73×10^{-8}	0.111
	Superior	9.10×10^{-9}	0.790	5.29×10^{-12}	1.000	7.14×10^{-8}	0.120
	Inferior	-1.95×10^{-7}	0.001	-1.95×10^{-8}	0.376	8.73×10^{-9}	0.834
	Nasal	4.30×10^{-8}	0.626	4.96×10^{-8}	0.054	1.48×10^{-7}	0.049
	Temporal	-4.83×10^{-7}	0.117	4.92×10^{-8}	0.131	1.84×10^{-7}	0.025
Clustered Reflectance Index (RI)	Entire ring	8.67×10^{-7}	0.977	6.89×10^{-5}	0.027	4.95×10^{-5}	0.462
	Inner ring	-7.67×10^{-6}	0.774	9.07×10^{-5}	0.030	5.27×10^{-5}	0.417
	Outer ring	-6.85×10^{-6}	0.888	5.33×10^{-5}	0.035	4.69×10^{-5}	0.565
	Superior	-1.22×10^{-5}	0.663	4.35×10^{-5}	0.156	5.91×10^{-5}	0.403
	Inferior	-4.72×10^{-5}	0.181	8.74×10^{-5}	0.011	2.32×10^{-5}	0.734
	Nasal	1.88×10^{-6}	0.962	7.31×10^{-5}	0.050	5.25×10^{-5}	0.459
	Temporal	2.00×10^{-5}	0.563	6.65×10^{-5}	0.031	3.80×10^{-5}	0.587
Continuous Reflectance Index (RI)	Entire ring	7.41×10^{-5}	0.034	5.30×10^{-5}	0.124	-5.20×10^{-7}	0.993
	Inner ring	7.65×10^{-5}	0.044	3.60×10^{-5}	0.258	1.77×10^{-5}	0.803
	Outer ring	7.23×10^{-5}	0.033	6.72×10^{-5}	0.081	-1.35×10^{-5}	0.805
	Superior	6.80×10^{-5}	0.267	4.24×10^{-5}	0.289	4.12×10^{-5}	0.540
	Inferior	1.31×10^{-4}	0.002	8.76×10^{-5}	0.118	-7.55×10^{-6}	0.934
	Nasal	3.74×10^{-5}	0.099	7.14×10^{-5}	0.162	7.08×10^{-5}	0.256
	Temporal	5.24×10^{-5}	0.356	9.32×10^{-6}	0.810	-9.84×10^{-5}	0.215

Chapter 5: The diagnostic power of RNFL thickness, phase retardation, birefringence, and reflectance in a human clinical trial

In this chapter, we further investigate in a human glaucoma clinical study the diagnostic potential of RNFL reflectance that was identified in the non-human primate study described in Chapter 4. We compare the performance of RNFL Thickness, phase retardation, birefringence, and a modified reflectance index for distinguishing among healthy subjects, glaucoma patients, and patients categorized as "glaucoma suspect".

5.1 METHODS

This chapter presents the computational analysis of data from the clinical study described in Chapter 2. We use the measurements from the PS-OCT and RTVue OCT instruments in this Chapter.

5.1.1 RNFL thickness, phase retardation, and birefringence of different RNFL locations

For data collected at the Eye Institute of Austin, a LABVIEW software program (National Instruments, Austin, Texas) was implemented for the PS-OCT system to automatically detect RNFL and RPE region boundaries in each B-scan[12,35]. After RNFL boundary detection, an expert on PS-OCT retinal image evaluation visually inspected the boundaries superimposed on each B-scan to manually correct any misidentified boundaries. For data collected at the Duke Eye Center, an active contour based algorithm was used for RNFL and RPE region boundary detection [60]. The difference in the RNFL and RPE region boundary detection methods is another reason for not combining the data from EIA and Duke for this analysis. The calculations of phase retardation and birefringence were described in previous papers by our group and were the same for both EIA and Duke datasets[12,38]. RNFL thickness, phase retardation, and

birefringence were then imported into MATLAB (The Mathworks, Natick, MA) for calculation of average values in different RNFL locations. For the PS-OCT system, the RNFL locations analyzed in this study are: all-rings, inner 5 rings, outer 5 rings, temporal quadrant (T), superior quadrant (S), nasal quadrant (N), and inferior quadrant (I), (Figure 34). For the RTVue OCT system, the only difference in the analysis is that we calculated the 7 inner rings average, as opposed to the 5 inner rings average, and the 6 outer rings average, as opposed to the 5 outer rings average, since an RTVue ONH scan has 13 ring scans around the ONH, rather than 10 rings as in a PS-OCT scan. The two GDx VCC parameters included in this study are TSNIT averages, which were reported as the parameter with the highest repeatability and least variability[37], and nerve fiber indicator (NFI), which is reported to be the best parameter of GDx for glaucoma diagnosis[61,62,63].

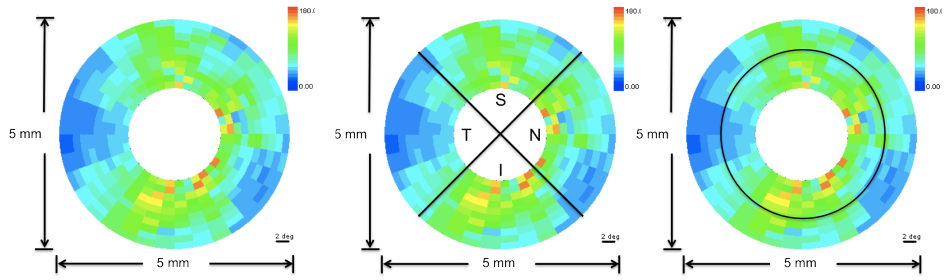

Figure 34. Definitions of RNFL locations as shown on a clustered RNFLT map of a human right eye (OD). An average across all-rings can be taken (left). Or, averages can be computed over the temporal (T), superior (S), inferior (I), and nasal (N) quadrants as shown in the middle panel. The right panel shows the demarcation of the 5 inner rings and 5 outer rings regions in the RNFLT map.

5.1.2 RNFL Reflectance

To quantify RNFL reflectance, we introduce a normalized RNFL reflectance index that is different from the reflectance index (RI) that we used in our previous study with non-human primates [38]. The normalized RNFL reflectance index (*NRRI*) is defined as the ratio of the summation of OCT intensities of the RNFL (I_{RNFL}) to the average OCT intensities of a thin layer centered on the retinal pigment epithelium (*RPE*). The advantage of the new NRRI measure is that it sums the backscattered intensity across the RNFL; thus, it is a hybrid measurement that combines the RNFLT and RI measures as they were defined in the primate study. Moreover, NRRI performs better than RI at distinguishing between glaucomatous and healthy eyes. Since the intensity is normalized relative to the RPE, the NRRI is unitless.

Specifically, for PS-OCT, we define *NRRI* for one cluster in one B-scan image corresponding to one image collection session as:

$$NRRI = \frac{I_{RNFL_c}}{\overline{I}_{RPE}} \quad \textbf{(16)}$$

where

$$I_{RNFL_c} = \sum_c \left(\sum_a I_{RNFL_a} \right)_c \quad \textbf{(17)}$$

which is the summation of the OCT signal intensity in the RNFL for all A-scans of the c^{th} cluster with 100 A-scans per cluster.

The average OCT intensities of a thin layer about the retinal pigment epithelium is calculated as

$$\overline{I}_{RPE} = \frac{\sum_{b=1}^{N_b} \left(\sum_a I_{RPE_a} / N_{RPE} \right)_b}{N_b} \quad \textbf{(18)}$$

where N_b is the number of B-scans in each image collection, and N_{RPE} is the number of pixels (7 pixels, about 50 microns) in the RPE layer.

For RTVue OCT, we define *NRRI* for one A-scan in one B-scan image corresponding to one image collection session as:

$$NRRI = \frac{\sum_a I_{RNFL_a}}{\bar{I}_{RPE}} \quad (19)$$

where

$$\bar{I}_{RPE} = \frac{\sum_{b=1}^{N_b} \left(\sum_a I_{RPE_a} / N_{RPE} \right)_b}{N_b} \quad (20)$$

which is the average OCT signal intensity in the RPE layer averaged over all B-scans in one image collection, where N_b is the number of B-scans in each image collection, and N_{RPE} is the number of pixels (7 pixels, about 70 microns) in the RPE layer. For one imaging session, we calculate $NRRI$ for A-scans in one retinal scan and then construct an *NRRI* map for that scan. The average NRRI of the seven RNFL locations is computed.

5.1.3 Statistical analysis

The area under the Receiver Operating Characteristic (ROC) curve (AUC) was used to compare the performance of the RNFLT and NRRI features for distinguishing between normal subjects and glaucoma patients as well as between normal subjects and patients meeting the definition of glaucoma suspect. Differences between the areas under the ROC curves were compared using a non-parametric method based on bootstrap sampling (n=2000 resamples). Since the identification of diagnostic parameters that can

achieve high sensitivity or high specificity is of particular interest, we also compared the partial ROC areas for the high sensitivity or high specificity region of the curves (sensitivity ≥ 90% or specificity ≥ 90%). We used the pROC package[64] the R statistical programming language (v2.15.10; http://www.R-project.org/, R Development Core Team, 2012, R Foundation for Statistical Computing, Vienna, Austria) and R studio (v0.94, RStudio, Inc.) for the ROC analysis. The PASS 11 software (NCSS, Kaysville, Utah 84037) was used for statistical power and sample size calculations.

5.2 RESULTS

We calculated the average NRRI, RNFL thickness, phase retardation, and birefringence measured in seven RNFL locations: all-rings; inner 5 rings for PS-OCT or inner 7 rings for RTVue OCT; outer 5 rings for PS-OCT or outer 6 rings for RTVue OCT; temporal quadrant (T); superior quadrant (S); nasal quadrant (N); and inferior quadrant (I). Pairwise comparisons among NRRI, RNFL thickness, phase retardation, and birefringence average in different RNFL locations for distinguishing between healthy and glaucomatous eyes as well as between healthy and glaucoma suspect eyes were made in terms of the area and partial area (sensitivity ≥ 90% or specificity ≥ 90%) under the ROC curves.

5.2.1 NRRI, RNFL thickness, phase retardation, and birefringence measured by PS-OCT for distinguishing between healthy and glaucomatous eyes

We first compared the performance of the all rings average of NRRI ($NRRI_{all}$), the all rings average of RNFL thickness ($RNFLT_{all}$), the all rings average of phase retardation (PR_{all}), and the all rings average of birefringence (BR_{all}) from both EIA and DEC datasets since these global averages were reported to be the most reproducible in previous studies[26] (AUC shown in Table 7 and ROC curves shown in Figure 35). For the EIA

dataset, we found that the AUC of $NRRI_{all}$ was significantly larger than the areas under the ROC curves for PR_{all} (p=0.003) and birefringence (p=0.00002). We also found that the AUC of $RNFLT_{all}$ was significantly larger than that of PR_{all} (p=0.007) and BR_{all} (p=0.0002). Thus, the average of all rings of $NRRI_{all}$ and $RNFLT_{all}$ both performed significantly better than PR_{all} and BR_{all} at distinguishing between healthy and glaucomatous eyes. However, we didn't find a significant difference between the AUC of $RNFLT_{all}$ and $NRRI_{all}$ (p=0.331). This is probably due to the small sample size. With the current sample size we can only achieve statistical power of 4%. In order to achieve 90% power to detect a difference of 0.043 between the AUCs of $RNFLT_{all}$ and $NRRI_{all}$, we would need 325 samples each of healthy and glaucomatous eyes. The AUCs of PR_{all} and BR_{all} are also statistically indistinguishable (p=0.067). The results for the data collected at the Duke Eye Center are similar, as shown in Table 9. Since the identification of diagnostic parameters that can achieve high sensitivity is of particular interest, we also compared the partial ROC areas for the high sensitivity region of the curves (sensitivity ≥ 90%). We compared the partial ROC curves of $NRRI_{inner}$ and $RNFLT_S$ in the 0.90 to 1 sensitivity region. For the DEC data, we found that the partial AUC of $NRRI_{all}$ is significantly larger than that of $RNFLT_{all}$ in the 0.90 to 1 sensitivity region (p= 0.0406). Thus, $NRRI_{all}$ performed significantly better than $RNFLT_{all}$ at distinguishing between healthy and glaucomatous eyes when high sensitivity was required.

In the preceding analysis, each of the RNFL properties was quantified by averaging across all of the rings since such global averages were reported to be the most reproducible in previous studies[26]. However, it is possible that averaging only over certain RNFL locations, e.g., across the outer rings only, could provide more diagnostically useful values for some RFNL properties. Thus, in this analysis, we selected the RNFL location that provided the largest AUC value for each of the RNFL

properties for comparison (shown in red in Table 7). We found that for the EIA dataset, the all rings average of NRRI ($NRRI_{all}$), the inner rings average of RNFL thickness ($RNFLT_{inner}$), the superior quadrant average of phase retardation (PR_S), and the all rings average of birefringence (BR_{all}) had the largest AUCs. The pairwise comparisons of these RNFL properties measured in these 'best' RNFL locations of both the EIA and DEC datasets are similar to the findings of using average all rings location (p values are shown in Table 10) with one exception; for the EIA dataset, we found the AUC of PR_S was significantly larger than that of BR_{all} (p=0.004). For the partial ROC curves comparisons, we found that for DEC data, the partial AUC of $NRRI_{all}$ is significantly larger than the one of $RNFLT_{inner}$ in the 0.90 to 1 sensitivity region (p= 0.0416).

Table 7. AUC and its standard errors (SE) of NRRI, RNFL thickness, phase retardation and birefringence averaged over different RNFL locations measured by PS-OCT for distinguishing between healthy and glaucomatous eyes of EIA dataset.

RNFL location	**Healthy vs. Glaucoma**							
	NRRI		Thickness		Phase retardation		Birefringence	
	AUC	SE	AUC	SE	AUC	SE	AUC	SE
All rings	0.983	0.021	0.932	0.056	0.547	0.145	0.419	0.131
Inner rings	0.923	0.078	0.940	0.050	0.598	0.138	0.427	0.131
Outer rings	0.966	0.032	0.897	0.071	0.521	0.142	0.410	0.132
Superior	0.923	0.060	0.872	0.076	0.650	0.131	0.474	0.131
Inferior	0.872	0.086	0.889	0.068	0.470	0.156	0.368	0.142
Nasal	0.872	0.076	0.735	0.112	0.521	0.133	0.350	0.125
Temporal	0.838	0.096	0.838	0.089	0.504	0.138	0.427	0.130

Table 8. AUC and its standard errors (SE) of NRRI, RNFL thickness, phase retardation and birefringence averaged over different RNFL locations measured by PS-OCT for distinguishing between healthy and glaucomatous eyes of DEC dataset.

RNFL location	**Healthy vs. Glaucoma**							
	NRRI		Thickness		Phase retardation		Birefringence	
	AUC	SE	AUC	SE	AUC	SE	AUC	SE
All rings	0.957	0.032	0.880	0.065	0.460	0.109	0.403	0.107
Inner rings	0.947	0.037	0.790	0.083	0.490	0.106	0.415	0.102
Outer rings	0.963	0.026	0.910	0.058	0.463	0.112	0.393	0.104
Superior	0.860	0.063	0.783	0.081	0.533	0.110	0.388	0.101
Inferior	0.920	0.044	0.837	0.071	0.443	0.116	0.387	0.109
Nasal	0.813	0.075	0.635	0.097	0.420	0.104	0.407	0.104
Temporal	0.823	0.073	0.657	0.095	0.493	0.104	0.450	0.101

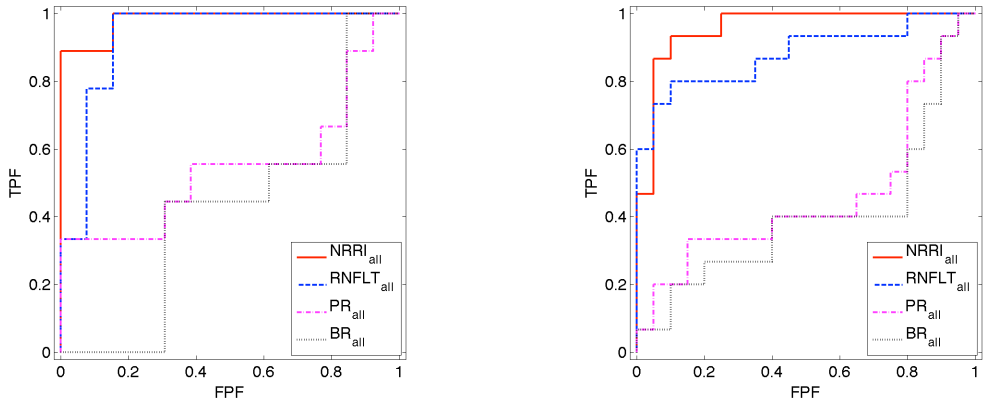

Figure 35. ROCs of average of all rings of NRRI, RNFL thickness, phase retardation, and birefringence for distinguishing between healthy and glaucomatous eyes of Eye Institute of Austin (EIA) data (shown in left) and Duke Eye Center (DEC) data (shown in right).

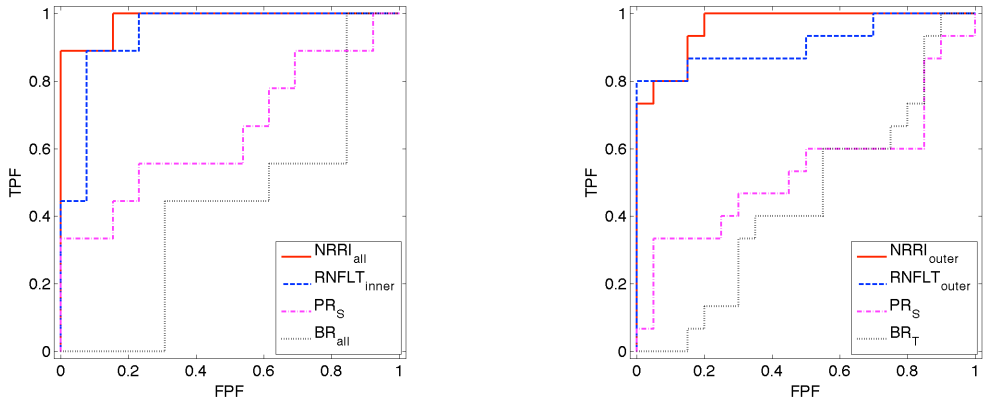

Figure 36. ROCs of average of all rings of NRRI, inner rings of RNFL thickness, superior of phase retardation, and all rings of birefringence for distinguishing between healthy and glaucomatous eyes of Eye Institute of Austin (EIA) data (shown in left). ROCs of average of outer rings of NRRI, outer rings of RNFL thickness, superior of phase retardation and temporal of birefringence for distinguishing between healthy and glaucomatous eyes of Duke Eye Center (DEC) data (shown in right).

Table 9. P values of comparisons of the AUCs of the all rings average of NRRI, RNFL thickness, phase retardation birefringence for distinguishing between healthy and glaucomatous eyes of both EIA and DEC datasets.

Comparisons of AUC	p value	
	EIA	DEC
NRRI vs RNFLT	0.33112	0.20040
NRRI vs .PR	0.00260	0.00006
NRRI vs .BR	0.00002	0.00001
RNFLT vs .PR	0.00715	0.00319
RNFLT vs .BR	0.00020	0.00111
PR vs. BR	0.06741	0.05403

Table 10. P values of comparisons of the AUCs of the best RNFL locations of NRRI, RNFL thickness, phase retardation birefringence for distinguishing between healthy and glaucomatous eyes of both EIA and DEC datasets.

Comparisons of AUC	p value	
	EIA	DEC
NRRI vs .RNFLT	0.37884	0.33799
NRRI vs .PR	0.00871	0.00044
NRRI vs .BR	0.00002	0.00001
RNFLT vs .PR	0.03668	0.00484
RNFLT vs .BR	0.00018	0.00010
PR vs. BR	0.00412	0.28223

5.2.2 NRRI, RNFL thickness, phase retardation, and birefringence measured by PS-OCT for distinguishing between healthy and glaucoma suspect eyes

We first compared the performance of $NRRI_{all}$, $RNFLT_{all}$, PR_{all}, and BR_{all} for both the EIA and DEC datasets (Figure 37). From the comparisons using the EIA dataset, we found that the AUC of $NRRI_{all}$ was significantly larger than those of $RNFLT_{all,}$(p=0.03), PR_{all} (p=0.0016), and BR_{all} (p=0.00004). Thus, $NRRI_{all}$ performed significantly better than $RNFLT_{all}$, PR_{all}, and BR_{all} at distinguishing between healthy and glaucoma suspect eyes. We also found the the AUC of $RNFLT_{all}$ and PR_{all} was significantly larger than that of BR_{all} (p=0.016 and p=0.038 respectively). $RNFLT_{all}$ and PR_{all} performed significantly better than BR_{all} at distinguishing between healthy and glaucoma suspect eyes. However, we didn't find a significant difference between the AUC of $RNFLT_{all}$ and PR_{all} (p=0.089). This is probably due to the small sample size. We would need 48 samples for each of healthy and glaucoma suspect eyes to achieve 90% power to detect a difference of 0.212 between the AUCs of $RNFLT_{all}$ and PR_{all}. For the DEC dataset, some of the results of comparisons are different. We didn't find a significant difference between the AUC of $NRRI_{all}$ and $RNFLT_{all}$ (p=0.150). We would need 137 samples for each of healthy and glaucoma suspect eyes to achieve 90% power

to detect a difference of 0.07 between the AUCs of $NRRI_{all}$ and $RNFLT_{all}$. We also didn't find a significant difference between the AUC of PR_{all} and BR_{all} (p=0.116). But we find the AUC of $RNFLT_{all}$ was significantly larger than that of PR_{all} (p=0.0075).

In the subsequent analysis, we selected the RNFL location that provided the largest AUC value for each of the RNFL properties for comparison (shown in red in Table 11, ROC curves shown in Figure 37). We found that the inner rings average of NRRI, the superior average of RNFL thickness, the inferior average of phase retardation, and the temporal average of birefringence had the largest AUCs for the EIA data. We found that the AUC of $NRRI_{inner}$ was significantly larger than those of PR_I ($p = 0.003$) and BR_T ($p = 0.0006$). The other comparisons of the full AUCs didn't show any statistically significant difference (Table 14). However, the partial AUC of $NRRI_{inner}$ is significantly larger than that of $RNFLT_S$ in the 0.90 to 1 specificity region ($p = 0.0007$). Thus, $NRRI_{inner}$ performed significantly better at distinguishing between healthy and glaucoma suspect eyes when high specificity was required. For the DEC data, the all rings average of NRRI, the inferior average of RNFL thickness, the temporal average of phase retardation, and the temporal average of birefringence had the largest AUCs. The pair-wise comparisons showed similar results of those using all rings average for DEC data.

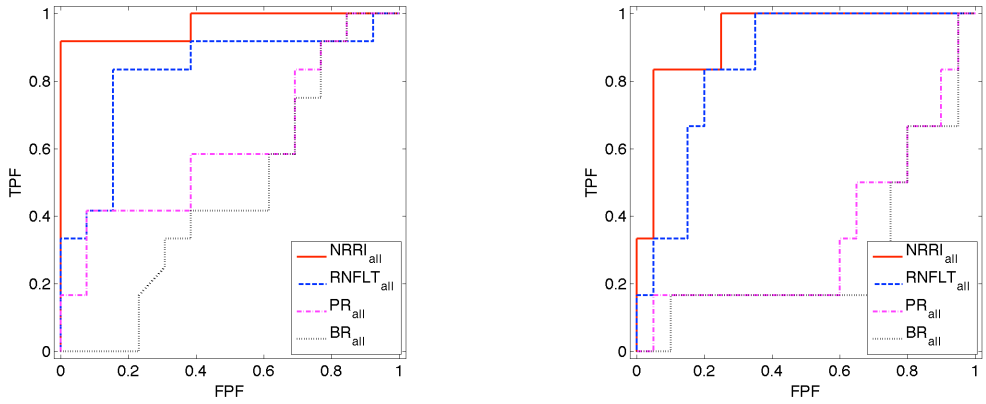

Figure 37. ROCs of the all rings average of NRRI, RNFL thickness, phase retardation and birefringence on distinguishing between healthy and glaucoma suspect eyes of Eye Institute of Austin (EIA) data (shown in left) and Duke Eye Center (DEC) data (shown in right).

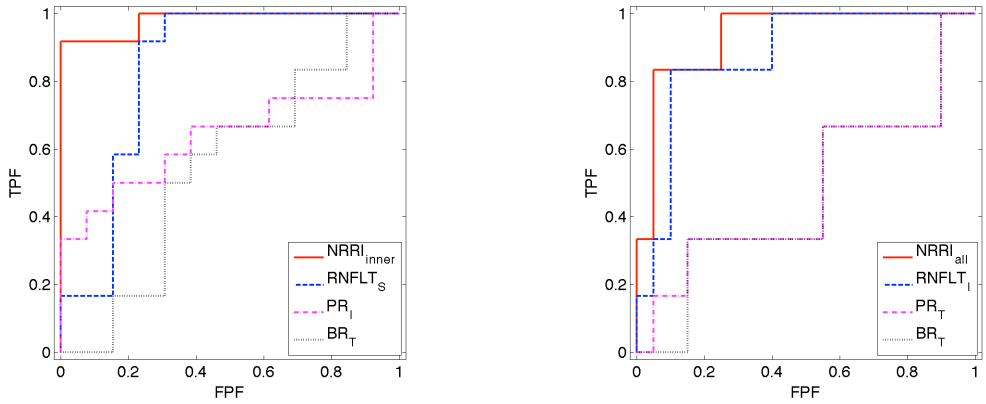

Figure 38. ROCs of average of inner rings of NRRI, superior of RNFL thickness, inferior of phase retardation and temporal of birefringence for distinguishing between healthy and glaucoma suspect eyes of Eye Institute of Austin (EIA) data (shown in left). ROCs of average of all rings of NRRI, inferior of RNFL thickness, temporal of phase retardation and temporal of birefringence for distinguishing between healthy and glaucoma suspect eyes of Duke Eye Center (DEC) data (shown in right).

Table 11. AUC and its standard errors (SE) for distinguishing between healthy and glaucoma suspect eyes of NRRI, RNFL thickness, phase retardation, and birefringence averaged over different RNFL locations as measured by PS-OCT of EIA dataset.

RNFL location	**Healthy vs. Glaucoma suspect**							
	NRRI		Thickness		Phase retardation		Birefringence	
	AUC	SE	AUC	SE	AUC	SE	AUC	SE
All rings	0.968	0.034	0.821	0.094	0.609	0.120	0.465	0.122
Inner rings	0.981	0.022	0.808	0.089	0.635	0.117	0.500	0.123
Outer rings	0.955	0.041	0.788	0.101	0.564	0.121	0.452	0.121
Superior	0.897	0.064	0.833	0.092	0.609	0.121	0.404	0.119
Inferior	0.936	0.047	0.801	0.089	0.641	0.122	0.462	0.122
Nasal	0.782	0.101	0.756	0.107	0.558	0.122	0.429	0.122
Temporal	0.769	0.104	0.660	0.117	0.538	0.123	0.545	0.122

Table 12. AUC and its standard errors (SE) for distinguishing between healthy and glaucoma suspect eyes of NRRI, RNFL thickness, phase retardation, and birefringence averaged over different RNFL locations as measured by PS-OCT of DEC dataset.

RNFL location	**Healthy vs. Glaucoma suspect**							
	NRRI		Thickness		Phase retardation		Birefringence	
	AUC	SE	AUC	SE	AUC	SE	AUC	SE
All rings	0.933	0.052	0.850	0.077	0.342	0.147	0.283	0.142
Inner rings	0.833	0.117	0.800	0.110	0.367	0.134	0.333	0.126
Outer rings	0.908	0.063	0.742	0.130	0.283	0.157	0.250	0.151
Superior	0.808	0.085	0.750	0.134	0.392	0.159	0.321	0.126
Inferior	0.867	0.088	0.875	0.077	0.408	0.181	0.325	0.163
Nasal	0.583	0.145	0.483	0.133	0.333	0.159	0.375	0.174
Temporal	0.667	0.124	0.450	0.142	0.483	0.148	0.467	0.152

Table 13. P values of comparisons of the AUCs of the all rings average of NRRI, RNFL thickness, phase retardation birefringence for distinguishing between healthy and glaucoma suspect eyes of both EIA and DEC datasets.

Comparisons of AUC	p value	
	EIA	DEC
NRRI vs. RNFLT	0.02995	0.14984
NRRI vs. PR	0.00164	0.00065
NRRI vs .BR	0.00004	0.00017
RNFLT vs .PR	0.08870	0.00750
RNFLT vs .BR	0.01607	0.00265
PR vs. BR	0.03785	0.11590

Table 14. P values of comparisons of the AUCs of the best RNFL locations of NRRI, RNFL thickness, phase retardation birefringence for distinguishing between healthy and glaucoma suspect eyes of both EIA and DEC datasets.

Comparisons of AUC	p value	
	EIA	DEC
NRRI vs. RNFLT	0.10098	0.22672
NRRI vs. PR	0.00298	0.00053
NRRI vs .BR	0.00055	0.00466
RNFLT vs .PR	0.18955	0.00606
RNFLT vs .BR	0.06461	0.02849
PR vs. BR	0.46296	0.22998

5.2.3 NRRI and RNFL thickness measured by RTVue OCT for distinguishing healthy, glaucomatous, and glaucoma suspect eyes

We also validated our findings on data acquired using an RTVue OCT system. We didn't find a statistically significant difference between the AUC of $NRRI_{all}$ and that of $RNFLT_{all}$ for distinguishing between healthy and glaucomatous eyes (p=0.877, Figure 39). For distinguishing healthy and glaucomatous eyes, the all rings average of NRRI ($NRRI_{inner}$) and all rings average of RNFL thickness ($RNFLT_{all}$) turned out to have the largest AUC among all the RNFL locations of NRRI and RNFLT (shown in red in Table

15). Thus, $NRRI_{all}$ and $RNFLT_{all}$ performed similarly for distinguishing between healthy and glaucomatous eyes.

For distinguishing healthy and glaucoma suspect eyes, we first compared the performance of $NRRI_{all}$ and $RNFLT_{all}$. We found that the AUC of $NRRI_{all}$ was significantly larger than that of $RNFLT_{all,}$ (p=0.014). Thus, $NRRI_{all}$ performs significantly better than $RNFLT_{all}$ at distinguishing between healthy and glaucoma suspect eyes. We compared the RNFL location inferior average, which gave the largest AUC (shown in red in Table 16) for both NRRI ($NRRI_I$) and RNFL thickness ($RNFLT_I$). The AUC of $NRRI_I$ was significantly larger than that of $RNFLT_{I,}$ (p=0.008). Thus, $NRRI_I$ also performs significantly better than $RNFLT_I$ at distinguishing between healthy and glaucoma suspect eyes.

Table 15. AUC and its standard errors (SE) for distinguishing between healthy and glaucomatous eyes of NRRI and RNFL thickness averaged over different RNFL locations as measured by RTVue OCT.

	Healthy vs. Glaucoma			
	NRRI		Thickness	
RNFL location	AUC	SE	AUC	SE
All rings	0.957	0.037	0.949	0.043
Inner rings	0.957	0.037	0.940	0.046
Outer rings	0.949	0.043	0.932	0.054
Superior	0.949	0.043	0.897	0.065
Inferior	0.949	0.043	0.906	0.074
Nasal	0.923	0.059	0.915	0.061
Temporal	0.872	0.075	0.726	0.124

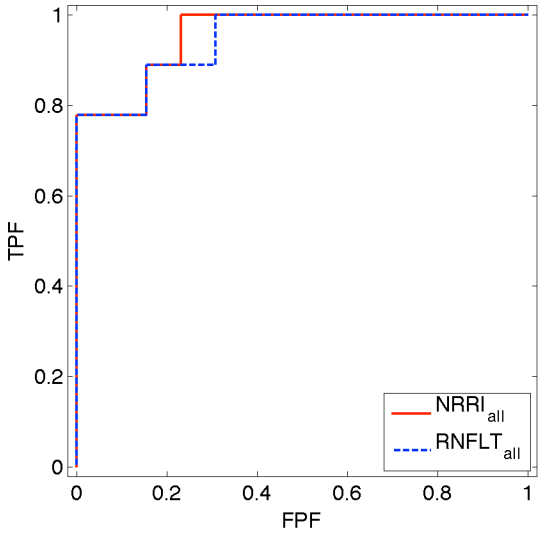

Figure 39. ROC curves for distinguishing between healthy and glaucomatous eyes based on the all rings averages of NRRI and RNFL thickness as measured by RTVue OCT.

Table 16. AUC and its standard errors (SE) for distinguishing between healthy and glaucoma suspect eyes based on NRRI and RNFL thickness averaged over different RNFL locations as measured by RTVue OCT.

	Healthy vs. Glaucoma Suspect			
	NRRI		Thickness	
RNFL location	AUC	SE	AUC	SE
All rings	0.885	0.066	0.679	0.118
Inner rings	0.833	0.081	0.673	0.116
Outer rings	0.878	0.073	0.744	0.106
Superior	0.846	0.085	0.724	0.106
Inferior	0.929	0.052	0.744	0.110
Nasal	0.763	0.104	0.667	0.118
Temporal	0.622	0.125	0.487	0.124

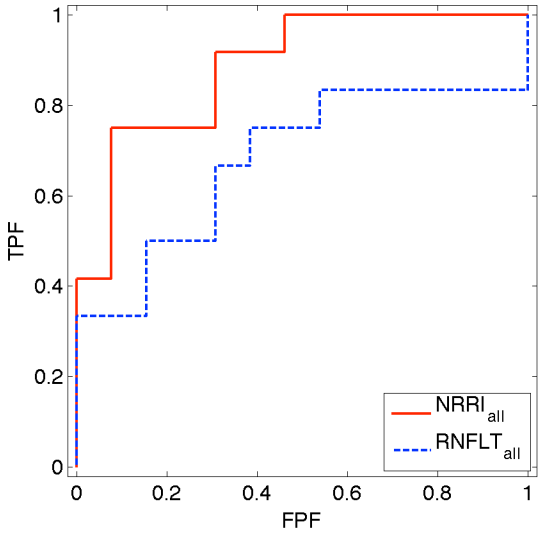

Figure 40. ROC curves for distinguishing between healthy and glaucoma suspect eyes based on the all rings averages of NRRI and RNFL thickness as measured by RTVue OCT.

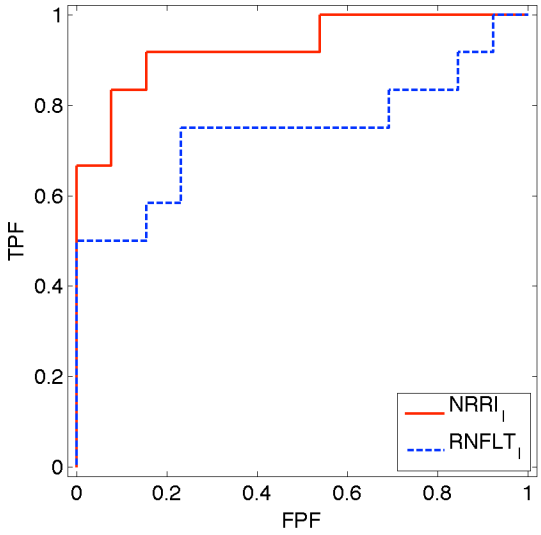

Figure 41. ROC curves for distinguishing between healthy and glaucoma suspect eyes based on the inferior averages of NRRI and RNFL thickness as measured by RTVue OCT.

5.2.4 NRRI measured by PS-OCT, TSNIT average and NFI measured by GDx VCC for distinguishing healthy, glaucomatous and glaucoma suspect eyes

We compared the NRRI measured in the RNFL location that gave the largest AUC to the TSNIT average and NFI provided by GDx VCC in both the EIA and DEC datasets (Table 17). The comparisons of ROC curves for distinguishing healthy and glaucomatous eyes were shown in Figure 42. For both the EIA and DEC datasets, the performance between NRRI and TSNIT average as well as between NRRI and NFI were statistically indistinguishable (For NRRI vs. TSNIT, p=0.052 for EIA data, p=0.165 for DEC data; For NRRI vs. NFI, p=0.074 for EIA data, p=0.384 for DEC data). However, we found that for the EIA dataset, the partial AUC of NRRI was significantly larger than that of TSNIT and NFI in 0.90 to 1 sensitivity region (p=0.010 for NRRI vs. TSNIT; p=0.027 for NRRI vs. NFI). For the DEC dataset, the partial AUC of NRRI was significantly larger than that of TSNIT in 0.90 to 1 sensitivity region (p=0.028).

The comparisons of ROC curves for distinguishing healthy and glaucoma suspect eyes are shown in Figure 43. For the EIA dataset, we found that the AUC of NRRI is significantly larger than those of the TSNIT average (p=0.0120) and NFI (p=0.0187). For the DEC dataset, we found that the AUC of NRRI is significantly larger than that of the TSNIT average (p=0.0286), but not significantly larger than that of NFI (p=0.137). Therefore, NRRI performed significantly better than TSNIT average provided by GDx for distinguishing healthy and glaucoma suspect eyes in both datasets. NRRI performed significantly better than NFI provided by GDx for distinguishing healthy and glaucoma suspect eyes in the EIA dataset.

Table 17. AUC and its standard errors (SE) for distinguishing between healthy and glaucomatous eyes as well as healthy and glaucoma suspect eyes based on NRRI measured by PS-OCT, TSNIT average and NFI measured by GDx VCC.

	Healthy vs. Glaucoma				**Healthy vs. Glaucoma suspect**			
	TSNIT		NFI		TSNIT		NFI	
Study institute	AUC	SE	AUC	SE	AUC	SE	AUC	SE
Eye Institute of Austin	0.752	0.123	0.786	0.108	0.721	0.107	0.686	0.114
Duke Eye Center	0.850	0.081	0.915	0.048	0.617	0.159	0.792	0.106

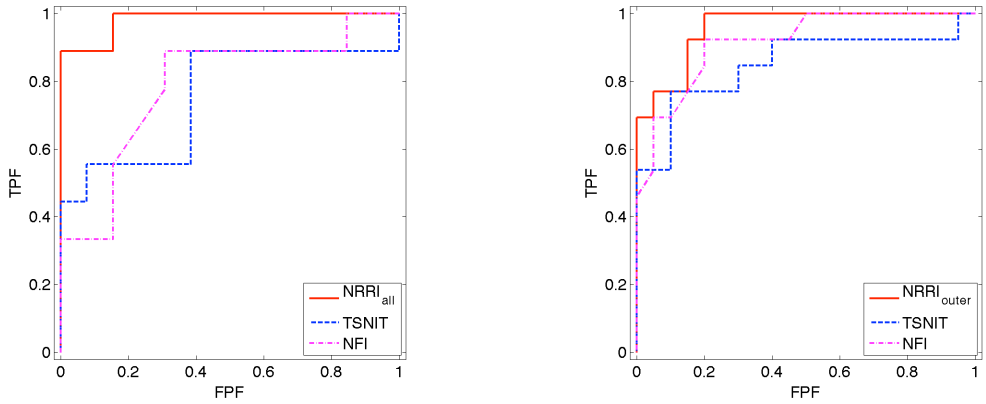

Figure 42. ROC curves of NRRI measured by PS-OCT, TSNIT average and NFI measured by GDx VCC for distinguishing between healthy and glaucomatous eyes of Eye Institute of Austin (EIA) data (shown in left) and Duke Eye Center (DEC) data (shown in right).

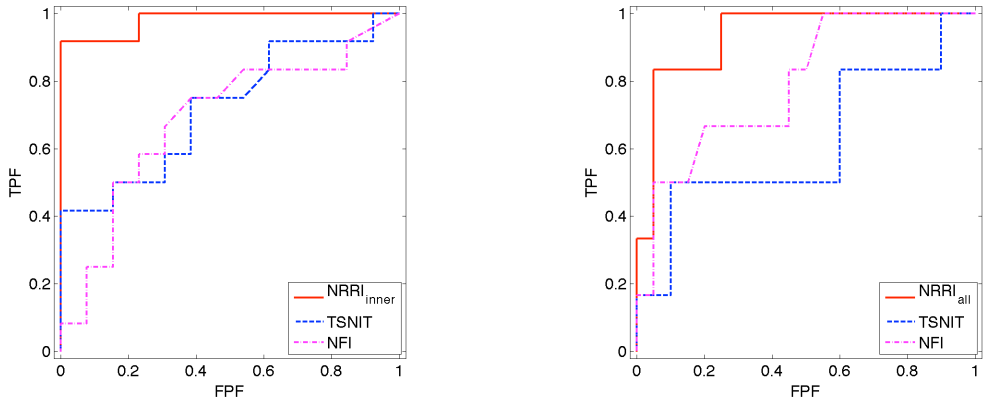

Figure 43. ROC curves of NRRI measured by PS-OCT, TSNIT average and NFI measured by GDx VCC for distinguishing between healthy and glaucoma suspect eyes of Eye Institute of Austin (EIA) data (shown in left) and Duke Eye Center (DEC) data (shown in right).

5.3 DISCUSSION

In this human clinical study, we assessed the diagnostic potential of RNFL thickness, phase retardation, birefringence, and normalized RNFL reflectance index (NRRI) measured in seven different RNFL locations (all rings, inner rings, outer rings, and TSNI quadrants) by PS-OCT for distinguishing between healthy and glaucomatous eyes as well as between healthy and glaucoma suspect eyes in a study conducted at the Eye Institute of Austin. We also assessed the diagnostic potential of RNFL thickness and NRRI measured in seven different RNFL locations (all rings, inner rings, outer rings, and TSNI quadrants) by RTVue OCT for distinguishing between healthy and glaucomatous eyes as well as between healthy and glaucoma suspect eyes on the same study population at the Eye Institute of Austin. Additionally, we also assessed the diagnostic power of RNFL thickness, phase retardation, birefringence, and normalized RNFL reflectance index (NRRI) measured by a modified version of the PS-OCT instrument in a study at the Duke Eye Center. From the measurements by both original and modified version of the PS-OCT, we found that for both diagnostic tasks, NRRI performs significantly better than

either phase retardation or birefringence. However, the performances of NRRI and RNFL thickness were statistically indistinguishable in this study except the all rings average of NRRI and RNFL on distinguishing between healthy and glaucoma suspect eyes using EIA dataset. It is likely that the lack of statistical significance is due to the limited sample size. We also did some partial ROC curves comparisons. We found that the inner ring average of NRRI performed significantly better for distinguishing between healthy and glaucoma suspect eyes than superior average of RNFLT in the 0.90 to 1 specificity region for EIA dataset. From the RTVue OCT measurements, we found that for distinguishing between healthy and glaucomatous eyes, the performances of NRRI and RNFL thickness were statistically indistinguishable. However, the NRRI performs significantly better than RNFL thickness at distinguishing between healthy and glaucoma suspect eyes. In addition, we compared the NRRI measured in the RNFL location that gave the largest AUC to the TSNIT average and NFI provided by GDx VCC in both EIA and DEC datasets. For both datasets, NRRI performed similarly to TSNIT average and NFI for distinguishing between healthy and glaucomatous eyes. NRRI performed significantly better than TSNIT average provided by GDx for distinguishing healthy and glaucoma suspect eyes on both datasets. NRRI performed significantly better than NFI provided by GDx for distinguishing healthy and glaucoma suspect eyes on EIA dataset. Since GDx actually measures phase retardation of RNFL, the comparisons above are actually NRRI vs. phase retardation measured by GDx. In interpreting these findings, it should be noted that NRRI as defined in this paper is different from the RI parameter introduced in our previous study on non-human primates[38]. NRRI contains information from *both* RNFL thickness and reflectance. Thus, NRRI can be considered as a combination feature of RNFL thickness and reflectance.

Table 18. Pearson's correlation between NRRI measured by both PS-OCT and RTVue OCT and age in the healthy, glaucoma, and glaucoma suspect groups of the dataset from Eye Institute of Austin (EIA) and Duke Eye Center (DEC).

	NRRI by PS-OCT vs. Age of EIA		NRRI by PS-OCT vs. Age of DEC		NRRI by RTVue OCT vs. Age of EIA	
Patient Group	rho	p value	rho	p value	rho	p value
Healthy	0.371	0.213	0.087	0.778	-0.093	0.762
Glaucoma	0.431	0.247	-0.163	0.675	0.284	0.459
Glaucoma suspect	-0.129	0.690	-0.148	0.647	-0.017	0.959

The average age of the patients of healthy, glaucoma, and glaucoma suspect groups enrolled in this study are significantly different as shown Figure 4 and Figure 5. The average age of healthy subjects is significantly less than that of both the glaucoma and glaucoma suspect groups as tested by two-sample t-test for two independent samples with equal variance in dataset from Eye Institute of Austin (EIA) and Duke Eye Center (DEC) (EIA: $p=0.0008$ for healthy vs. glaucoma; $p=0.0006$ for healthy vs. glaucoma suspects DEC: $p=0.0003$ for healthy vs. glaucoma; $p=0.019$ for healthy vs. glaucoma suspects). Therefore, RNFL thickness measurements might be biased by the differences in ages in different groups since RNFLT decreases as age increases [65,66,67,68]. However, we evaluated the Pearson's correlation between NRRI measured by both PS-OCT and RTVue OCT and age in the healthy, glaucoma, and glaucoma suspect groups, respectively, and didn't find statistically significant correlations ($p>0.5$ for all groups as shown in Table 18). Thus, it seems unlikely that the results of the NRRI analysis are affected by the age differences between the groups. In conclusion, we showed that NRRI has the potential to outperform RNFL thickness, phase retardation and birefringence for distinguishing between healthy and glaucoma suspect eyes. Therefore, NRRI is a promising new marker for detecting glaucoma at the earliest stage. Measurement of NRRI does not require any new instrumentation. It's implementation only requires new

software. This pilot clinical study suggests the need for a larger clinical study to validate the diagnostic power of NRRI in pre-perimetric glaucoma.

Chapter 6: Conclusion and Future work

In this dissertation, we first investigated LPCC based and MI based registration algorithms and determined the benefits of image registration on estimation of longitudinal RNFL thickness (RNFLT) changes. We found that the precision and recall calculated between manually segmented image pairs are significantly better following registration by either MI or LPCC algorithms than before any registration is performed. The trends in the all-rings average and TSNI-quadrants average of RNFLT over time in healthy primate eyes are not affected by registration. RNFLT of clock hours 1, 2, and 10 in primate eyes showed significant changes over a 30-week time period without registration, but stay constant over time with registration. Thus, either the MI or the LPCC algorithm can improve registration of RNFLT maps recorded on different dates in a longitudinal study. In our study, LPCC provided better registration of RNFLT maps recorded on different dates than did the MI algorithm. Improved registration of RNFLT maps measured using OCT can improve clinical analysis of glaucoma progression.

Secondly, we investigated candidate markers for early glaucoma diagnosis. We measured time variation of retinal nerve fiber layer (RNFL) thickness, phase retardation, birefringence, and reflectance using polarization sensitive optical coherence tomography (PS-OCT) in three non-human primates with induced glaucoma in one eye. We also characterize the variation of RNFL thickness, phase retardation, birefringence, and reflectance with elevated intraocular pressure (IOP). We found that elevated IOP was associated with loss of RNFL reflectance, while thickness, phase retardation, and birefringence showed no significant changes at the mean IOP and integral IOP levels tested. Thus, decreased RNFL reflectance was the earliest correlate with glaucomatous

damage in this study. Candidate cellular mechanisms are considered for decreased RNFL reflectance including mitochondrial dysfunction and retinal ganglion cell apoptosis.

Finally, we validate our findings of primates model on human clinical study data acquired by two instruments, PS-OCT and RTVue OCT. For the data acquired by PS-OCT, we found that RNFL thickness and our new normalized RNFL reflectance index (NRRI) perform significantly better than birefringence for distinguishing between healthy and glaucomatous eyes as well as healthy and glaucoma suspect eyes. NRRI also performs significantly better than phase retardation on distinguishing between healthy and glaucomatous eyes, as well as between healthy and glaucoma suspect eyes. However, there was no statistically significant difference between the performances of NRRI and RNFL thickness, likely due to the limited sample size. In analyzing the data acquired by RTVue OCT, we didn't find a significant difference between the performances of NRRI and RNFL thickness for distinguishing between healthy and glaucomatous eyes. However, NRRI performs significantly better than RNFL thickness on distinguishing between healthy and glaucoma suspect eyes. NRRI showed potential to be an earlier indicator of glaucoma than RNFL thickness on two different OCT instruments. In addition, we compared the NRRI measured in the RNFL location that gave the largest AUC to the TSNIT average and NFI provided by GDx VCC. NRRI performed similarly to TSNIT average and NFI for distinguishing between healthy and glaucomatous eyes. NRRI performed significantly better than TSNIT average and NFI provided by GDx for distinguishing healthy and glaucoma suspect eyes. Of course, while these results are highly encouraging, our findings will need to be validated in future studies with a larger sample size.

In conclusion, we demonstrated that implementing registration algorithms in recorded OCT images has the potential to improve analysis and interpretation of changes

in the retinal nerve fiber layer thickness over time as assessed in a longitudinal study. We defined an RNFL reflectance index (RI), which might be an earlier indicator of glaucoma than RNFL thickness, phase retardation and birefringence on non-human primates. We validated this finding in a clinical study on human eyes. We developed a normalized RNFL reflectance index (NRRI) that combines information from both RNFL thickness and reflectance. We showed that NRRI has the potential to outperform RNFL thickness, phase retardation and birefringence for distinguishing between healthy and glaucoma suspect eyes. Therefore, NRRI is a promising new marker for detecting glaucoma at the earliest stage.

References

1. Quigley HA (1996) Number of people with glaucoma worldwide. Br J Ophthalmol 80: 389-393.
2. Quigley HA, Broman AT (2006) The number of people with glaucoma worldwide in 2010 and 2020. Br J Ophthalmol 90: 262-267.
3. Tielsch JM, Sommer A, Katz J, Royall RM, Quigley HA, et al. (1991) Racial variations in the prevalence of primary open-angle glaucoma. The Baltimore Eye Survey. JAMA 266: 369-374.
4. Quigley HA, Addicks EM, Green WR (1982) Optic nerve damage in human glaucoma. III. Quantitative correlation of nerve fiber loss and visual field defect in glaucoma, ischemic neuropathy, papilledema, and toxic neuropathy. Arch Ophthalmol 100: 135-146.
5. Gupta D (2005) Glaucoma diagnosis and management. philadelphia: LIPPINCOTT WILLIAMS & WILKINS.
6. Panel AAoOG (2010) Preferred Practice Pattern® Guidelines. Primary Open-Angle Glaucoma Suspect. . San Francisco, CA: American Academy of Ophthalmology.
7. Drance SM, Sweeney VP, Morgan RW, Feldman F (1973) Studies of factors involved in the production of low tension glaucoma. Arch Ophthalmol 89: 457-465.
8. Schrems WA, Mardin CY, Horn FK, Juenemann AG, Laemmer R (2009) Comparison of Scanning Laser Polarimetry and Optical Coherence Tomography in Quantitative Retinal Nerve Fiber Assessment. J Glaucoma.
9. Zangwill LM, Bowd C, Berry CC, Williams J, Blumenthal EZ, et al. (2001) Discriminating between normal and glaucomatous eyes using the Heidelberg Retina Tomograph, GDx Nerve Fiber Analyzer, and Optical Coherence Tomograph. Arch Ophthalmol 119: 985-993.
10. Poinoosawmy D, Tan JC, Bunce C, Hitchings RA (2001) The ability of the GDx nerve fibre analyser neural network to diagnose glaucoma. Graefes Arch Clin Exp Ophthalmol 239: 122-127.
11. Chang RT, Knight OJ, Feuer WJ, Budenz DL (2009) Sensitivity and specificity of time-domain versus spectral-domain optical coherence tomography in diagnosing early to moderate glaucoma. Ophthalmology 116: 2294-2299.
12. Elmaanaoui B, Wang B, Dwelle JC, McElroy AB, Liu SS, et al. (2011) Birefringence measurement of the retinal nerve fiber layer by swept source polarization sensitive optical coherence tomography. Opt Express 19: 10252-10268.
13. Gaasterland D, Kupfer C (1974) Experimental Glaucoma in the Rhesus Monkey. Investigative Ophthalmology and Visual Science 13: 455-457.
14. Pederson J, Gaasterland D (1984) Laser-Induced Primate Glaucoma. 1.Progression of Glaucoma. Archives of Ophthalmology 102: 1689-1692.
15. Quigley HA, Hohman RM (1983) Laser energy levels for trabecular meshwork damage in the primate eye. Invest Ophth Visual 24: 1305-1307.

16. Quigley HA, Hohman RM (1983) Laser energy levels for trabecular meshwork damage in the primate eye. Investigative Ophthalmology and Visual Science 24: 1305-1307.
17. Schuman JS, Pedut-Kloizman T, Pakter H, Wang N, Guedes V, et al. (2007) Optical coherence tomography and histologic measurements of nerve fiber layer thickness in normal and glaucomatous monkey eyes. Investigative Ophthalmology and Visual Science 48: 3645-3654.
18. Elmaanaoui B, Wang B, Dwelle JC, McElroy AB, Liu SS, et al. (2011) Birefringence measurement of the retinal nerve fiber layer by swept source polarization sensitive optical coherence tomography. Optics express 19: 10252-10268.
19. Kemp NJ, Park J, Zaatari HN, Rylander HG, Milner TE (2005) High-sensitivity determination of birefringence in turbid media with enhanced polarization-sensitive optical coherence tomography. Journal of the Optical Society of America A, Optics and Image Science 22: 552-560.
20. Kemp NJ, Park J, Zaatari HN, Rylander HG, Milner TE (2005) High-sensitivity determination of birefringence in turbid media with enhanced polarization-sensitive optical coherence tomography. Journal of the Optical Society of America A 22: 552-560.
21. Liu S, Datta A, Ho D, Dwelle JC, Milner TE, et al. (2012) Effect of registration on longitudinal analysis of Retinal Nerve Fiber Layer Thickness in non-human primates using Optical Coherence Tomography. under revision, Investigative Ophthalmology & Visual Science
22. Liu S, Datta A, Ho D, Milner TE, III HGR, et al. (2012) Comparison of registration algorithms on retinal blood vessel images from Optical Coherence Tomography. submitted to 34th Annual International Conference of the Engineering in Medicine and Biology Society. San Diego, California, USA.
23. Cvenkel B, Kontestabile AS (2011) Correlation between nerve fibre layer thickness measured with spectral domain OCT and visual field in patients with different stages of glaucoma. Graefes Arch Clin Exp Ophthalmol 249: 575-584.
24. Horn FK, Mardin CY, Laemmer R, Baleanu D, Juenemann AM, et al. (2009) Correlation between local glaucomatous visual field defects and loss of nerve fiber layer thickness measured with polarimetry and spectral domain OCT. Invest Ophthalmol Vis Sci 50: 1971-1977.
25. Yalvac IS, Altunsoy M, Cansever S, Satana B, Eksioglu U, et al. (2009) The correlation between visual field defects and focal nerve fiber layer thickness measured with optical coherence tomography in the evaluation of glaucoma. J Glaucoma 18: 53-61.
26. Garas A, Vargha P, Hollo G (2010) Reproducibility of retinal nerve fiber layer and macular thickness measurement with the RTVue-100 optical coherence tomograph. Ophthalmology 117: 738-746.
27. Gonzalez-Garcia AO, Vizzeri G, Bowd C, Medeiros FA, Zangwill LM, et al. (2009) Reproducibility of RTVue retinal nerve fiber layer thickness and optic disc

measurements and agreement with Stratus optical coherence tomography measurements. Am J Ophthalmol 147: 1067-1074, 1074 e1061.
28. Li JP, Wang XZ, Fu J, Li SN, Wang NL (2010) Reproducibility of RTVue retinal nerve fiber layer thickness and optic nerve head measurements in normal and glaucoma eyes. Chin Med J (Engl) 123: 1898-1903.
29. Vizzeri G, Bowd C, Medeiros FA, Weinreb RN, Zangwill LM (2008) Effect of improper scan alignment on retinal nerve fiber layer thickness measurements using Stratus optical coherence tomograph. J Glaucoma 17: 341-349.
30. Yoo C, Suh IH, Kim YY (2010) Comment on the article entitled "Effect of improper scan alignment on retinal nerve fiber layer thickness measurements using Stratus optical coherence tomograph" by Vizzeri G, Bowd C, Medeiros F, Weinreb R, Zangwill L, published in J Glaucoma. 2008;17:341-349. J Glaucoma 19: 226-227.
31. Pluim JP, Maintz JB, Viergever MA (2003) Mutual-information-based registration of medical images: a survey. IEEE Trans Med Imaging 22: 986-1004.
32. Ritter N, Owens R, Cooper J, Eikelboom RH, van Saarloos PP (1999) Registration of stereo and temporal images of the retina. IEEE Trans Med Imaging 18: 404-418.
33. Rosin PL, Marshall D, Morgan JE (2002) Multimodal Retinal Imaging: New Strategies For The Detection Of Glaucoma. Proceedings of IEEE International Conference on Image Processing. Rochester, NY, USA. pp. 137–140.
34. Wolberg G, Zokai S (2000) Robust image registration using log-polar transform In Proc IEEE Int Conf image processing. pp. 493--496.
35. Wang B, Paranjape A, Yin B, Liu S, Markey MK, et al. Optimized Retinal Nerve Fiber Layer Segmentation Based on Optical Reflectivity and Birefringence for Polarization-Sensitive Optical Coherence Tomography; 2011.
36. Schuman JS, Pedut-Kloizman T, Pakter H, Wang N, Guedes V, et al. (2007) Optical coherence tomography and histologic measurements of nerve fiber layer thickness in normal and glaucomatous monkey eyes. Invest Ophthalmol Vis Sci 48: 3645-3654.
37. Sehi M, Guaqueta DC, Greenfield DS (2006) An enhancement module to improve the atypical birefringence pattern using scanning laser polarimetry with variable corneal compensation. Br J Ophthalmol 90: 749-753.
38. Dwelle J, Liu S, Wang B, McElroy A, Ho D, et al. (2012) Thickness, phase retardation, birefringence, and reflectance of the retinal nerve fiber layer in normal and glaucomatous non-human primates. in press, Investigative Ophthalmology & Visual Science.
39. Huang X-R, Knighton RW (2005) Microtubules contribute to the birefringence of the retinal nerve fiber layer. Investigative Ophthalmology and Visual Science 46: 4588-4593.
40. Pocock GM, Aranibar RG, Kemp NJ, Specht CS, Markey MK, et al. (2009) The Relationship between Retinal Ganglion Cell Axon Constituents and Retinal Nerve Fiber Layer Birefringence in the Primate. Investigative Ophthalmology and Visual Science: 5238-5246.

41. Kong GYX, Van Bergen NJ, Trounce IA, Crowston JG (2009) Mitochondrial dysfunction and glaucoma. Journal of Glaucoma 18: 93-100.
42. Ju W-K, Liu Q, Kim K-Y, Crowston JG, Lindsey JD, et al. (2007) Elevated Hydrostatic Pressure Triggers Mitochondrial Fission and Decreases Cellular ATP in Differentiated RGC-5 Cells. Investigative Ophthalmology and Visual Science 48: 2145-2151.
43. Abu-Amero KK, Morales J, Bosley TM (2006) Mitochondrial abnormalities in patients with primary open-angle glaucoma. Investigative Ophthalmology and Visual Science 47: 2533-2541.
44. Huang X, Kong W, Zhou Y, Gregori G (2011) Distortion of axonal cytoskeleton: an early sign of glaucomatous damage. Investigative Ophthalmology and Visual Science 52: 2879-2888.
45. Zhang X, Hu J, Knighton RW, Huang X-R, Puliafito CA, et al. (2011) Dual-band spectral-domain optical coherence tomography for in vivo imaging the spectral contrasts of the retinal nerve fiber layer. Optics express 19: 19653-19659.
46. Wang B, Paranjape A, Yin B, Liu S, Markey MK, et al. (2011) Optimized retinal nerve fiber layer segmentation based on optical reflectivity and birefringence for polarization-sensitive optical coherence tomography. Proceedings of SPIE.
47. Park J, Kemp NJ, Zaatari HN, Rylander HG, Milner TE (2006) Differential geometry of normalized Stokes vector trajectories in anisotropic media. Journal of the Optical Society of America A, Optics and Image Science 23: 679-690.
48. Chauhan BC, Pan J, Archibald ML, LeVatte TL, Kelly ME, et al. (2002) Effect of intraocular pressure on optic disc topography, electroretinography, and axonal loss in a chronic pressure-induced rat model of optic nerve damage. Invest Ophthalmol Vis Sci 43: 2969-2976.
49. Thomsen S, Pearce JA (2011) Thermal Damage and Rate Processes in Biologic Tissues. In: Welch AJ, van Gemert MJC, editors. Optical-Thermal Response of Laser-Irradiated Tissue. 2nd. ed. New York: Springer. pp. 487-550.
50. Pinheiro J, Bates D (2009) Mixed-Effects Models in S and S-PLUS. New York, NY: Springer Verlag.
51. Zhang Y, Dong Y, Wu X, Lu Y, Xu Z, et al. (2010) The mitochondrial pathway of anesthetic isoflurane-induced apoptosis. J Biol Chem 285: 4025-4037.
52. Huang X, Zhou Y, Kong W, Knighton RW (2011) Reflectance Decrease Prior to Thickness Change of the Retinal Nerve Fiber Layer in Glaucomatous Retinas. Investigative Ophthalmology and Visual Science.
53. Mittag TW, Danias J, Pohorenec G, Yuan HM, Burakgazi E, et al. (2000) Retinal damage after 3 to 4 months of elevated intraocular pressure in a rat glaucoma model. Investigative Ophthalmology and Visual Science 41: 3451-3459.
54. Fraser J, Biousse V, Newman N (2010) The Neuro-ophthalmology of Mitochondrial Disease. Surv Ophthalmol 55: 299-334.
55. Ju W, Liu Q, Kim K, Crowston JG, Lindsey JD, et al. (2007) Elevated hydrostatic pressure triggers mitochondrial fission and decreases cellular ATP in differentiated RGC-5 cells. Investigative Ophthalmology and Visual Science.

56. Pasternack R, Zheng J, Boustany NN (2010) Detection of mitochondrial fission with orientation - dependent optical Fourier filters. Cytometry Part A.
57. Chalut K, Ostrander J, Giacomelli M, Wax A (2009) Light scattering measurements of subcellular structure provide noninvasive early detection of chemotherapy-induced apoptosis. Cancer research.
58. van der Meer F, Faber D, Aalders M, Poot AA, Vermes I, et al. (2010) Apoptosis-and necrosis-induced changes in light attenuation measured by optical coherence tomography. Lasers in Medical Science.
59. Farhat G, Mariampillai A, Yang V, Czarnota G, Kolios M (2011) Detecting apoptosis using dynamic light scattering with optical coherence tomography. Journal of Biomedical Optics.
60. Kass M, Witkin A, Terzopoulos D (1988) Snakes: Active contour models. International Journal of Computer Vision 1: 321-331.
61. Medeiros FA, Zangwill LM, Bowd C, Mohammadi K, Weinreb RN (2004) Comparison of scanning laser polarimetry using variable corneal compensation and retinal nerve fiber layer photography for detection of glaucoma. Arch Ophthalmol 122: 698-704.
62. Reus NJ, Lemij HG (2004) Diagnostic accuracy of the GDx VCC for glaucoma. Ophthalmology 111: 1860-1865.
63. Zheng W, Baohua C, Qun C, Zhi Q, Hong D (2008) Retinal nerve fiber layer images captured by GDx-VCC in early diagnosis of glaucoma. Ophthalmologica 222: 17-20.
64. Robin X, Turck N, Hainard A, Tiberti N, Lisacek F, et al. (2011) pROC: an open-source package for R and S+ to analyze and compare ROC curves. BMC Bioinformatics 12: 77.
65. Alamouti B, Funk J (2003) Retinal thickness decreases with age: an OCT study. Br J Ophthalmol 87: 899-901.
66. Bowd C, Zangwill LM, Blumenthal EZ, Vasile C, Boehm AG, et al. (2002) Imaging of the optic disc and retinal nerve fiber layer: the effects of age, optic disc area, refractive error, and gender. J Opt Soc Am A Opt Image Sci Vis 19: 197-207.
67. Varma R, Skaf M, Barron E (1996) Retinal nerve fiber layer thickness in normal human eyes. Ophthalmology 103: 2114-2119.
68. Leung CK, Yu M, Weinreb RN, Ye C, Liu S, et al. (2012) Retinal nerve fiber layer imaging with spectral-domain optical coherence tomography: a prospective analysis of age-related loss. Ophthalmology 119: 731-737.

Vita

Shuang Liu was born and grew up in Hubei, China. She obtained the B.S. and M.S. degrees in Electronics and Information Engineering in 2004 and 2006 from Huazhong University of Science and Technology, Wuhan, Hubei, China. From August 2006 to January 2008, Shuang studied in the Electrical Engineering Department at University of Houston, Houston, Texas. In 2011, Shuang received a Graduate Student Professional Development Award from The University of Texas at Austin. Shuang is a student member of Institute of Electrical and Electronics Engineers (IEEE), Biomedical Engineering Society (BMES), and The Association for Research in Vision and Ophthalmology (ARVO).

This dissertation was typed by Shuang Liu.